SINGLE-PIXEL OPTICAL ENCODING AND TRANSMISSION WITH RANDOM NUMBERS

CAO YONGGUI

PhD

The Hong Kong Polytechnic University

2024

The Hong Kong Polytechnic University
Department of Electrical and Electronic Engineering

Single-Pixel Optical Encoding and Transmission with Random Numbers

CAO Yonggui

A thesis submitted in partial fulfillment of the requirements
for the degree of Doctor of Philosophy

September 2023

CERTIFICATE OF ORIGINALITY

I hereby declare that this thesis is my own work and that, to the best of my knowledge and belief, it reproduces no material previously published or written, nor material that has been accepted for the award of any other degree or diploma, except where due acknowledgement has been made in the text.

_____(Signed)

_____CAO Yonggui_____(Name of Student)

Abstract

Free-space optical communication (FSO) is promising for data transmission, offering specific advantages over traditional systems in some applications, e.g., high bandwidth. Optical communication in free space is also less susceptible to interference and signal degradation, when atmospheric attenuation and multipath fading happen. However, FSO still faces significant challenges in practice. 1) The impact of scattering media, e.g., fog, smoke, or dust, can significantly degrade signal quality and limit data transmission range. 2) Security of optical data transmission needs to be addressed in many scenarios. Therefore, it is crucial to investigate high-fidelity optical data transmission in free space, which can overcome the challenges associated with scattering media and ensure the security of optical data transmission in free space.

In this thesis, new optical encoding approaches for high-fidelity optical diffraction and transmission through scattering media in free space are proposed using a series of 2D arrays of random numbers as information carriers. A series of 2D arrays of random numbers are directly generated to encode the ghosts, i.e., original signals or images. In addition, a new transmission scheme is designed to realize optical transmission through dynamic scattering media (e.g., smoke or turbid water). Real-time optical thickness is calculated to describe temporal change of the properties of optical wave in dynamic environment. Transmission noise and errors caused by dynamic smoke are temporally corrected. It is experimentally demonstrated that irregular analog signals can always be retrieved with high fidelity. To enhance transmission rate of the proposed system and evaluate robustness of the designed methods against dynamic and complex scattering media, the proposed optical data transmission scheme is optimized. New algorithms are proposed to generate 2D

binary arrays (i.e., information carriers). Therefore, the transmission rate would be increased significantly, since a digital micro-mirror device with a high switching rate can be applied.

In addition, security of the developed optical data transmission schemes is also analyzed, and an improved encrypted transmission scheme is proposed to realize high-fidelity and high-security data transmission. Different security keys, i.e., computer-generated keys and physically-generated keys, are applied in a scattering environment. An optimized data transmission system is also introduced to improve security of optical data transmission, when it is applied in a dynamic and complex scattering environment. Experimental results demonstrate feasibility and effectiveness of the proposed methods.

The studies in this thesis address two key scientific problems in optical data transmission in free space, i.e., high-fidelity optical data transmission through scattering media and high-security optical data transmission through scattering media. The studies pave a way for realizing high-fidelity and high-security free-space optical data transmission through scattering media using the concept of ghost diffraction and transmission with random numbers.

Publications

Journal Papers

(1) **Yonggui Cao**, Yin Xiao, and Wen Chen, "Securing 2D information carriers over dynamic and turbulent media in a free-space optical channel," Optics Letters, **48**(13), 3491–3494 (2023).

(2) **Yonggui Cao**, Yin Xiao, and Wen Chen, "Optical analog-signal transmission system in dynamic and complex scattering environment using binary encoding with a modified differential method," Optics Express, **31**(10), 16882–16896 (2023).

(3) **Yonggui Cao**, Yin Xiao, Zilan Pan, Lina Zhou, and Wen Chen, "Direct generation of 2D arrays of random numbers for high-fidelity optical ghost diffraction and information transmission through scattering media," Optics and Lasers in Engineering, **158**, 107141 (2022).

(4) **Yonggui Cao**, Yin Xiao, Zilan Pan, Lina Zhou, and Wen Chen, "High-fidelity temporally-corrected transmission through dynamic smoke via pixel-to-plane data encoding," Optics Express, **30**(20), 36464–36477 (2022).

(5) **Yonggui Cao**, Yin Xiao, Zilan Pan, Lina Zhou, and Wen Chen, "Physically-secured ghost diffraction and transmission," IEEE Photonics Technology Letters, **34**(22), 1238–1241 (2022).

(6) Zilan Pan, Yin Xiao, **Yonggui Cao**, Lina Zhou, and Wen Chen, "Optical analog-signal transmission and retrieval through turbid water," Applied Optics, **60**(34), 10704–10713 (2021). (Editor's Pick)

(7) Zilan Pan, Yin Xiao, **Yonggui Cao**, Lina Zhou, and Wen Chen, "Accurate optical information transmission through thick tissues using zero-frequency modulation and single-pixel detection," Optics and Lasers in Engineering, **158**, 107133 (2022).

(8) Zilan Pan, Yin Xiao, **Yonggui Cao**, Lina Zhou, and Wen Chen, "Optical data transmission through highly dynamic and turbid water using dynamic scaling factors and single-pixel detector," Optics Express, **30**(24), 43480–43490 (2022).

(9) Zilan Pan, Yin Xiao, Lina Zhou, **Yonggui Cao**, M. Yang, and Wen Chen, "Non-line-of-sight optical information transmission through turbid water," Optics Express, **29**(24), 39498–39510 (2021).

(10) Yin Xiao, Lina Zhou, Zilan Pan, **Yonggui Cao**, and Wen Chen, "Physically-enhanced ghost encoding," Optics letters, **47**(2), 433–436 (2022).

(11) Yin Xiao, Lina Zhou, Zilan Pan, **Yonggui Cao**, and Wen Chen, "Physically-secured high-fidelity free-space optical data transmission through scattering media using dynamic scaling factors," Optics Express, **30**(5), 8186–8198 (2022).

(12) Yin Xiao, Lina Zhou, Zilan Pan, **Yonggui Cao**, M. Yang, and Wen Chen, "Analog ghost hidden in 2D random binary patterns for free-space optical data transmission," Optics and Lasers in Engineering, **150**, 106880 (2022).

(13) Lina Zhou, Yin Xiao, Zilan Pan, **Yonggui Cao**, and Wen Chen, "Optical hiding based on single-input multiple-output and binary amplitude-only holograms via the modified Gerchberg-Saxton algorithm," Optics Express, **29**(16), 25675–25696 (2021).

(14) Lina Zhou, Yin Xiao, Zilan Pan, **Yonggui Cao**, and Wen Chen, "Visual Cryptography Using Binary Amplitude-Only Holograms," Frontiers in Photonics, **2**, 8 (2022).

Conference Papers

(1) **Yonggui Cao**, Yin Xiao, Zilan Pan, and Wen Chen, "2D Arrays of Random Numbers as Holograms for Optical Data Transmission through Scattering Media in Free Space," in *3D Image Acquisition and Display: Technology, Perception*

and Applications, Optica Publishing Group 2022, p. 3Tu5A. 9, 11-15 July 2022, Vancouver, British Columbia, Canada.

(2) **Yonggui Cao**, Yin Xiao, and Wen Chen, "Optical analog-signal transmission system in complex and dynamic scattering environment," Conference on Visible Light Communication and Optical Computing, 18–20 August 2023, Shenzhen, China. (Abstract)

(3) **Yonggui Cao**, Yin Xiao, and Wen Chen, "Secured optical transmission through dynamic and turbulent media with pixel-to-plane optical encoding," The International Conference on Optical and Photonic Engineering (icOPEN), 27 November to 1 December 2023, Singapore.

Acknowledgements

As time flies, I will finish my doctoral studies. I would like to take this opportunity to express my gratuities to all people who have supported me throughout my doctoral period. First and foremost, I am extremely grateful to my supervisor Dr. CHEN Wen, who has been providing me with a wealth of professional advice, patient guidance, and continued encouragement throughout my Ph.D study progress. The experience of studying and working with such a teacher is very enjoyable and rewarding. I am deeply impressed by his healthy lifestyle, rigorous academic attitude and hard working spirit, and Dr. CHEN Wen is a good example for my future study and life. I remember that when I first started my PhD study in Hong Kong, I encountered great difficulties in terms of not only my body and my PhD research areas. Thanks to Dr. CHEN 's encouragement and guidance, I slowly stepped into my own rhythm of life. In the weekly meeting with Dr. CHEN, I can learn a lot of meaningful knowledge and principles. Our weekly meetings have been fruitful and inspiring, and we have significant and meaningful discussions every week. Discussions with my teacher give me a clearer understanding of my advantages and greater confidence in myself. In addition, I would also like to give my great gratitude to my co-supervisor, Prof. YU Changyuan. He is a famous researcher in the field of optical fiber. It is always encouraging and positive to see things from his perspective when it comes to study and life. This experience has not only been helpful to my academic research, but to my personal and professional development as well.

Secondly, I would like to express my sincere gratitude to my excellent research team members. Dr. Xiao Yin has provided great help to my research work, and every discussion with him can bring me new research ideas. In addition to the discussion of research ideas, Dr. Xiao Yin also gave me a lot of suggestions on paper writing and

scientific research skills learning, which brings me great progress. Dr. Zhou Lina and Ms. Pan Zilan have also shared many innovative designs with me and provide me with many helps not only in the field of my research work but also in the field of my PhD life. It is also a great pleasure to meet other research members in our lab, Ms. Hao Yining, Ms. Peng Yang, Ms. Song Qian, Mr. Xu Zhihan, and we make a colorful and interesting life in Hong Kong together. I am also very happy to meet the two lab members, Mr. Zhang Tianshun and Mr. Zhao Hanruo. In addition, I would like to extend my gratitude to my friends in office EF501j, Mr. Zheng Huadi,Ms. Zhang Ying, Mr. Han Ziyang, and Ms. Tang Li. I have experienced a wonderful life at school together with them. What's more, I am also grateful to my four roommates, Jiuhai Wang, Fang He, Guangyuan Shi, Yuxiao Ma when I stayed in Homantin Hall during the COVID pandemic period. I suffered from a serious back injury for a long time and could only lie on my bed. They had all took care of me during that difficult period.

Last but not least, I am deeply grateful to my family members, i.e., my grandmother, parents, brother, sister-in-law, and my two adorable nieces, for their boundless love and constant supports over the past four years. I would like to show my deep love for my parents due to their endless love. They always respect my decision and give one hundred percent supporting. Here, I am so grateful to my Mom that she had the most impact on me since I was born. She taught me many knowledge and practical principles during the period of my growing although she never had a chance to attend school. She always cooks so much delicious food every time I return home. However, due to the pandemic, I stayed in Hong Kong for three years and had no chance to return home. Also, I would like to show my deep love to my beloved grandmother. I was broken-hearted when I heard that my grandmother passed away at

the beginning of this year and I had even no chance to see her for the last time. I am so sad that I have no chance to share the good news of my doctoral studies with her. My grandmother shared the happiest memory with me during my growing period. I once promised that I would bring her to my university and travel outside with her. I am so regretful that I have no chance to keep my promise. While she passed away and could not witness my doctoral graduation, I hope that I have met her expectation and she could be proud of me. Notably, I would like to mention my girlfriend and express my deep gratitude for her support and trust during my doctoral study period. It would be impossible for me to complete my study without their understanding and endless support.

Table of Contents

List of Figures

List of Tables

Chapter 1 Introduction

1.1 Background

Due to a rapid growth of data volume, wireless information transmission [1] has attracted increasingly attention from researchers, which has also promoted the further research and development of emerging technologies that can provide users with ultra-high data rates. However, traditional radio frequency communication and wireless transmission technologies are facing the challenges, such as spectrum scarcity and expensive spectrum licensing. Therefore, free-space optical communication that can provide alternatives or supplements for future wireless transmission has been developed.

Recently, ghost diffraction is proposed as a promising method for optical imaging and data transmission. Ghost diffraction can be conducted with coherent light source (e.g., lasers), and coherent light sources have specific advantages for long-distance transmission, e.g., stable frequencies and phase, compared with incoherent light source. Hence, in this thesis, methods are proposed to use coherent light source to transmit information through scattering media with a theory of ghost diffraction.

1.2 Literature review

1.2.1 Ghost diffraction

Ghost diffraction was first introduced in quantum [2–5], which takes advantage of entangled state of two photons generated from spontaneous parametric down-conversion to image an object. Since ghost diffraction was conducted with two-photon pairs using entangled properties, it was originally believed that only photon pairs with quantum entangled properties can achieve ghost diffraction. With further

in-depth research on ghost diffraction, in 2002, Bennink et al. [6] successfully implemented ghost diffraction experiments with thermal light source, which proved that ghost diffraction can also be achieved by using thermal coherent light source. In 2004, Han et al. [7] and Lugiato et al. [8] respectively explained the principle of ghost diffraction from the perspective of statistical optics and quantum mechanics, and reached a unified conclusion that light sources with quantum entanglement characteristics and thermal light source can be applied to conduct ghost diffraction. However, regardless of quantum ghost diffraction or classical ghost diffraction, it is necessary to design an object beam path and a reference beam path respectively using bucket detector and charge-coupled device (CCD), increasing complexity of the imaging system.

With the development of ghost imaging, the research had been shifted from light source to the improvement of imaging quality. In 2008, Shapiro [9] proposed that a ghost diffraction setup can contain only one single-pixel detector, which was named computational ghost imaging. In 2009, Bromberg first introduced spatial light modulator (SLM) [10] which serves as a controllable phase mask for the incident light in ghost diffraction setup, as shown in Fig. 1.1. A laser source is expanded by a pinhole and reflected by a mirror to illuminate the SLM. Many 2D patterns are sequentially embedded into SLM to modulate the input light. Then, the modulated light field interacts with an object, and light intensity is collected by a single-pixel bucket detector (BD). The single-pixel light detection process can be expressed as

$$I_i = \sum_x \sum_y P_i(x,y) O(x,y), \ \ (i = 1,2,3,...,M), \tag{1.1}$$

where P_i denotes the *i*-th 2D pattern embedded into the SLM, O denotes the object placed before the BD, I_i denotes the *i*-th collected light intensity, (x,y) denotes the

coordinate in spatial domain, and M denotes the total measurement number. During image reconstruction, a correlation algorithm is applied, which can be described by

$$O_{GI}(x,y)=\frac{1}{M}\sum_{i=1}^{M}\left(I_i-\langle I_i\rangle\right)\left(P_i-\langle P_i\rangle\right), \tag{1.2}$$

where O_{GI} denotes the reconstructed object, and $\langle\bullet\rangle=\sum i\bullet/M$ denotes the ensemble average value after M measurements.

Moreover, differential ghost imaging [11], normalized ghost imaging [12], correspondence ghost imaging [13] and compressed ghost imaging [13–18] have been proposed sequentially to improve the quality or speed of imaging process. Since then, single-pixel imaging has been developed in various fields, such as three-dimensional imaging [19, 20], pure phase object imaging [21, 22], terahertz imaging [23–25], remote sensing [26], X-ray imaging [27, 28], spectrum-resolved imaging [29,30], high-order correlation imaging [31,32]. Compared with conventional imaging methods, ghost imaging shows great advantages as follows: 1) ghost diffraction setup is flexible to design; 2) single-pixel detector is more cost-effective and easier to use than conventional pixelated detectors in some applications, especially in terms of overbroad wavebands.

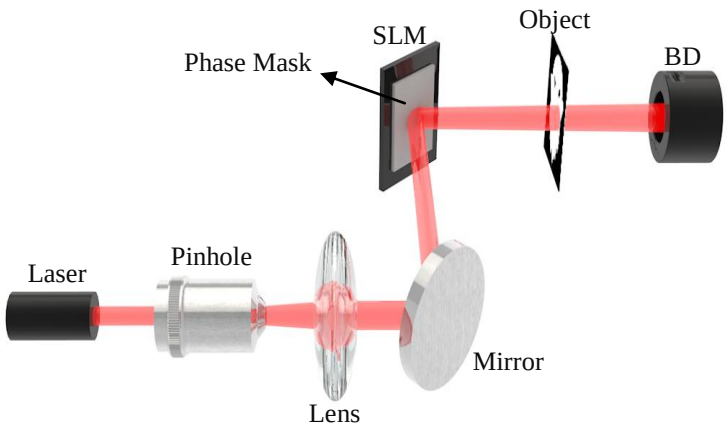

Figure 1.1 Schematic of ghost imaging with only one single-pixel detector.

The theory of ghost diffraction is generally used for imaging, and it can be used as a method to realize phase retrieval. Borghi et al. [33] designed an optical interferometry technique to achieve phase reconstruction in ghost diffraction. In addition, Han et al. [34] obtained the phase of unknown objects in ghost imaging using a two-step reconstruction algorithm, offering numerical iteration method.

Furthermore, an extension of ghost diffraction from spatial domain to time domain has been investigated theoretically and experimentally by considering space-time duality in optics [35–44]. In temporal ghost imaging, the light beam was split into two optical arms, called “reference” and “object”. In the object beam arm, the light transmits through a “time object” and is detected using a single-pixel detector that cannot properly resolve the time object. In the reference beam arm, the light that does not interact with temporal object is detected using a fast single-pixel detector. A typical temporal ghost imaging setup is shown in Fig. 1.2.

Temporal ghost imaging [45] can be used to realize information transmission. Inspired by temporal ghost imaging, ghost diffraction is promising for information transmission process via light field modulation, and the desired information can be retrieved at the receiving end.

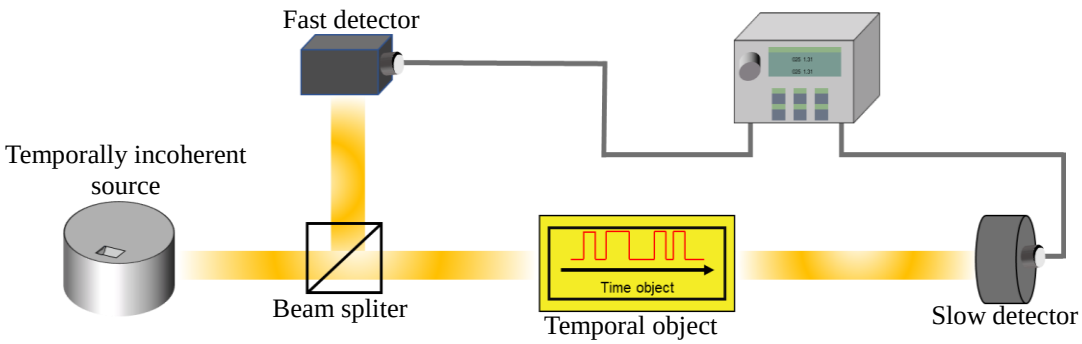

Figure 1.2 Schematic of temporal ghost imaging.

1.2.2 Optical transmission through scattering media

Optical transmission in free space often encounters different kinds of scattering media, and the quality of signal is often affected by the absorption or reflection effects occurring in scattering media. In this Section, two aspects of scattering media are discussed, i.e., scattering media and non-line-of-sight environment. In terms of scattering media (e.g., static scattering media and dynamic scattering media), random scatter can have a detrimental impact on imaging, sensing and communication areas. Various kinds of scattering phenomena (e.g., non-selective scattering, Mie scattering, and Rayleigh scattering) are classified based on the size of particles in scattering media and wavelength of the incident light. Non-line-of-sight transmission environment is also introduced in this Section as a kind of more complex scattering media. Light is often blocked by different kinds of obstacles (e.g., rough surface, walls), and the absorption and reflection process occurs simultaneously when light transmits in non-line-of-sight environment.

1.2.2.1 Scattering media

Optical transmission through scattering media pertains to the propagation of light through materials, e.g., biological tissues, clouds, fog, and turbid water [46–48]. Scattering media cause light to scatter and change direction multiple times, resulting in a diffuse beam that spreads out in numerous directions [49–54]. Scattering phenomenon severely degrades the performance of optical transmission or imaging through scattering media [55–70]. In fact, when an input light field passes through scattering media, it significantly alters the properties of light intensity [55–62], polarization states [63–68], and optical field information [69,70], resulting in substantial changes. Light intensity diminishes as it traverses a scattering medium due

to absorption and scattering. The degree of attenuation is determined by various factors, such as the density and size of scattering particles and wavelength of the light. Moreover, the scattering media can impact the polarization state of light. Scattering particles induce depolarization, leading to a mixed or scrambled polarization state. The extent of this depolarization depends on the media properties and the initial polarization state of the incoming light. Scattering particles can induce wavefront distortion [71] and reduced coherence in the presence of scattering media, resulting in the loss of optical field information. Fog and smoke represent prevalent types of scattering media within the atmospheric environment, exerting considerable influence on the performance of optical communication and imaging systems. Fog emerges when airborne water droplets condense, while smoke consists of minute particles and gases. Light scattering and absorption can induce significant attenuation and distortion of signals, thereby diminishing communication and imaging system range and quality. In underwater and atmospheric environments (e.g., fog and smoke), the scattering and absorption properties can vary based on factors, such as temperature, humidity, and particle size distribution. It is challenging to achieve precise transmission and reception of information through scattering media.

Various techniques have been introduced to address the challenge of optical transmission or imaging through scattering media. Wavefront shaping techniques have been widely utilized to realize optical transmission through scattering media. Wavefront shaping method [72] was firstly proposed in 2007, and coherent light is focused through opaque scattering media by control of the incident wavefront. Wavefront shaping methods can be utilized to measure transmission matrix [73] of a complex scattering environment. Transmission matrix of a fixed scattering media is further used to control light transmission in disordered media. The incident optical

field information and the output optical field information recorded by a CCD camera are correlated to retrieve the transmission matrix of a typical system [74]. A complete description of transmission matrix can be obtained with a large amount of collected data. Different kinds of transmission matrices of different scattering media might have huge differences. Hence, a slight change in the scattering medium may result in a completely different transmission matrix. The technique is time-consuming, data-demanding and highly sensitive to model errors. In practice, wavefront shaping method can be realized with SLM, which can impose spatially-varying modulation on the incident wavefront. Many iterative optimization algorithms [75–77] are proposed to obtain the desired wavefront information. Wavefront shaping methods often utilize a prior knowledge of the typical scattering media to acquire better optimization result. Another method utilized the optical channel information [78] to realize optical transmission through scattering media, named optical-channel-based intensity streaming. Optical encoding and transmission are realized with linear intensity operation among different optical channels. The proposed optical-channel-based intensity streaming method manipulates light and transmits optical information through linear optical encoding process.

In addition, time-resolved imaging [79] exploits the temporal features of scattered light to extract information about the media. Polarimetric imaging [80] can additionally unveil the shape, orientation, and composition of objects or scenes in a scattering environment. Another promising strategy involves the implementation of adaptive optics, which entails employing deformable mirrors and wavefront sensors to rectify the distortion caused by the medium. This technique has been effectively applied in astronomy to mitigate atmospheric turbulence and enhance telescope resolution. Blue-green laser communication [81] has been developed to enhance both

the range and reliability of underwater communication. Deep learning techniques [82–86] have shown promising results in this regard. Machine learning algorithms can be trained to extract valuable information from scattered light, such as object location and shape in biological tissue or turbid water composition. This has a potential to revolutionize optical imaging and sensing, particularly in situations where traditional techniques struggle to penetrate through scattering media. Furthermore, novel materials and structures that enhance the transmission of light through scattering media are being developed. For instance, photonic crystals [87] and metamaterials [88,89] can be used to control light scattering and enhance its transmission through turbid media. These materials can be designed to possess specific properties [90], such as a high refractive index, to reduce scattering and enhance the resolution of imaging and sensing systems.

1.2.2.2 Non-line-of-sight environment

Non-line-of-sight transmission and imaging pertain to the capability of transmitting, receiving optical signals, or capturing images even when the direct line of sight between the transmitter and receiver is obstructed by an obstacle [91–96], as shown in Fig. 1.3. Rough reflective surfaces existing in non-line-of-sight environment can be seen as scattering media. Non-line-of-sight transmission process often exists in various communication or imaging fields. For instance, light transmission in underwater environment [92] often encounters stones, rocks, and suspended particles, which would block the transmission path of light transmission and arouse severe attenuation and distortion. In addition, non-line-of-sight environment often poses threats to optical communication [95] and imaging [96] in the indoor environment.

Non-line-of-sight transmission holds significance in many areas, e.g., autonomous vehicles, search and rescue operations, and military reconnaissance.

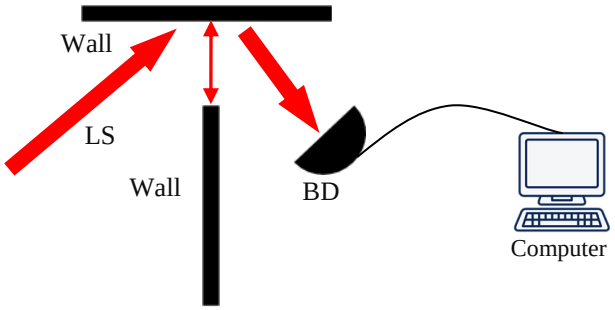

Figure 1.3 Non-line-of-sight transmission scheme. LS: light source. BD: single-pixel bucket detector.

Various techniques have been proposed for achieving non-line-of-sight transmission and imaging. Time-of-flight (TOF) measurements of light [97–100] are often applied in the field of non-line-of-sight transmission and imaging. TOF technique involves measuring the duration of light travelling from the transmitter to the obstacle and subsequently to the receiver. By analyzing the time delay and light intensity, it is feasible to reconstruct an image of the object hidden behind the obstacle. Photon-counting detectors [101–103] are capable of detecting scattered light in non-line-of-sight environment. Low-noise detectors and imaging algorithms have been utilized in photon-counting non-line-of-sight imaging [101]. Photon-counting non-line-of-sight imaging [104] can be realized by utilizing a single-photon avalanche diode detector to detect scattered light and reconstruct an image of an obscured object. In addition, sound waves [105] or radio waves [106] can be utilized to explore hidden objects and acquire their location and shape. In an acoustic non-line-of-sight imaging system [106], sound waves are used to detect objects concealed behind walls.

Therefore, optical transmission through scattering media is a multifaceted and challenging problem in optics. Various techniques are proposed to realize optical transmission through scattering media, including structured illumination,

enhancement of contrast, and theoretical algorithms. However, traditional methods for imaging through scattering media are inadequate due to their huge computational demands, low resolution, and limited application ranges.

1.2.3 Optically secured transmission

Optical encryption is an advanced technique that utilizes optics and photonics techniques to ensure the confidentiality of transmitted information. Optical encryption has gained considerable attention in recent years due to its high level of security, high transmission rate, and low probability of interception. Optical encryption methods are often applied in different fields, e.g., information encryption [107,108], physically secured wireless transmission [109–112], and encrypted visible light communication (VLC) [113,114].

Double random phase encryption (DRPE) [107] is a widely adopted optical encryption technique utilizing two random phase masks to encode and decode information. The first random phase mask encodes the original image, and the second mask multiplies the encoded image to generate a scrambled image. Original image can only be recovered with correct keys, e.g., inverse of the second random phase mask. DRPE has found widespread applications in various areas, e.g., image and video encryption.

Physically secured optical transmission (PSOT) is an optical encryption technique that utilizes unique physical properties of the transmission channel to enhance the security of wireless communications. The characteristics of the wireless channel include signal strength, frequency response, and channel impulse response. The key is generated by measuring the wireless channel between the transmitter and the receiver. PSOT eradicates the necessity of exchanging encryption keys between the transmitter and receiver, reducing the risk of key interception and enhancing the

efficiency of the encryption process. PSOT is resistant to replay attacks since the PSOT key is generated based on the constantly changing physical properties of the wireless channel. PSOT has been applied in various wireless communication systems, such as Wi-Fi, Bluetooth, and cellular networks.

Encrypted VLC is a novel optical encryption technique that utilizes visible light to transmit encrypted information. Information can be encoded into a sequence of light pulses, which are modulated using the encryption key. The encrypted information can only be retrieved using correct encryption key. Encrypted VLC has been employed in diverse applications, including indoor positioning, secure data transmission, and augmented reality. Some researchers have proposed various encryption methods like quantum key distribution [115] or chaos-based encryption [111]. Furthermore, researchers have proposed hybrid encryption methods that integrate optical encryption with other encryption techniques, such as electronic encryption [116], to augment security of the information.

However, implementing optical encryption techniques still has faced numerous challenges. One of the most significant challenges is the susceptibility of optical systems to external noise and interference [117,118]. Various factors, such as atmospheric turbulence, temperature changes, and mechanical vibrations, can introduce noise and distortion into the optical signal, affecting the quality and security of the encryption. Another challenge is a need for specialized equipment and expertise to implement optical encryption [119]. Laser, phase modulators, and spatial light modulators are specialized optical devices and components required for optical encryption that can be costly and challenging to obtain. Despite the challenges, optical encryption techniques have shown a potential in various applications. For instance, optical encryption can secure communication in military and government applications,

financial transactions, and healthcare systems. Optical encryption can also secure sensitive data in cloud computing and IoT devices, where traditional electronic encryption techniques may not suffice.

1.3 Problems and motivation statement

Based on the aforementioned introduction, single-pixel optical encoding methods are studied for optical transmission framework in this thesis, which is aimed to solve key scientific problems in optical wireless transmission. The challenges and research motivations are described as follows:

(1) It has been well recognized that when 2D random patterns and coherent light source are directly applied, it is not possible to optically transmit data through scattering media with high fidelity. It is desirable to explore an easy-to-implement and feasible way to apply ghost diffraction and optical encoding method to enable high-fidelity optical information transmission through scattering media in free space. It is also desirable that 2D arrays of random numbers can be generated and used as information carriers to conduct optical transmission through scattering media in free space with high fidelity and high robustness.

(2) Few work was conducted on optical data transmission through dynamic scattering media, e.g., dynamic smoke or dynamic turbid water. Free-space optical analog-signal transmission in a dynamic smoke environment is challenging, and it is desirable to investigate the influence of dynamic smoke environment on high-fidelity free-space optical analog-data transmission.

(3) Obstacles in the transmission channel would block optical wave. Optical analog-signal transmission in non-line-of-sight environment is still challenging, and it is desirable to investigate new schemes for high-fidelity free-space optical analog-data transmission through dynamic scattering in non-line-of-sight environment.

(4) Security of optical wireless transmission has not been fully studied in harsh environments. A promising approach to solving the problem is that the computer-generated keys can be used with physically-generated keys to achieve high security. It is desirable to develop a feasible and easy-to-implement method to enable optical data transmission through scattering media in free space with high fidelity and high security.

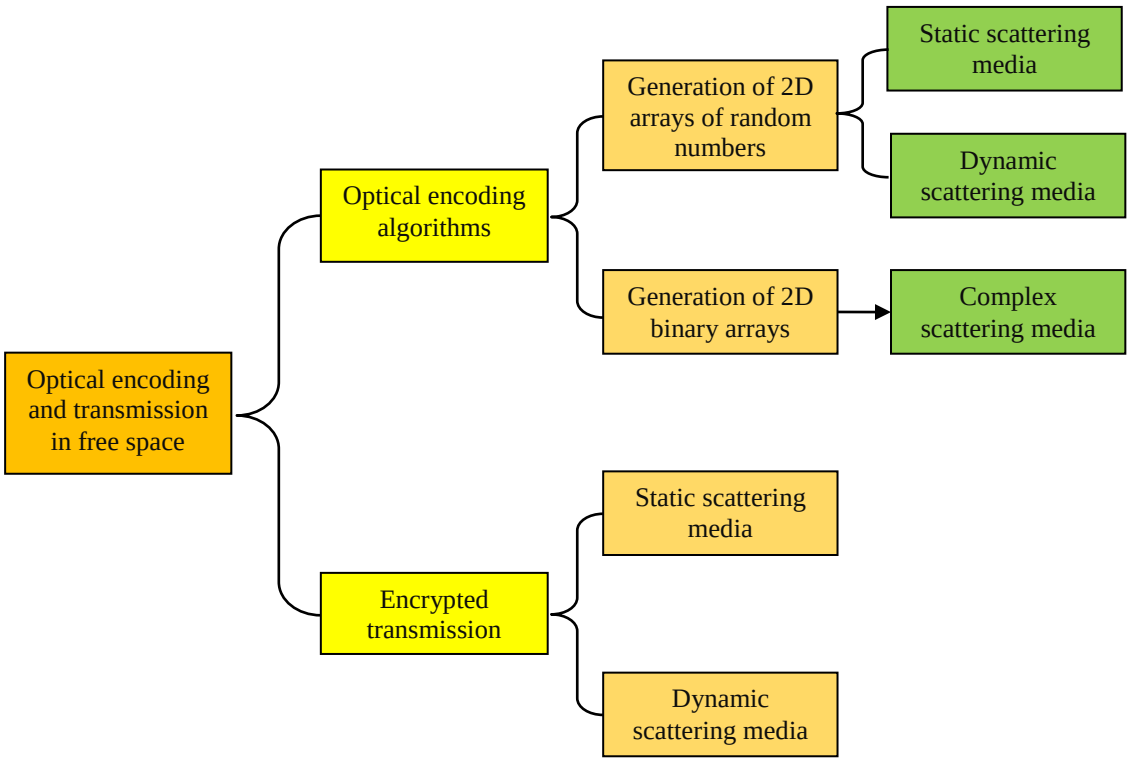

Figure 1.4 Structure of the research questions in this thesis.

The main objective of this thesis is to design optical encoding algorithms to realize optical transmission through scattering media in free space. The main works conducted in this thesis include two aspects, e.g. optical encoding algorithm and encrypted transmission. The main research work of this thesis is outlined in Fig. 1.4.

1.4 Thesis structure

This Ph.D. thesis is composed of six chapters, and the contents in Chapters 2-6 are described as follows:

Chapter 2 presents a method to realize free-space optical transmission through scattering media. 2D arrays of random numbers are applied as information carriers, and the concept of ghost diffraction and transmission is introduced. Experimental results verify the feasibility of the proposed method to realize high-fidelity optical wireless transmission through static scattering media.

Chapter 3 presents a high-fidelity optical transmission through dynamic scattering media. A fixed reference pattern is repeatedly utilized as temporal carriers to temporally correct the transmission errors aroused by dynamic scattering media.

Chapter 4 presents a scheme to realize optical transmission in dynamic and complex environment using binary encoding with a modified differential method. In this Chapter, the proposed scheme realizes optical transmission at a potentially higher rate and the fewer number of random patterns is utilized.

Chapter 5 focuses on the secured optical data transmission through scattering media. An encryption system is proposed to realize optically secured transmission in harsh environments. Optically secured transmission through static and dynamic scattering media is respectively presented. Experimental results verify effectiveness and feasibility of the proposed optically secured transmission through scattering media in free space.

Chapter 6 summarizes the research findings, and contributions of the thesis are described. The future work is also described in this Chapter.

Chapter 2 Ghost transmission through static scattering media

2.1 Introduction

Optical information transmission through scattering media is always considered as a significant challenge, since optical field could be severely destroyed in scattering environment. A number of methods [1,120–122] have been developed to realize information transmission through scattering media. A typical method is based on wavefront shaping [121], in which phase or amplitude modulation is usually conducted to control light to focus at a certain point of the output plane. Manipulation of interference among different optical channels is also applied to establish effective information channels [122], and amplitude or phase information of light through scattering media is further used as a feedback to optimize optical field. However, conventional methods could be complex and time-consuming due to the optimization and precise stability requirements. In addition, high-fidelity and high-robustness free-space optical data transmission through scattering media has not been realized.

To solve key scientific problems in conventional free-space optical transmission through scattering media, ghost diffraction can be explored to provide a promising solution. Ghost diffraction originated from quantum [2,3], in which the entangled state of two photons generated from spontaneous parametric down-conversion was used to realize the imaging. Later, ghost diffraction was further proved to be feasible with classical thermal light [6,8]. Ghost diffraction has been widely applied, e.g., three-dimensional reconstruction [20,21,123], phase object recovery [22,124], Terahertz [24,25], optical encryption [125–127] and X-ray imaging [7,128]. In ghost diffraction process with only one single-pixel bucket detector, a number of 2D

patterns [19,129–131] need to be generated and sequentially embedded into a spatial light modulator (SLM). Then, these 2D patterns are illuminated to propagate at object wave path, and light intensity is collected by using a single-pixel bucket detector. The object information can be recovered by using correlation algorithms [19,129–131] with the 2D patterns and the collected intensity. It is required that a large number of patterns are usually applied to enhance quality of the recovered object image and mitigate environmental and detection noise. However, in ghost diffraction, the 2D patterns embedded into SLM usually contain no meaningful information about the data or object, and cannot be directly employed as information carriers for optical data transmission. Moreover, a non-correlation relationship usually exists among the 2D patterns, and there is also no determined relationship between the 2D patterns and the recorded intensity. Therefore, high-fidelity data transmission through scattering media is not feasible in traditional ghost diffraction, when the 2D patterns are directly used and coherent light source is applied. It is highly desirable to explore an easy-to-implement and feasible way to apply ghost diffraction and optical modulation method to enable high-fidelity ghost diffraction and optical information transmission through scattering media in free space. It is also desirable that 2D arrays of random numbers can be generated and directly used as information carriers to conduct ghost transmission through scattering media in free space with high fidelity and high robustness.

In this Chapter, optical ghost diffraction using a series of 2D arrays of random numbers and coherent light source is proposed to realize optical field modulation and optical information transmission in free space through scattering media, which can provide an easy-to-implement way with high fidelity and high robustness. Instead of a direct realization of signal transmission with a laser, various types of ghosts, e.g.,

analog signals and grayscale images, are first encoded into 2D arrays of random numbers as information carriers. The generated 2D arrays of random numbers are sequentially embedded into SLM, and are sequentially illuminated to propagate through scattering media in free space. A single-pixel bucket detector is used at the receiving end to collect the intensity. Original signals or images can be retrieved at the receiving end using a simple retrieval operation. The main contributions of this work are described as follows: (1) To the best of my knowledge, it is the first time to realize free-space optical signal transmission through scattering media using a series of 2D arrays of random numbers as information carriers. (2) An entirely new method is proposed to design a series of 2D arrays of random numbers to realize high-fidelity and high-robustness free-space optical information transmission through scattering media. (3) Optical experiments are conducted to analyze the effect of different parameters and different environments on free-space optical information transmission by utilizing the proposed method. (4) Light intensity is collected by using a single-pixel bucket detector so that the collimation and alignment problem of free-space optical transmission channel can be solved at the receiving end. Optical experimental results and observation could shed light on free-space optical information transmission through scattering media. The corresponding publication of this Chapter is listed as follows:

Yonggui Cao, Yin Xiao, Zilan Pan, Lina Zhou, and Wen Chen, "Direct generation of 2D arrays of random numbers for high-fidelity optical ghost diffraction and information transmission through scattering media," Optics and Lasers in Engineering, **158**, 107141 (2022).

2.2 Theory of wave propagation through scattering media

In this Section, a detailed introduction to the theory of wave propagation through scattering media is given. Theory of transmission matrix is utilized to obtain the relationship between input plane wave field and the output wave field after the plane wave propagates through scattering media.

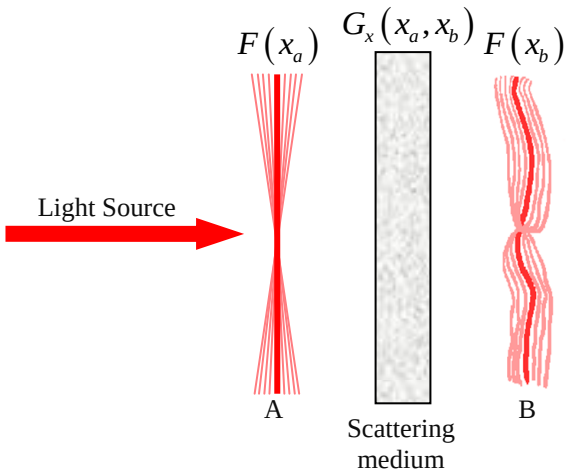

Figure 2.1 Light propagating through thin diffusing slabs [46].

Traditionally, when light transmitting through scattering media, transmission matrix G_x is often used to describe a relationship between the spatial input and output optical modes. Transmission matrix is often modeled as a random matrix with complex Gaussian elements, and there is also a macroscopic structure in transmission matrix, which is particularly noticeable for thin slabs: a point source at the input plane would diffuse into a diffuse spot at the output.

To theoretically derive the relationship between output and input optical field intensity, continuous fields $F(x_a)$ and $F(x_b)$ along the front and back surfaces of a scattering slab are considered. Wave propagation through any linear medium can be described by a complex transmission function $G_x(x_a, x_b)$ such that

$$F(x_b) = \int G_x(x_a, x_b) F(x_a) d^2 x_a, \tag{2.1}$$

where $F(x_a)$ denotes the incident field on side A, and $F(x_b)$ denotes the output field on side B, x_a and x_b is the spatial coordinates in arbitrary planes.

After that, the k-space intensity propagator $L_k(k_b, k_a)$ needs to be calculated, which defines the average transmitted intensity when plane wave passes through scattering medium. By convention, the intensity is defined as a function of propagation direction k_b as, $I(k_b) \equiv |F(k_b)|^2$.

To derive the theorem of intensity propagation, a truncated plane wave is designed with normalized power:

$$F_H(x_a) = \frac{J_H(x_a)}{\sqrt{H}} e^{ik_a \cdot x_a}, \qquad J_H(x_a) = \begin{cases} 1 & \textit{for } x_a \textit{ inside a square area } H \\ 0 & \textit{otherwise} \end{cases}. \quad (2.2)$$

As a result of normalization, $\int_H |F_H(x_a)|^2 d^2 x_a = 1$ is obtained. Note that while wave is truncated to a square area H in Eq. (2.2), I take the limit area $H \to \infty$ in the following part. Following Eq. (2.1), the incident field $F_H(x_a)$ generates the following transmitted field.

$$F(x_b) = \int G_x(x_a, x_b) \frac{J_H(x_a)}{\sqrt{H}} e^{ik_a \cdot x_a} d^2 x_a. \quad (2.3)$$

So the k-space intensity propagator is defined as the average spectrum intensity at side B, when an incident plane wave with wavevector k_a illuminates side A [46].

$$\begin{aligned} L_k(k_b, k_a) &= \lim_{H \to \infty} \left\langle \left| \int e^{-ik_b \cdot x_b} F(x_b) d^2 x_b \right|^2 \right\rangle \\ &= \left\langle \frac{1}{H} \iint e^{-ik_b \cdot x_b} G_x(x_a, x_b) J_H(x_a) e^{ik_a \cdot x_a} d^2 x_a d^2 x_b \right. \\ &\times \left. \iint e^{ik_b \cdot x_{b'}} G_x^*(x_{a'}, x_{b'}) J_H(x_{a'}) e^{-ik_a \cdot x_{a'}} d^2 x_{a'} d^2 x_{b'} \right\rangle. \end{aligned} \quad (2.4)$$

The coordinate transforms $x_{a'} \to x_a - \Delta x_a$ and $x_{b'} \to x_b - \Delta x_b$ are applied, and Eq. (2.4) is rewritten as

$$\begin{aligned} L_k\left(k_b, k_a\right) &= \lim_{H\to\infty} \frac{1}{H} \iiiint \left\langle G_x\left(x_a, x_b\right) G_x^*\left(x_{a'}, x_{b'}\right)\right\rangle \\ &\times J_H\left(x_a\right) J_H\left(x_a - \Delta x_a\right) e^{ik_a \cdot \Delta x_a} e^{-ik_b \cdot \Delta x_b} d^2 x_a d^2 x_b d^2 \Delta x_a d^2 \Delta x_b. \end{aligned} \tag{2.5}$$

The shift-shift correlation function Q_x is defined under the circumstance $H \to \infty$.

$$\begin{aligned} Q_x\left(\Delta x_a, \Delta x_b\right) &= \lim_{H\to\infty} \frac{1}{H} \iint J_H\left(x_a\right) J_H\left(x_a - \Delta x_a\right) \\ &\times \left\langle G_x\left(x_a, x_b\right) G_x^*\left(x_{a'}, x_{b'}\right)\right\rangle d^2 x_a d^2 x_b, \\ &= \lim_{H\to\infty} \frac{1}{H} \int_H \int_H \left\langle G_x\left(x_a, x_b\right) G_x^*\left(x_a - \Delta x_a, x_b - \Delta x_b\right)\right\rangle d^2 x_a d^2 x_b. \end{aligned} \tag{2.6}$$

Note that correlation function in Eq. (2.6) can be defined in arbitrary conditions even when the medium is not shift-invariant. However, defining a correlation function does not make sense unless the medium is statistically invariant to translations over the analysis area.

Then, combining Eqs. (2.5) and (2.6) so that [46]:

$$L_k\left(k_b, k_a\right) = \iint Q_x\left(\Delta x_a, \Delta x_b\right) e^{ik_a \cdot \Delta x_a} e^{-ik_b \cdot \Delta x_b} d^2 \Delta x_a d^2 \Delta x_b. \tag{2.7}$$

Inverting this Fourier transform to give

$$Q_x\left(\Delta x_a, \Delta x_b\right) = \iint L_k\left(k_b, k_a\right) e^{-ik_a \cdot \Delta x_a} e^{ik_b \cdot \Delta x_b} d^2 k_a d^2 k_b. \tag{2.8}$$

For convenience, changing the coordinates of L_k to $k \equiv k_a$ and $\Delta k \equiv k_b - k_a$ to get

$$Q_x\left(\Delta x_a, \Delta x_b\right) = \iint L_k'\left(k; \Delta k\right) e^{i\Delta k \cdot \Delta x_b} e^{-ik\left(\Delta x_a - \Delta x_b\right)} d^2 k d^2 \Delta k, \tag{2.9}$$

where this is still a general expression.

In the above discussion, the diagonal features of transmission matrix is explained, and 2D Fourier Transform provides us a direct explanation why the transmitted intensity of light through scattering media has a close relationship with the diagonal value of Fourier transformed transmission matrix.

In addition, the intensity propagator matrix is proportional to the correlation function of transmission matrix.

$$\mathbf{E_{out}} = \begin{bmatrix} E_{out,1} \\ E_{out,2} \\ \vdots \\ E_{out,m} \end{bmatrix} = \begin{bmatrix} t_{11} & t_{12} & \cdots & t_{1n} \\ \vdots & \vdots & \vdots & \vdots \\ t_{m1} & t_{m2} & \cdots & t_{mn} \end{bmatrix}_{m\times n} \begin{bmatrix} E_{in,1} \\ E_{in,2} \\ \vdots \\ E_{in,n} \end{bmatrix} = \mathbf{TE_{in}}, \qquad (2.10)$$

where t_{mn} denotes the complex coefficient of transmission matrix **T**.

Through Eq. (2.10), the result of transmitted intensity is derived

$$\begin{aligned} I^{\text{out}} &= \sum_m \left| \sum_n t_{mn} E_{in,n} \right|^2 \\ &= \sum_m \sum_n \left| t_{mn} \right|^2 \left| E_{in,n} \right|^2 + \sum_m \sum_n \sum_{n' \neq n} t_{mn} t_{mn'}^* E_{in,n} E_{in,n'}^* . \end{aligned} \qquad (2.11)$$

The first term of Eq. (2.11) can be regarded as the sum of the diagonal elements of the transmission matrix autocorrelation matrix, and the second term of Eq. (2.11) can be regarded as the sum of the cross-correlation of elements in transmission, which is equal to zero. Due to scattering statistics, the transmission matrix can be regarded as a Gaussian distributed matrix, and the cross terms of auto-correlation matrix of T are all small values. In other words, the contribution of the coefficient $t_{mn} t_{mn'}^*$ is negligible compared with the coefficient $\left| t_{mn} \right|$.

In this Section, a detailed analysis to the theory of wave propagation through scattering media is given. Theoretically, it is proved that the intensity of input optical field and output optical field has a proportional relationship, and the scaling factor is

equal to the sum of diagonal elements of the correlation matrix of scattering medium transmission matrix. Hence, it is explained why optical information can be retrieved with a single-pixel detector through decoding process.

2.3 Principles

An optical model of the proposed optical ghost diffraction and information transmission is shown in Fig. 2.2. Data to be transmitted are encoded into 2D information carriers, and the 2D information carriers are embedded into SLM sequentially. A laser is modulated by the 2D information carriers, and the modulated light propagates through scattering optical channel which is composed of diffusers (e.g., ground glass) and reflective media (e.g., an A4 paper). Light intensity is collected by a single-pixel bucket detector at the receiving end and is utilized to retrieve original signal.

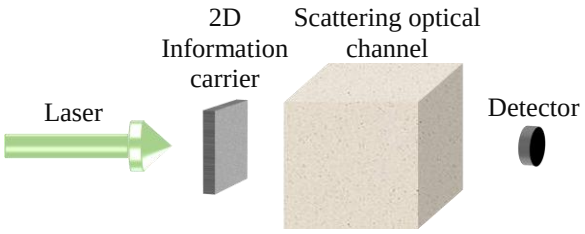

Figure 2.2 An optical model of the proposed optical ghost diffraction and information transmission scheme.

In the proposed method, the signal or image is first encoded into 2D arrays of random numbers. The proposed generation process of 2D arrays of random numbers is described as follows:

(1) Enlarge each original signal pixel (S) by using a magnification factor (M): $A = M \times S$;

(2) Arbitrarily generate a random matrix P with real and non-negative values (i.e., from 0 to 1);

(3) Calculate a difference *y* between the enlarged value *A* obtained in step (1) and the sum of the generated matrix P: $y = A - \mathrm{sum}(\mathrm{P})$;

(4) Generate another matrix C with real and non-negative values, sum of whose pixel values is equivalent to absolute value of the difference *y* obtained in step (3): $\mathrm{sum}(\mathrm{C}) = |y|,$ where | | denotes an absolute operation;

(5) When the difference obtained in step (3) is negative, a 2D array corresponding to the enlarged data in step (1) is generated by calculating the difference between the matrix P and the matrix C. When the difference *y* obtained in step (3) is positive, a 2D array corresponding to the enlarged data in step (1) is generated by the addition of matrix P and matrix C:

$$\tilde{\mathrm{P}} = \begin{cases} \mathrm{P} + \mathrm{C}, & y >= 0 \\ \mathrm{P} - \mathrm{C}, & y < 0 \end{cases}. \tag{2.12}$$

To analyze the selection of different parameters in the proposed method aforementioned, original signal, i.e., acting as ghost, is normalized to be within a range from 0 to 1. (i) Since the generated 2D arrays of random numbers are sequentially embedded into the SLM, the large size of 2D arrays, e.g., 256×256 or 512×512 pixels, is required in order to provide sufficient light intensity in the experiments. (ii) Although the magnification factor used in the proposed method can be arbitrarily selected, it needs to satisfy that the enlarged value obtained in step (1) is comparable to the total pixel number of its correspondingly generated 2D array. (iii) The matrix F is generated in a random process. A difference value y is first calculated by using a subtraction operation between the enlarged value obtained in step (1) and the sum of random matrix P, whose absolute value consists of an integer value denoted as *p* and a decimal (fractional part) denoted as *q*. Then, the steps for the generation of matrix C are as follows: A random sequence T with a length of $2 \times p$ is

first generated, of which the upper half are random numbers between 0 and 1 and the lower half are obtained by calculating the difference between 1 and each value of the upper half. Then, an all-zero matrix with the same size of the matrix P is generated, and pixels with the number of $2 \times p+1$ are randomly selected from this all-zero matrix. Finally, the decimal (fractional part) q and all values of the random sequence T are arbitrarily assigned to those randomly-selected pixel positions with the number of $2 \times p+1$ in order to generate the matrix C.

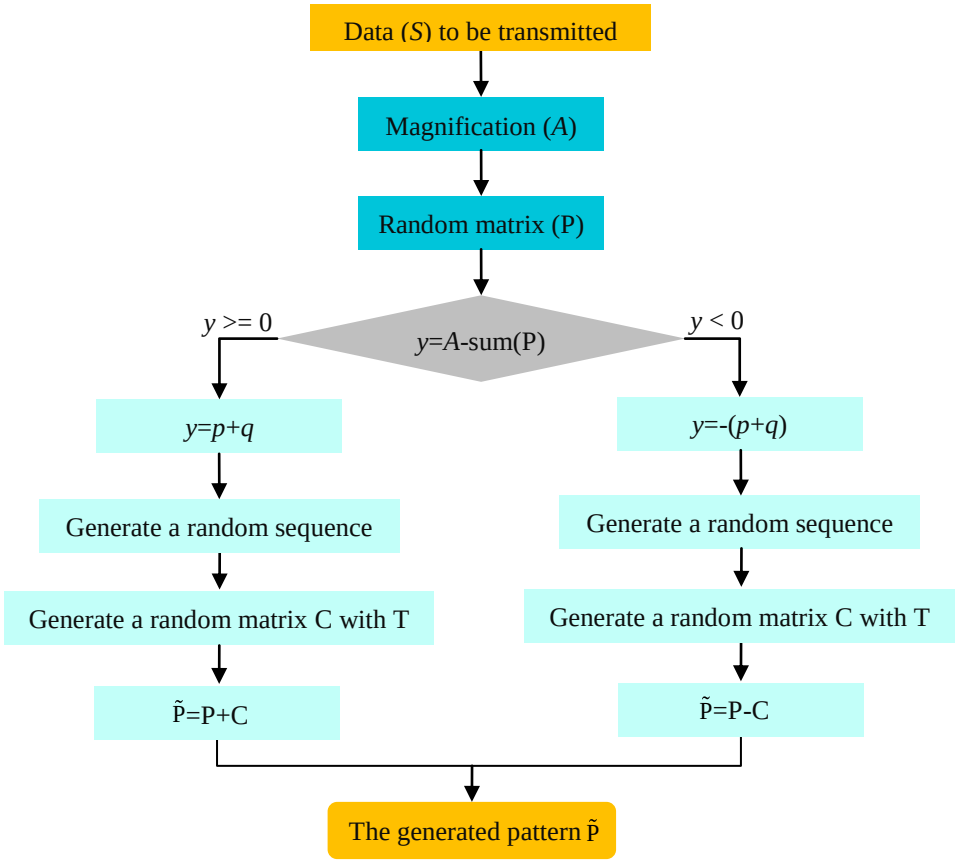

Figure 2.3 A flow chart of the proposed pattern generation algorithm.

A flow chart of the proposed pattern generation process is shown in Fig. 2.3, and important and relevant parameters have been described. The following objective can be achieved: the sum of the generated 2D array of random numbers is equivalent to the enlarged value obtained in step (1), and each signal pixel to be transmitted is individually encoded into a 2D array of random numbers.

The whole encoding and retrieval process is shown in Fig. 2.4. For an original signal (as ghost, i.e., S_i, i=1,2,3,…,K) with K pixels to be transmitted, the proposed whole process is as follows: Each signal pixel is first encoded into a 2D array of random numbers ($\tilde{P}_i$, i=1,2,3,…,K) using the proposed algorithm aforementioned. To fully mitigate environmental and detection noise, a differential method is further developed to convert each generated 2D array of random numbers into two 2D

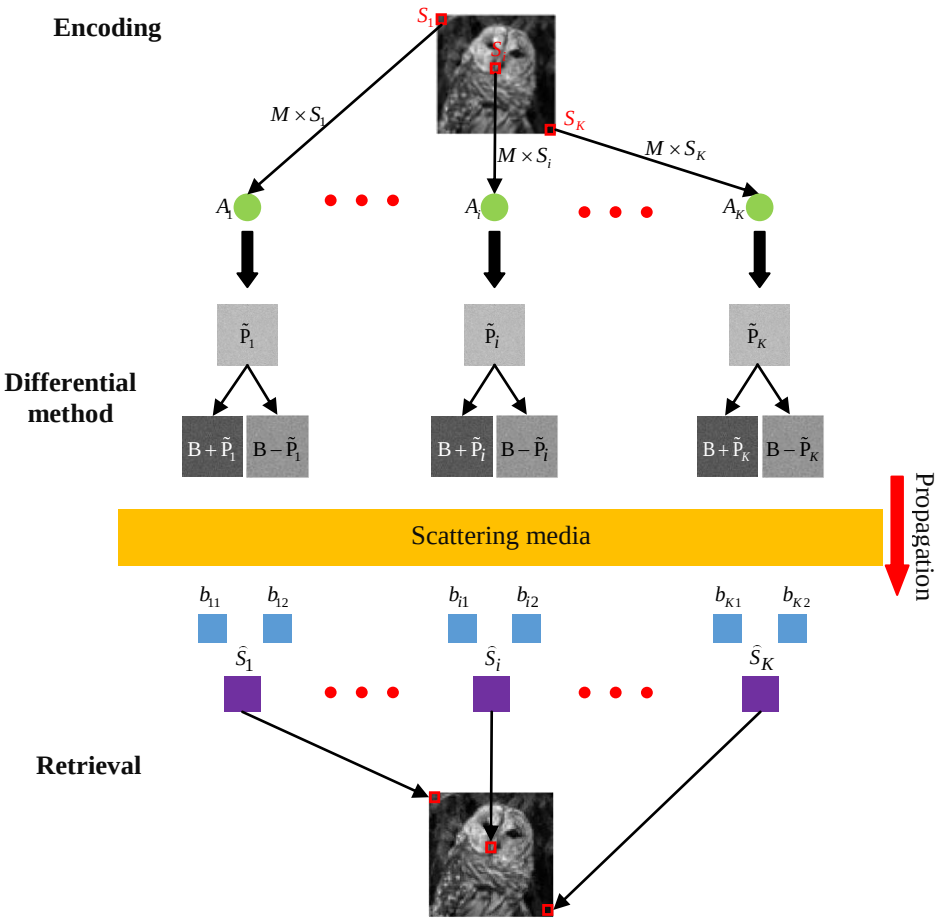

Figure 2.4 A flow chart of the proposed optical information encoding and retrieval process.

arrays of random numbers (i.e., $B+\tilde{P}_i$ and $B-\tilde{P}_i$) with a real and positive constant B to remove negative values. Then, for each pixel of the signal to be transmitted, the two generated 2D arrays of random numbers are sequentially embedded into an amplitude-only SLM in Fig. 2.5, and two intensity points (b_{i1}, b_{i2}) can be sequentially collected by a single-pixel bucket detector. In information retrieval process, a simple

subtraction operation with these two collected intensity values (b_{i1}, b_{i2}) is carried out to retrieve each signal pixel value (S_i), which has a close relationship with its corresponding pixel value in original signal, i.e., with a scaling factor. According to the principles of wave propagation through scattering media [46,132], intensity I_{out} collected by single-pixel bucket detector can be described by $I_{out} \approx u\left|E_n\right|^2$, where u denotes a scaling factor and E_n (n=1, 2, 3,…) denotes each element of wavefront information. In a certain transmission environment, the scaling factors corresponding to different 2D arrays of random numbers can be considered as the same one, and the scaling factors can be easily obtained during the experimental process. Hence, the original signal can be retrieved with high fidelity by using the scaling factor and the two collected intensity values (b_{i1}, b_{i2}). The proposed method is able to realize high-fidelity optical ghost diffraction and information transmission through scattering media in free space, when a single-pixel bucket detector is used at the receiving end.

2.4 Experimental results and discussion

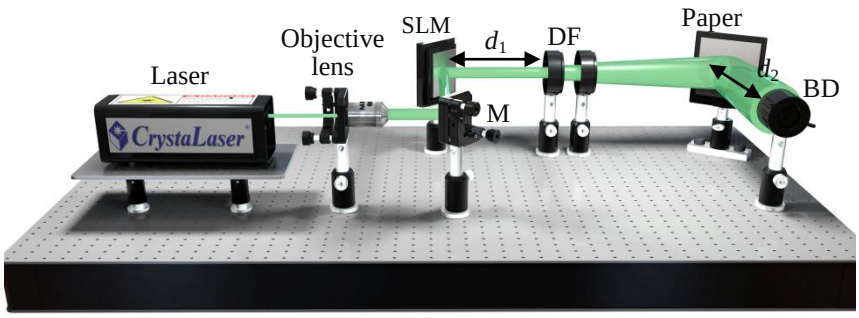

Figure 2.5 A schematic experimental setup for the proposed free-space optical ghost diffraction and information transmission through scattering media: M, Mirror; SLM, Amplitude-only spatial light modulator; DF, Diffusers; BD, Single-pixel bucket detector. d_1 denotes axial distance between the SLM and the first diffuser, and d_2 denotes axial distance between the A4 paper and single-pixel bucket detector. Two cascaded diffusers and a reflective A4 paper are used as a typical example in this study.

An experimental setup in Fig. 2.5 is conducted to show feasibility and effectiveness of the proposed method. A diode pumped green laser (CrystaLaser, CL532-025-S) with

power of 25.0 mW and wavelength of 532.0 nm is expanded with an objective lens (MLWD-50X). The collimated light source illuminates amplitude-only SLM (Holoeye, LC-R720) with pixel size of 20.0 μm. The generated 2D arrays of random numbers with size of 512×512 pixels are sequentially embedded into the SLM, and then are illuminated to propagate through scattering media in free space. The switching rate of SLM is 1.25Hz, which means the interval between pattern switching is 0.8s. Here, two cascaded diffusers (Thorlabs, DG10-1500) and one reflective ordinary A4 paper are used as a typical example. After wave propagation, light intensity at the receiving end is collected by using a single-pixel bucket detector (Newport, 918D-UV-OD3R).

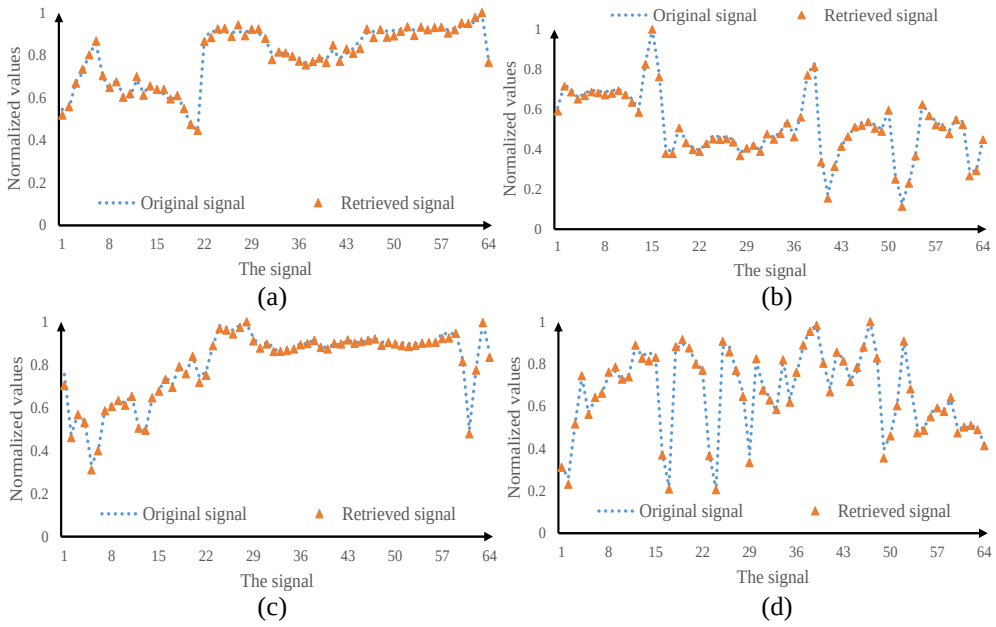

Figure 2.6 The signals retrieved at the receiving end in different environments: the signal obtained (a) when no scattering medium is in wave propagation path in Fig. 2.5, (b) when only the reflective A4 paper is placed in wave propagation path in Fig. 2.5, (c) when one diffuser and the reflective paper are placed in wave propagation path in Fig. 2.5, and (d) when two cascaded diffusers and the reflective paper are placed in wave propagation path in Fig. 2.5. PSNR values of the retrieved signals in (a)-(d) are 35.62 dB, 38.20 dB, 38.02 dB and 36.35 dB, respectively. MSE values of the retrieved signals in (a)-(d) are 2.74×10^{-4}, 1.52×10^{-4}, 1.58×10^{-4} and 2.31×10^{-4}, respectively.

Axial distance between the two diffusers is 25.0 mm. Axial distance between the SLM and the first diffuser is denoted as d_1 with a default value of 12.5 cm. Axial

distance between the second diffuser and the A4 paper is 11.0 cm, and axial distance between the A4 paper and single-pixel bucket detector is denoted as d_2 with a default value of 2.5 cm.

When the series of generated 2D arrays of random numbers is sequentially embedded into the SLM and the modulated wave propagates through scattering media in free space, a series of intensity values are sequentially collected by using the single-pixel bucket detector at the receiving end. Here, four different 1D analog signals are used as the ghosts to be individually encoded and optically transmitted through scattering media in free space to verify the proposed method. The optical experimental results are shown in Figs. 2.6(a)–2.6(d), where the dotted points represent original signals and triangle points represent the retrieved signals. As can be seen in Figs. 2.6(a)–2.6(d), the encoded ghosts are retrieved at the receiving end with high fidelity in different transmission environments. Peak signal-to-noise ratio (PSNR) and mean squared error (MSE) [133,134] are calculated to quantitatively evaluate experimental results, given in Fig. 2.6. The values of MSE and PSNR are respectively calculated by [133]

$$\mathrm{MSE}=\frac{1}{\mathrm{N}}\sum_{i=1}^{\mathrm{N}}\left(S_i-\widehat{S}_i\right)^2, \tag{2.13}$$

$$\mathrm{PSNR}=10\log_{10}\frac{MAX_S^{\,2}}{\mathrm{MSE}}, \tag{2.14}$$

where MAX_S denotes the maximum value of analog signal.

The high PSNR values and low MSE values demonstrate that high-fidelity ghost diffraction and optical information transmission through scattering media in free space are experimentally realized by using the proposed method. To further show the difference between the retrieved signals and original signals in Figs. 2.6(a)–2.6(d), a

box chart is shown in Fig. 2.7. As shown in Fig. 2.7, all the normalized errors between the retrieved signals and original signals are within a very small range, meaning that original signals are retrieved with high fidelity.

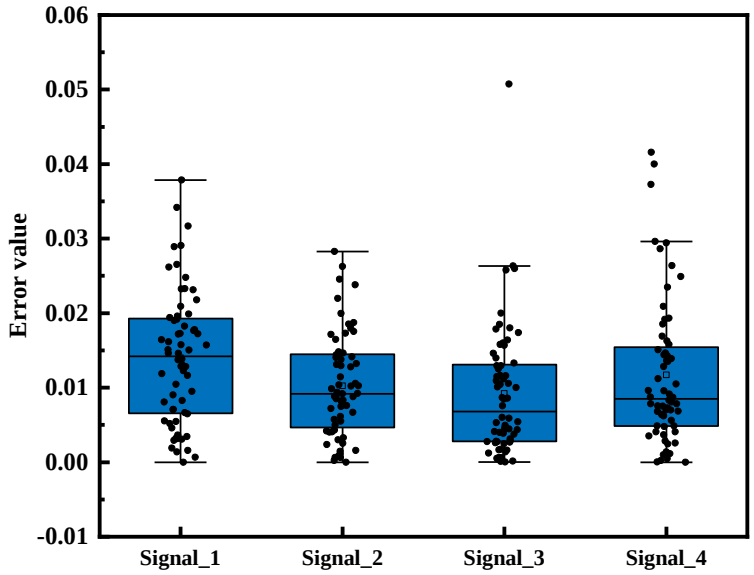

Figure 2.7 Error distributions obtained between original signals and the retrieved signals in Figs. 2.6(a)–2.6(d).

2D grayscale images are also used as ghosts to be encoded into a series of 2D arrays of random numbers, and optical information transmission through scattering media in free space are conducted using the experimental setup in Fig. 2.5. Here, two grayscale images with 64×64 pixels are selected as original signals (i.e., ghosts). Each grayscale image contains 4096 pixels to be sequentially encoded into 2D arrays of random numbers by using the proposed method, and then these generated 2D arrays of random numbers are sequentially embedded into SLM and are illuminated to propagate through scattering media in free space. Here, two typical 2D patterns with random numbers are shown in Figs. 2.8(a) and 2.8(b). As described in Section 2.3, each generated 2D array of random numbers is further transformed into two 2D arrays of random numbers (i.e., $B+\tilde{P}_i$ and $B-\tilde{P}_i$) with a real and positive constant B to remove negative values. Fig. 2.8(a) shows a typical image of $B+\tilde{P}_i$, and Fig. 2.8 (b)

shows a typical image of $B-\tilde{P}_i$. In this experiment, a refreshing rate of the SLM is set as 1.25 Hz as a typical example to illustrate the proposed method, and there are totally 8192 patterns sequentially embedded into the SLM for each 2D grayscale image with 64×64 pixels. The time to acquire 2D information by using single-pixel bucket detector is 6553.6 s. A proof-of-principle optical experiment is conducted in this study, and the refreshing rate can be further increased by using digital micromirror devices (DMD).

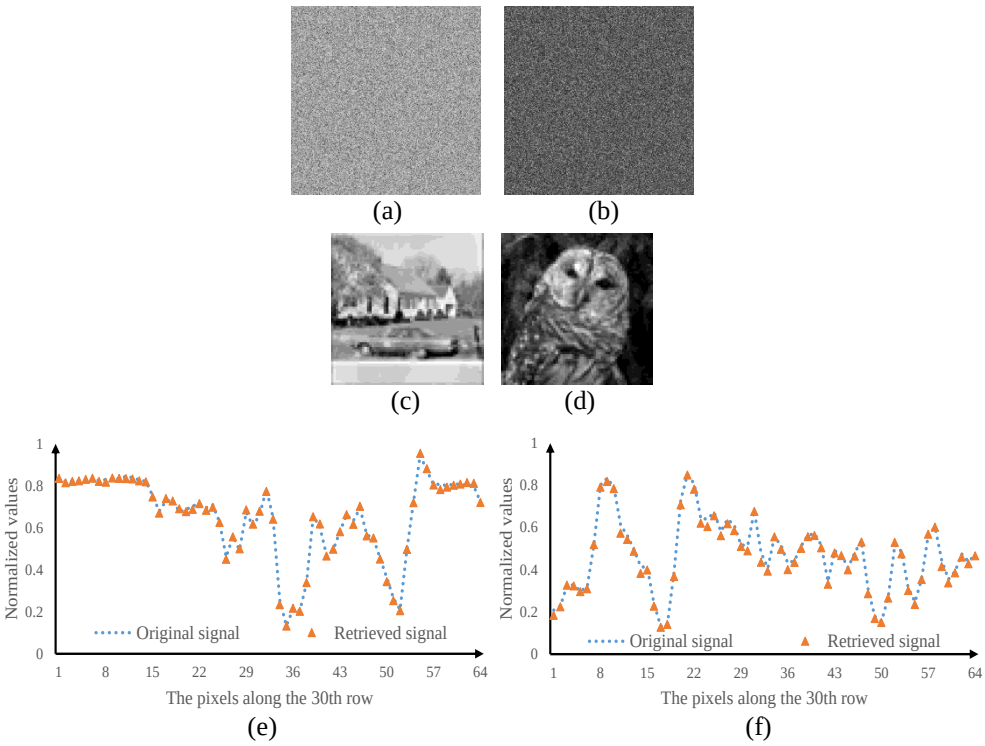

Figure 2.8 Experimental results retrieved at the receiving end: (a) and (b) typically generated 2D patterns with random numbers containing ghost information, (c) and (d) the retrieved ghosts (64×64 pixels) using the proposed method, (e) a typical comparison between the 30th row of the retrieved ghost in (c) and those original values, and (f) a typical comparison between the 30th row of the retrieved ghost in (d) and those original values. PSNR values of (c) and (d) are 37.94 dB and 37.26 dB, respectively. MSE values of (c) and (d) are 1.61×10^{-4} and 1.88×10^{-4}, respectively.

A series of intensity values are correspondingly collected by the single-pixel bucket detector, and these intensity values are further used to retrieve image data. Optical experimental results are shown in Figs. 2.8(c) and 2.8(d) and the PSNR and MSE values are given in Fig. 2.8, which demonstrates that high-fidelity optical

transmission of 2D images can also be realized by using the proposed method when there is a scattering medium in the optical path.

To further illustrate quality of the images (ghosts) retrieved at the receiving end, cross-sectional comparisons between original signals and the retrieved ghosts are conducted and shown in Figs. 2.8(e) and 2.8(f). A typical comparison between the pixels along the 30th row of the retrieved ghost in Fig. 2.8(c) and those original values is shown in Fig. 2.8(e). A typical comparison between the pixels along 30th row of the retrieved ghost in Fig. 2.8(d) and those original values is shown in Fig. 2.8(f). It is demonstrated again that high-fidelity signals are retrieved at the receiving end. As discussed in Section 2.3, scaling factor can be calculated to denote the relationship between intensity values collected by a single-pixel bucket detector and original information. 4096 scaling factors can be calculated for each grayscale image in optical experiment. The scaling factors in Figs. 2.8(c) and 2.8(d) are within a small range, i.e., 2.06×10^{-11}~2.24×10^{-11} and 2.00×10^{-11}~2.25×10^{-11}, respectively. This verifies the validity of the proposed method. It is experimentally demonstrated that high-fidelity 2D image (as ghost) transmission through scattering media in free space can be realized by encoding pixel values into a series of 2D arrays of random numbers.

To better evaluate performance of the proposed method with different parameters, two important parameters, i.e., the magnification factor and size of 2D arrays, are further analyzed for a comparison using the experimental setup in Fig. 2.5.

Different magnification factors are selected to generate 2D arrays of random numbers as information carriers, and these 2D arrays of random numbers are further used for free-space ghost transmission through scattering media. In this case, size of the generated 2D arrays of random numbers is fixed as 512×512 pixels. The experimental results using different magnification factors ranging from 1.0×10^{4} to

2.0×10^5 are shown in Fig. 2.9(a). As can be seen in Fig. 2.9(a), high PSNR values and low MSE values are always obtained when the magnification factor is larger than 3.5×10^4. It is also experimentally found that when the magnification factor is low, influence of environmental and detection noise is large. Experimental results using different sizes (N×N pixels) of the generated 2D arrays of random numbers are shown in Fig. 2.9(b). The experimental setup in Fig. 2.5 is applied. In this case, the magnification factor is fixed as 35000. It is demonstrated in Fig. 2.9(b) that high PSNR values and low MSE values are always obtained when N is larger than 200. In this study, the laser with a fixed power is used in the experiments, and insufficient

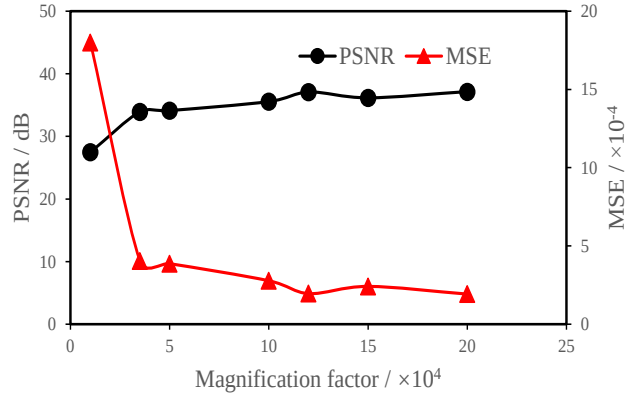

(a)

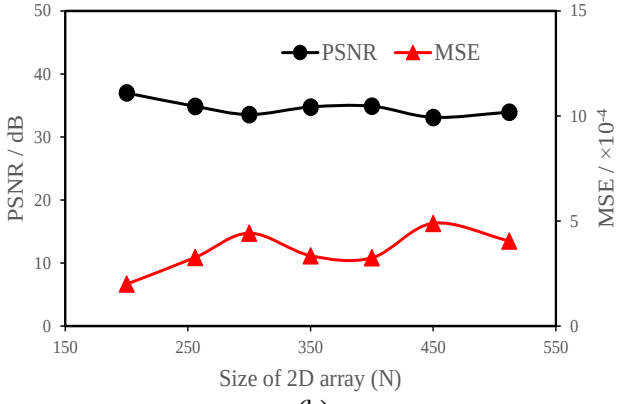

(b)

Figure 2.9 (a) PSNR and MSE values of the signals retrieved at the receiving end when different magnification factors are used in the proposed method, and (b) PSNR and MSE values of the signals retrieved at the receiving end when 2D arrays with different sizes are used.

light reflected by the SLM would be collected by the single-pixel bucket detector when the size of 2D arrays is small (e.g., 64×64 or 128×128 pixels). In conclusion,

the acceptable values of magnification factor in this experimental should be larger than 3.5×10^4. In terms of the acceptable range of size (N×N pixels) of 2D arrays of random numbers, N should be larger than 200.

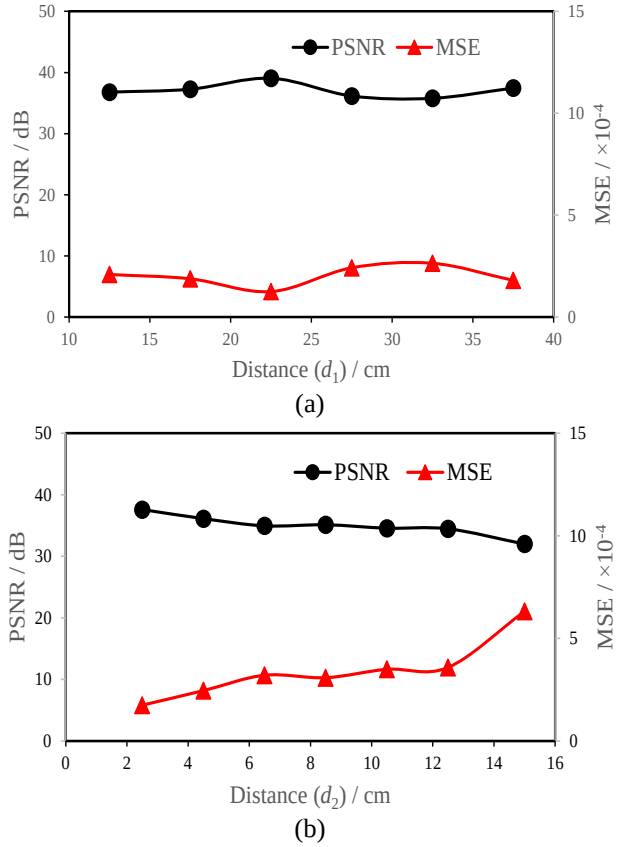

Figure 2.10 (a) PSNR and MSE values of the signals retrieved at the receiving end using different propagation distances d_1, and (b) PSNR and MSE values of the signals retrieved at the receiving end using different propagation distances d_2.

Different propagation distances are further employed to evaluate the proposed method, and experimental results are shown in Figs. 2.10(a) and 2.10(b). Here, d_1 denotes axial distance between the SLM and the first diffuser, and d_2 denotes axial distance between the A4 paper and single-pixel bucket detector in Fig. 2.5. In Fig. 2.10(a), the distance d_2 is fixed as 2.5 cm, and the propagation distance d_1 ranges from 12.5 cm to 37.5 cm. It is shown in Fig. 2.10(a) that high PSNR values and low MSE values are always obtained, and high-fidelity data transmission through scattering media in free space is realized. In Fig. 2.10(b), the distance d_1 is fixed as 12.5 cm, and

the propagation distance d_2 ranges from 2.5 cm to 15.0 cm. It is also illustrated in Fig. 2.10(b) that high PSNR values and low MSE values are always obtained, and high-fidelity data transmission through scattering media in free space is realized. When the propagation distance d_2 is approaching to or larger than 15.0 cm, the scattered light intensity collected by single-pixel bucket detector is weaker and quality of the retrieved ghosts decreases as shown in Fig. 2.10(b). In terms of d_1, all the distances (i.e., from 12.5 cm to 37.5 cm) in this experiment are acceptable when d_2 is fixed as 2.5 cm. In terms of d_2, distances smaller than 12.0 cm are all acceptable in this experiment when d_1 is fixed as 12.5 cm.

The laser with different wavelengths is also used to conduct the proposed free-space ghost diffraction and optical information transmission through scattering media. Here, the laser with five different wavelengths (i.e., 405.0nm, 520.0nm, 532.0nm, 658.0nm and 690.0nm) is individually used in the experiments. Experimental results of optical diffraction through scattering media using the generated 2D arrays of random numbers are shown in Fig. 2.11. It can be seen in Fig. 2.11 that PSNR and MSE values of the retrieved data remain stable, and high-fidelity free-space optical ghost diffraction and information transmission through scattering media are always realized when different wavelengths are used. Therefore, multiple transmission channels are potentially feasible.

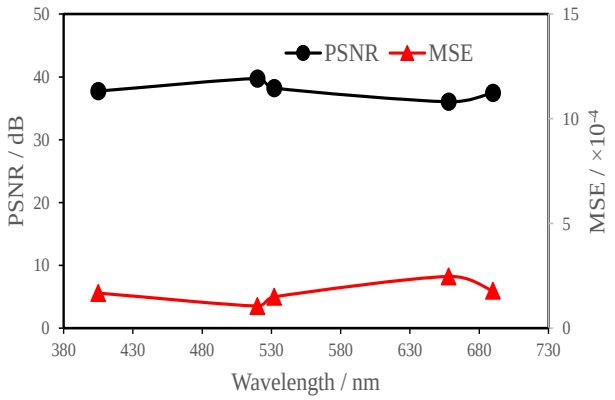

Figure 2.11 PSNR and MSE values of signals retrieved at the receiving end when the laser with different wavelengths is used.

In this study, two cascaded diffusers and one A4 paper are utilized as scattering media and reflective media, which provide typically optical experimental results in scattering environment. It is believed that the proposed method can also work well through other scattering media, and performance of the proposed method in different scattering environments would be further evaluated. Compared with wavefront shaping [3], the proposed method does not require a time-consuming optical alignment and calibration process. Compared with other optical methods that use linear intensity modulation [4] to realize information transmission, the proposed method can realize high-fidelity free-space analog signal transmission and retrieval through scattering media.

2.5 Summary

A new method to directly generate a series of 2D arrays of random numbers to encode the ghost (e.g., signals or images) is proposed to realize high-fidelity free-space optical information transmission through scattering media. Optical experimental results demonstrate that high-fidelity free-space optical information transmission through scattering media is realized. The proposed ghost diffraction could open up an

avenue for many applications, e.g., high-fidelity free-space optical information transmission through scattering media.

Chapter 3 High-fidelity temporally-corrected transmission through dynamic smoke

3.1 Introduction

With ever-growing popularity of wireless communication, radio-frequency (RF) technologies and systems are widely deployed and utilized in our community [135,136]. The RF band of electromagnetic spectrum is expensive and fundamentally limited in capacity, since most sub-bands are exclusively licensed [1]. It is desirable and crucial to consider other options for wireless communication that rely on other electromagnetic spectra. Compared with traditional RF technologies, free-space optical communication has attracted much increasing attention in recent years due to its free and abundant spectrum resources, low power consumption and low cost [1,137]. Free-space optical data transmission often encounters absorption and scattering phenomena due to atmospheric conditions. In fact, optical transmission or imaging [48,138,139] through scattering media, e.g., smoke, rain, fog and dust, is always regarded as a significant challenge due to the severely degrading of optical field information. To verify the free-space optical data transmission, much research work has been conducted using different light sources in various optical transmission environments, e.g., atmospheric conditions [49–52] and underwater [53,54].

In atmospheric environments, smoke or fog severely attenuates the propagating light and degrades signal-to-noise ratio (SNR) of transmitted signals. When the light beam propagates through smoke or fog, light intensities [55–62], optical polarization states [63–68] and optical field information [69,70] could be changed. In particular, atmospheric environments, e.g., smoke, always have a dynamic property as a result of the changeable meteorological conditions. Due to the settlement and liquefaction of

smoke, the properties of optical field information could be dynamically changed during optical data transmission. Therefore, temporal changes of dynamic smoke affect the transmission and detection of optical information, and optical data information collected at the receiving end always contains transmission errors. Performance of free-space optical communication can be severely impaired by the absorption, scattering, and dynamic change of smoke properties. However, optical experiments [140–142] are mainly aimed to study the effect of different channel properties (e.g., different temperature [142]) of smoke environment on the transmission rate. Many methods [143–146] have also been developed to mitigate the transmission error caused by atmospheric turbulence. For instance, decision feedback equalizer [144] optimized by minimum mean square error was investigated to improve the performance of optical communication system through various atmospheric conditions. However, few studies have been conducted on optical data transmission through dynamic smoke. In fact, free-space optical analog-signal transmission in a dynamic smoke environment is challenging, and it is highly desirable to investigate the influence of dynamic smoke environment on free-space optical analog-data transmission.

In this Chapter, high-fidelity free-space optical data transmission through dynamic smoke is studied by using a pixel-to-plane encoding algorithm to generate a series of 2D arrays with random numbers as information carriers. A novel pixel-to-plane encoding algorithm is first developed to generate 2D arrays of random numbers constrained by each pixel of the signal to be transmitted. To eliminate transmission errors caused by dynamic smoke, a fixed reference pattern is further introduced and used to conduct dynamic compensation, and transmission errors and noise induced by dynamic smoke are temporally corrected. Experimental results are obtained to verify

the proposed method, when the developed free-space optical data transmission scheme is applied in dynamic smoke environment with different concentrations. It is demonstrated that irregular analog signals can always be retrieved with high fidelity at the receiving end after transmitting through dynamic smoke. Moreover, the proposed method also shows high robustness against dynamic smoke with different concentrations. The proposed method could open up a new research perspective for free-space optical data transmission through dynamic smoke. The corresponding publication of this Chapter is listed as follows:

Yonggui Cao, Yin Xiao, Zilan Pan, Lina Zhou, and Wen Chen, "High-fidelity temporally-corrected transmission through dynamic smoke via pixel-to-plane data encoding," Optics Express, **30**(20), 36464–36477 (2022).

3.2 Principles

A series of 2D arrays of random numbers are first generated as information carriers in the proposed method to realize high-fidelity free-space optical data transmission through dynamic smoke. In the proposed method, a sequence of pixels of the signal (S_i, i=1,2,3,…,N) to be transmitted are encoded into a series of 2D arrays of random numbers $\left(\hat{\mathrm{P}}_i, i=1,2,3,\ldots,N\right)$. To clearly illustrate the generation process, a simplified flow chart of the proposed optical encoding process is shown in Fig. 3.1. The detailed optical encoding procedure has already been introduced in Section 2.3 in this thesis.

The magnification factor M plays an important role in the proposed pixel-to-plane encoding algorithm, and it needs to satisfy that the enlarged value is comparable to the total number of pixels in the generated 2D array of random numbers. The size of 2D arrays of random numbers is 512×512 pixels in this study, and a typical magnification factor M of 1.0×10^5 can be used.

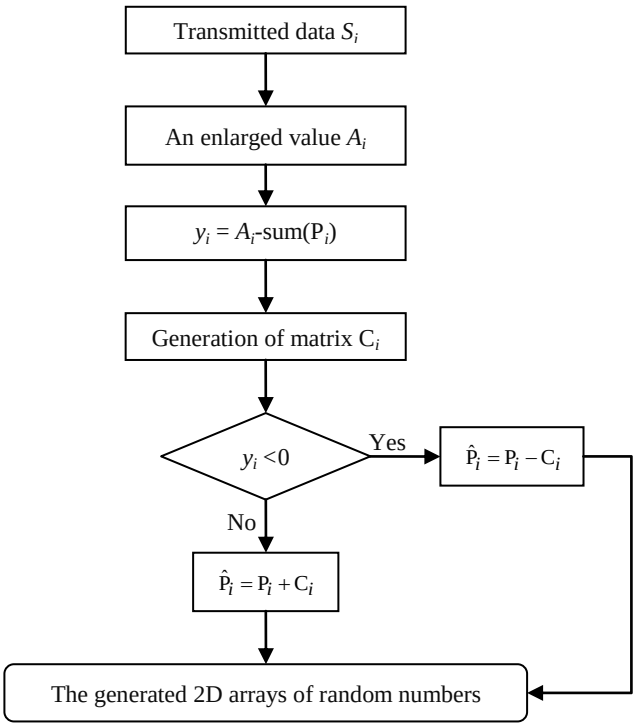

Figure 3.1 A flow chart to illustrate the generation of 2D arrays of random numbers to encode the signal.

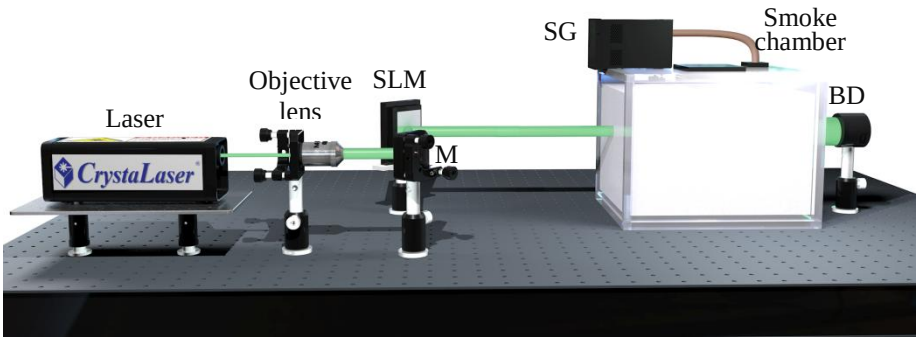

Figure 3.2 A schematic experimental setup for the proposed free-space optical data transmission in a dynamic smoke environment: M, Mirror; SLM, Amplitude-only spatial light modulator; BD, Single-pixel bucket detector; SG, Smoke generator.

The 2D arrays of random numbers $\hat{\mathbf{P}}_i$ could be embedded into amplitude-only spatial light modulator in Fig. 3.2. According to wave propagation theory [46,132], light intensities collected by single-pixel bucket detector at the receiving end can be described by

$$
\begin{aligned}
b_i &= u\iint \hat{\mathbf{P}}_i(x,y)\, e^{-2\pi j(x\xi+y\eta)}\, dxdy\Big|_{\xi=0,\eta=0} \\
&= u\iint \hat{\mathbf{P}}_i(x,y)\, dxdy
\end{aligned}
\tag{3.1}
$$

where (x,y) and (ξ,η) denote the coordinates, u denotes a scaling factor, and b_i denotes the recorded ith intensity value.

In Fig. 3.2, smoke is generated and pumped into a chamber to be considered as a dynamic smoke channel in free space, and liquefaction and sedimentation of smoke particles dynamically change scattering properties in the chamber. In the process of light intensity measurement, environmental and shot noise affects quality of the retrieved signals at the receiving end. To suppress noise, a differential operation is proposed and applied in this study. When all the pixel values of original signal to be transmitted are individually encoded into 2D arrays of random numbers, each generated 2D array of random numbers ($\hat{\mathrm{P}}_i, i=1,2,3,\ldots,N$) is further converted into two separate 2D arrays, i.e., $\mathrm{B}+\hat{\mathrm{P}}_i$ and $\mathrm{B}-\hat{\mathrm{P}}_i$ where $\mathbf{B}$ denotes a real and non-negative value.

Since dynamic smoke environment in Fig. 3.2 results in a loss or distortion of optical field information, a fixed reference pattern **R**, i.e., a pre-generated random amplitude-only pattern, is used before each generated 2D array of random numbers (i.e., $\mathrm{B}+\hat{\mathrm{P}}_i$ and $\mathrm{B}-\hat{\mathrm{P}}_i$). Therefore, four 2D arrays of random numbers corresponding to each pixel of the transmitted signal need to be sequentially embedded into amplitude-only SLM in Fig.3.2. The fixed reference pattern [147,148] plays an important role in the proposed high-fidelity free-space optical data transmission scheme. Scaling factors physically existing in the free-space optical transmission channel dynamically change due to dynamic smoke, and the fixed reference pattern is introduced here and used to overcome this challenge. For instance, the reference pattern **R** is embedded into SLM at time slot t_i, and an intensity value b_{ir} is collected by using single-pixel

bucket detector at the receiving end. Then, 2D array of random numbers ($\mathrm{B}+\hat{\mathrm{P}}_i$) is embedded into SLM at time slot t_{i+1}, and an intensity value b_{i1} is recorded. Subsequently, the fixed reference pattern $\mathbf{R}$ is embedded into SLM again at time slot t_{i+2}, and an intensity value $\tilde{b}_{ir}$ is recorded. Finally, the 2D array of random numbers ($\mathbf{B}-\hat{\mathbf{P}}_i$) is embedded into SLM at time slot t_{i+3}, and an intensity value b_{i2} is collected. For each pixel of the signal to be transmitted, the four recordings by using the single-pixel bucket detector can be respectively described by

$$b_{ir} = u\left(t_i\right)\iint \mathrm{R}\left(x,y\right)dxdy, \tag{3.2}$$

$$b_{i1} = u\left(t_{i+1}\right)\iint\left[\mathrm{B}+\hat{\mathrm{P}}_i\left(x,y\right)\right]dxdy, \tag{3.3}$$

$$\tilde{b}_{ir} = u\left(t_{i+2}\right)\iint \mathrm{R}\left(x,y\right)dxdy, \tag{3.4}$$

$$b_{i2} = u\left(t_{i+3}\right)\iint\left[\mathrm{B}-\hat{\mathrm{P}}_i\left(x,y\right)\right]dxdy, \tag{3.5}$$

where $u(t)$ denotes scaling factor at time slot t.

Since the time interval is short to display the patterns in amplitude-only SLM in each group of four measurements for optically transmitting each pixel of the signal, it can be obtained that

$$u\left(t_i\right) \approx u\left(t_{i+1}\right), \tag{3.6}$$

$$u\left(t_{i+2}\right) \approx u\left(t_{i+3}\right). \tag{3.7}$$

Therefore, a signal $\tilde{S}_i$ can be retrieved at the receiving end described by

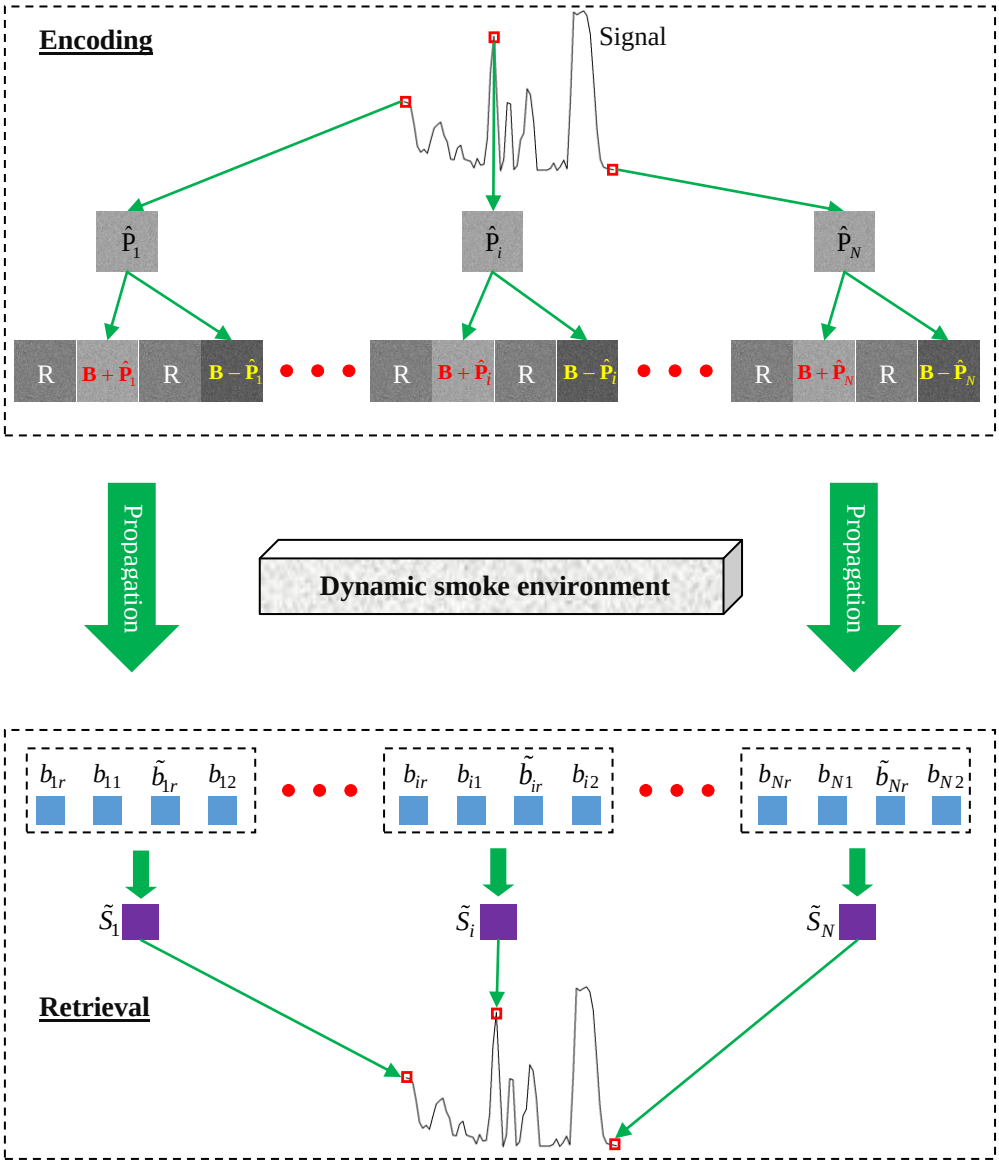

Figure 3.3 A flow chart of the proposed high-fidelity free-space optical data transmission through dynamic smoke.

$$\begin{aligned}\tilde{S}_i &= \frac{u(t_{i+1})\iint[\mathrm{B}+\hat{\mathrm{P}}_i(x,y)]dxdy}{u(t_i)\iint \mathrm{R}(x,y)\,dxdy} - \frac{u(t_{i+3})\iint[\mathrm{B}-\hat{\mathrm{P}}_i(x,y)]dxdy}{u(t_{i+2})\iint \mathrm{R}(x,y)\,dxdy} \\ &= \frac{1}{\iint \mathrm{R}(x,y)\,dxdy}\left\{\iint[\mathrm{B}+\hat{\mathrm{P}}_i(x,y)]dxdy - \iint[\mathrm{B}-\hat{\mathrm{P}}_i(x,y)]dxdy\right\} \\ &= Z\iint \hat{\mathrm{P}}_i(x,y)\,dxdy\end{aligned} \tag{3.8}$$

where Z denotes scaling factor between the retrieved signal and original signal, which is described by

$$Z = \frac{2}{\iint \mathrm{R}(x, y)\, dxdy}. \tag{3.9}$$

Therefore, based on Eq. (3.8), the proposed method is able to realize high-fidelity free-space optical data transmission through dynamic smoke. To clearly illustrate the proposed method, a flow chart is further shown in Fig. 3.3.

3.3 Experimental results and discussion

3.3.1 Experimental setup

To verify feasibility and effectiveness of the proposed method, a series of optical experiments are conducted, and a schematic experimental setup is shown in Fig. 3.2. An objective lens is used to expand a diode-pumped green laser (CrystaLaser, CL532-025-S) with a power of 25.0 mW and wavelength of 532.0 nm. The series of generated 2D arrays of random numbers and the fixed reference pattern are alternately embedded into an amplitude-only SLM (Holoeye, LC-R720) with pixel size of 20.0 μm to be illuminated by the collimated light. The switching rate of SLM is 1.25Hz. In optical experiments, refreshing rate of the SLM is set as 1.25 Hz as a typical example to illustrate the proposed method. Then, dynamic smoke is generated and pumped into an acrylic chamber placed in the beam path. The artificially-generated smoke is produced by using a commercial smoke generator (HALFSun, power of 3000W and pumping rate of 973.0 cm^3/s) and smoke oil. The smoke oil is a mixture of glycerol and water. Therefore, dynamic smoke environments are established. Light intensities after propagating through dynamic smoke are recorded by using a single-pixel bucket detector (Newport, 918D-UV-OD3R) without a front lens. Different from other free-space optical data transmission systems, a single-pixel bucket detector is used in the proposed method to collect light intensities at the receiving end. Finally, the recorded

experimental data is demodulated to retrieve the transmitted signal using the proposed method.

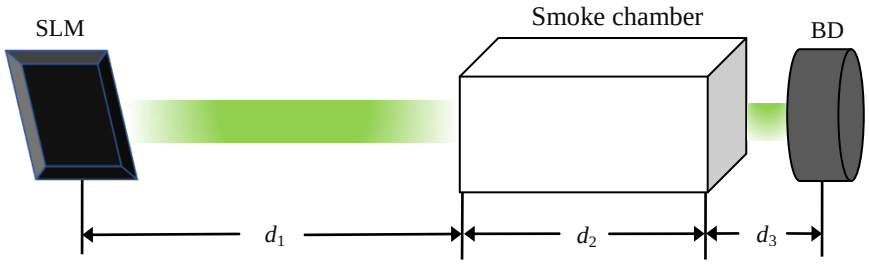

Figure 3.4 A schematic of axial transmission distances in the designed free-space optical data transmission system: d_1, axial distance between SLM and front side of smoke chamber; d_2, length of smoke chamber; d_3, axial distance between back side of smoke chamber and single-pixel bucket detector.

Table 3.1 The parameters used in optical experiments.

Chambers with different volumes (cm^3)	Pumping time (s)	d_1 (cm)	d_3 (cm)	Total distance (cm)
20×30×40	7.5	82.5	2.5	105.0
30×30×40	11.25	72.5	2.5	105.0
40×30×40	15.0	62.5	2.5	105.0
60×30×40	22.5	42.5	2.5	105.0
80×30×40	30.0	22.5	2.5	105.0
100×30×40	37.5	2.5	2.5	105.0

To illustrate optical data transmission in optical experiments, axial distances are shown in Fig. 3.4. The axial distance between amplitude-only SLM and front side of smoke chamber is denoted as d_1, and the length of smoke chamber is denoted as d_2. The axial distance between back side of smoke chamber and single-pixel bucket detector is denoted as d_3. In optical experiments, the total axial transmission distance, i.e., $d_1+d_2+d_3$, is fixed at 105.0 cm. Other experimental parameters are given in Table 3.1. Acrylic chambers with different volumes (i.e., 20(L)×30(W)×40(H), 30×30×40, 40×30×40, 60×30×40, 80×30×40, and 100×30×40 cm^3) are designed to conduct optical experiments for a comparison. Six lengths of d_2 in Fig. 3.4 are respectively used, i.e., 20.0, 30.0, 40.0, 60.0, 80.0 and 100.0 cm. In the smoke chambers, width and height of smoke chambers are fixed at 30.0 cm and 40.0 cm, respectively. The

axial distance d_3 between back side of smoke chamber and single-pixel bucket detector is fixed at 2.5 cm. To generate smoke with the same concentration in the chamber with different volumes for a comparison, a fixed ratio of 0.3041 between the total smoke volume pumped into acrylic chamber and the total volume of acrylic chamber is employed. Dynamic smoke is produced into the acrylic chamber during free-space optical data transmission from top side of the chamber, as shown in Fig. 3.2. Due to the existence of liquefaction and sedimentation of the smoke, smoke environment dynamically changes during optical experiments, and is used as a dynamic scattering medium to verify the proposed method.

3.3.2 Attenuation due to dynamic smoke

To study the impact of different smoke concentrations, a relationship between the collected light intensities and the concentrations of glycerol smoke can be obtained in real time by using optical thickness (OT). In this study, real-time OT in free-space optical transmission channel is calculated to describe concentration variations in the transmission channel based on Beer-Lambert law [149] defined by

$$I = I_0 e^{-\mathrm{OT}}, \tag{3.10}$$

where I_0 denotes the recorded light power at the receiving end without smoke chamber in the free-space optical transmission system, and I denotes the recorded light power at the receiving end with smoke chamber placed in free-space optical transmission. Therefore, the OT can be calculated by

$$\mathrm{OT} = -\ln\frac{I}{I_0}. \tag{3.11}$$

To eliminate measurement errors caused by the fluctuation of propagating wave, light intensities recorded at different time slots without the smoke chamber in the

free-space optical transmission are used to calculate an average light power I_0 described by

$$I_0 = \frac{1}{V}\sum_{i=1}^{V} I_{0i}, \tag{3.12}$$

where V denotes the total measurement number, and I_{0i} denotes the light intensities recorded at the receiving end.

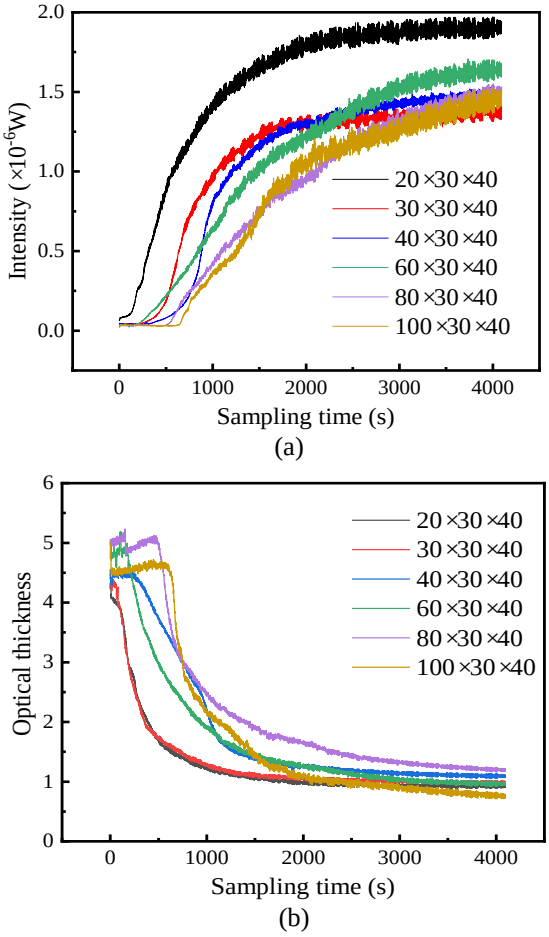

Figure 3.5 (a) The light intensities recorded at the receiving end with the sampling time when the smoke chambers with different volumes (20×30×40, 30×30×40, 40×30×40, 60×30×40, 80×30×40, and 100×30×40 cm^3) are respectively used, and (b) a relationship between the sampling time and real-time OT values when the smoke chambers with different volumes (20×30×40, 30×30×40, 40×30×40, 60×30×40, 80×30×40, and 100×30×40 cm^3) are respectively used.

The light intensities recorded at different time slots are obtained and shown in Fig. 3.5(a), when smoke chambers with different volumes (20×30×40, 30×30×40, 40×30×40, 60×30×40, 80×30×40, and 100×30×40 cm3) are respectively used. The

collected light intensities are small at the beginning, and increase with the sampling time and finally remain stable. Dynamic smoke pumped into the chamber has a high density at the beginning, and the propagating wave is strongly scattered through smoke chamber which results in only few light to be collected by the single-pixel bucket detector. It is also demonstrated in Fig. 3.5(a) that the light intensities recorded at the beginning are always at a low level, when the different smoke chambers are used. Due to precipitation and liquefaction process of the smoke, smoke concentration in the chambers decreases. In addition, the length of smoke chamber could affect the collected light intensities. The longer length of smoke chamber makes the collected light intensities smaller. Real-time OT values are further calculated based on Eq. (3.11) to describe the impact of dynamic smoke, and experimental results are shown in Fig. 3.5(b). As can be seen in Fig. 3.5(b), the trends are similar, when smoke chambers with different volumes are respectively used. The OT values are at a high level at the beginning, since smoke concentration in the chamber is at the largest level. As the sampling time increases, OT values decrease due to the existence of liquefaction and sedimentation of the smoke in the chamber.

3.3.3 Optical analog-data transmission

Due to dynamic smoke in the chamber, real-time OT values during optical transmission of different pixels of a signal are different. To better describe the OT in free-space optical data transmission through dynamic smoke, average optical thickness (AOT) is further calculated to measure the fluctuation. Each signal contains N pixels, and then in the proposed method the AOT can be calculated by

$$\mathrm{AOT} = \frac{1}{2N}\sum_{i=1}^{2N}\mathrm{OT}_i. \tag{3.13}$$

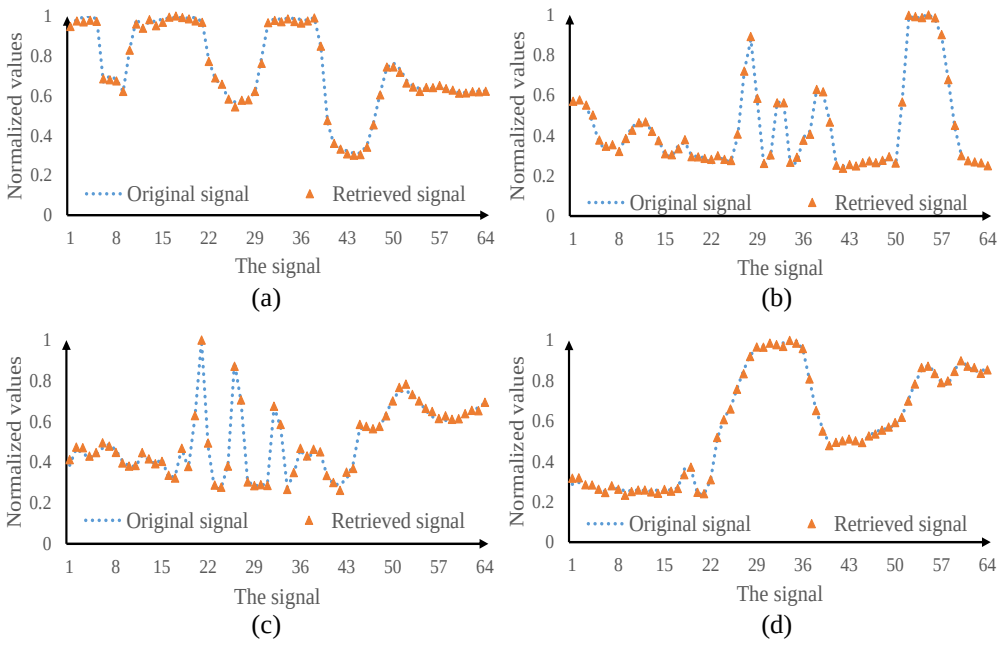

Figure 3.6 (a)-(d) The signals experimentally retrieved at the receiving end with a smoke chamber of 80×30×40 cm^3 and other experimental parameters in Table 3.1: the AOT in (a)-(d) is 1.58, 1.57, 1.63, and 1.59. PSNR values of the retrieved signals in (a)-(d) are 38.55 dB, 38.28 dB, 37.02 dB, and 39.94 dB, respectively. MSE values of the retrieved signals in (a)-(d) are 1.40×10^{-4}, 1.49×10^{-4}, 1.99×10^{-4}, and 1.01×10^{-4}, respectively.

Four irregular analog signals are first encoded by using the proposed pixel-to-plane algorithm to generate a series of 2D arrays of random numbers, and then these 2D arrays of random numbers and the fixed reference pattern are alternately embedded into the amplitude-only SLM to be optically illuminated to propagate through dynamic smoke in Fig. 3.2 to verify the proposed method. Some typically experimental results are shown in Fig. 3.6, where the dot denotes original signal and the triangle denotes a signal retrieved at the receiving end. It is experimentally demonstrated in Figs. 3.6(a)–3.6(d) that the signals can be retrieved with high fidelity in the developed free-space optical data transmission through dynamic smoke by using the proposed method. To evaluate the signals retrieved at the receiving end, MSE and PSNR) are calculated to mathematically show the experimental results. The AOT, MSE and PSNR values are calculated and given in Fig. 3.6, and low MSE values and high PSNR values of the retrieved signals are always obtained by using the

proposed method. It is illustrated in Fig. 3.6 that the proposed method is feasible and effective.

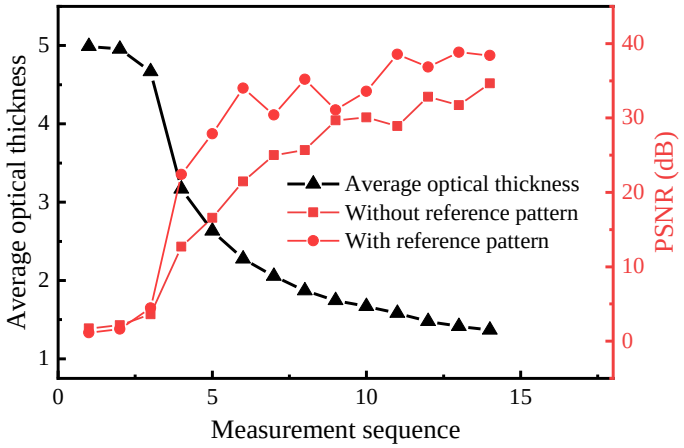

Figure 3.7 A comparison of quality of the signals retrieved at the receiving end with and without the fixed reference pattern and the corresponding AOT values.

Optical experiments are further conducted for a comparison, when the proposed method with and without the fixed reference pattern is applied in the free-space optical data transmission system through dynamic smoke. The experimental results are shown in Fig. 3.7. The measurement sequence in Fig. 3.7 represents free-space optical information transmission of one fixed analog signal at different time slots. As can be seen in Fig. 3.7, when the AOT is at a high level (i.e., larger than 2.5), PSNR values of the retrieved signals with and without the reference pattern are small (i.e., lower than 30.0 dB). The large AOT values mean that smoke in the chamber has high density, and optical field information could be severely scattered. When the AOT decreases, PSNR values of the retrieved signals increase. In addition, PSNR values of the signals retrieved by using the proposed method with the fixed reference pattern are higher than those of the signals retrieved without the reference pattern. The fixed reference pattern is utilized in optical experiments to record real-time scaling factors,

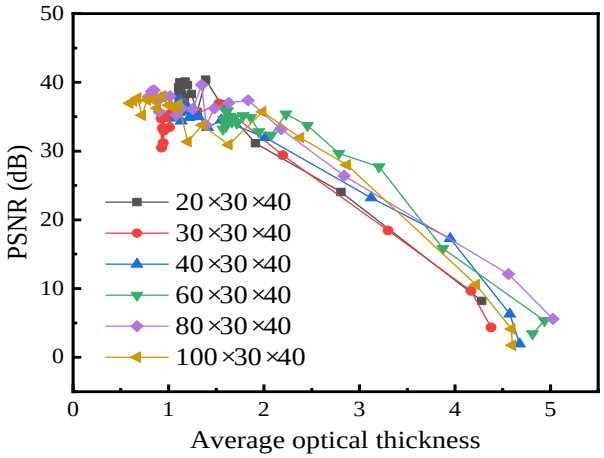

Figure 3.8 A relationship between the AOT and the PSNR of the retrieved signals obtained when the smoke chambers with different volumes are respectively used. One fixed analog signal is repeatedly tested here.

and then measurement errors caused by dynamic smoke can be corrected. The usage of a fixed reference pattern in the proposed method improves quality of the retrieved signals at the receiving end, when dynamic smoke environment is studied. It is also demonstrated that feasibility and effectiveness of the proposed high-fidelity free-space optical data transmission through dynamic smoke are verified.

The AOT is calculated to describe real-time destruction degree of optical field information in free-space optical data transmission through dynamic smoke. A relationship between the AOT and PSNR values of the retrieved signals is further obtained and shown in Fig. 3.8, when the smoke chambers with different volumes ($20\times30\times40$, $30\times30\times40$, $40\times30\times40$, $60\times30\times40$, $80\times30\times40$, and $100\times30\times40$ cm^3) are respectively used. As can be seen in Fig. 3.8, PSNR values of the retrieved signals decrease with the higher AOT. It is a downward trend, when the AOT is higher than 2.5. It is demonstrated in Fig. 3.8 that the retrieved signals are of high quality by using the proposed method when the AOT is lower than 2.5. The typically retrieved signals are shown in Figs. 3.9(a)–3.9(f), and the AOT and PSNR values of the retrieved signals are given in Figs. 3.9(a)–3.9(f). The label of x-axis in Figs. 3.9(a)–3.9(f) means the signal to be transmitted in dynamic smoke environment. Each transmitted

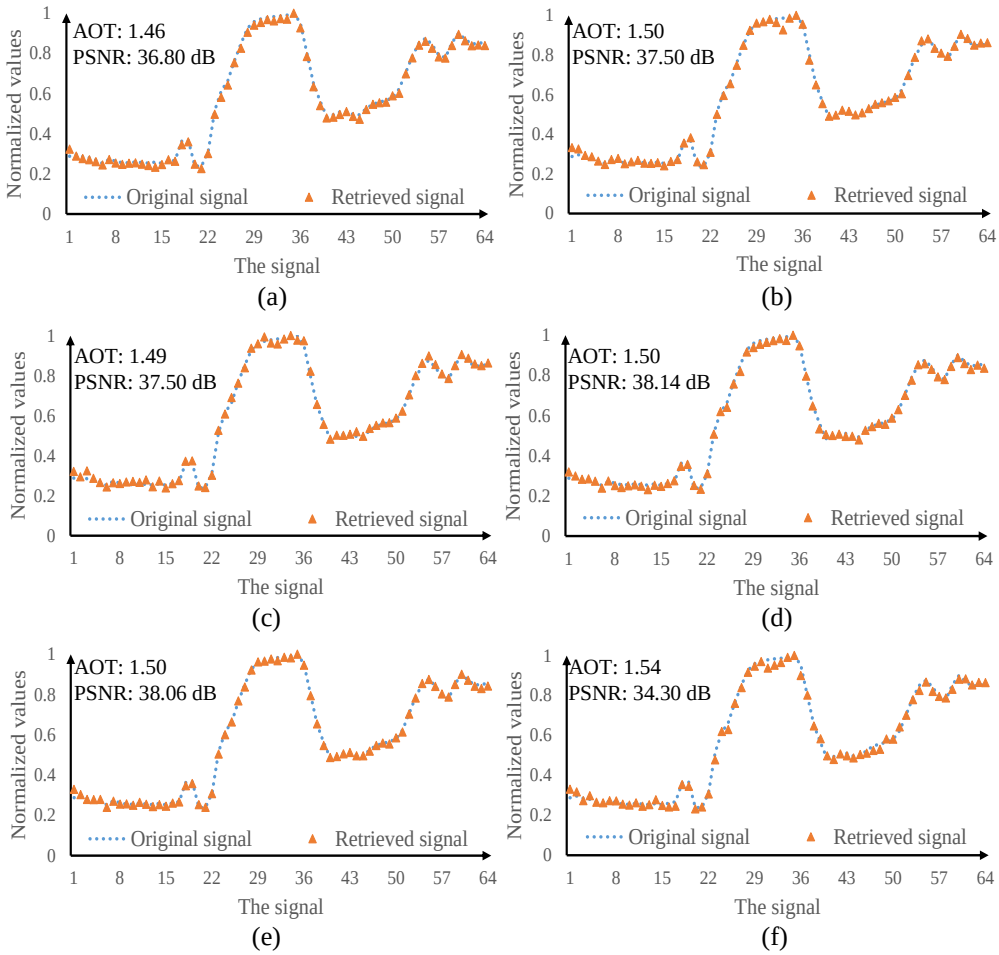

Figure 3.9 (a)-(f) The signals retrieved at the receiving end using the proposed method when smoke chambers with different volumes (length d_2 of 20.0, 30.0, 40.0, 60.0, 80.0, and 100.0 cm) are respectively used.

signal has 64 pixels, which are generated randomly as the tested signal. As can be seen in Figs. 3.9(a)–3.9(f), the retrieved signals are of high fidelity by using the proposed method, when smoke chambers with different volumes are designed and used in the developed free-space optical data transmission through dynamic smoke. Moreover, based on the experimental results of irregular analog signals transmission through dynamic smoke, binary signals can also be retrieved with high fidelity when only binary signals are transmitted based on the developed optical system. Binary signals are much simpler compared with irregular analog signals, and the errors between transmitted binary signals retrieved with the propose method and original binary signals can be zero. Advantages of the proposed method can be summarized as

follows: (1) Pixel-to-plane encoding algorithm are proposed to transform each pixel of signal into a 2D array of random numbers, which can be used as information carrier; (2) Transmission errors aroused by dynamic smoke are temporally corrected with a fixed reference pattern; (3) A novel signal retrieval process is proposed to realize high-fidelity signal transmission through dynamic smoke.

3.4 Summary

A new approach is proposed to realize high-fidelity free-space optical data transmission through dynamic smoke using a series of 2D arrays of random numbers via pixel-to-plane encoding. A series of 2D arrays with random numbers are generated to be used as information carriers in the free-space optical data transmission channel. Transmission errors induced by dynamic smoke are temporally corrected using a fixed reference pattern. It is experimentally demonstrated that irregular analog signals can be retrieved with high fidelity at the receiving end, when the AOT in the free-space optical data transmission channel is lower than 2.5. It is expected that the proposed method could open up a novel research perspective for high-fidelity free-space optical data transmission through dynamic smoke.

Chapter 4 Optical transmission in dynamic and complex scattering environment

4.1 Introduction

It is well recognized that information transmission plays an important role in modern society [136,150]. Radio frequency technology has been widely applied in communication systems. However, it has several drawbacks (e.g., small spectral range and license request), and could not fully meet the demands of data communication [136]. Many data transmission approaches have been further developed to address the challenges [50–52,151]. Among them, free-space optical data transmission has a potential to provide flexible deployments and an extended spectral range, and has attracted much interest [1,137]. However, free-space optical data communication also encounters some significant challenges [49,152]. The atmospheric disturbance, e.g., wind, rain and fog, could severely affect free-space optical data transmission. Optical properties [55–70,140–142], e.g., intensity [55–62] and polarization [63–68], could be dynamically changed, when optical transmission is conducted in a turbulent environment. Signal-to-noise ratio of the signals retrieved at the receiving end is severely degraded due to absorption and scattering, and transmission errors are introduced. Some methods [143–146,153] have been developed to suppress transmission errors induced by atmospheric disturbance. For instance, free-space optical communication could be enhanced using a decision feedback equalizer [144,145] optimized by minimum mean squared error. Until now, few studies have been conducted on optical analog-signal transmission in dynamic and complex scattering environments, and it is desirable to correct the influence induced by dynamic and complex scattering environments. Non-line-of-sight transmission has

also been studied [91,95,154–156], and optical wave could be blocked or dramatically attenuated. Encode a signal into 2D patterns as information carriers [153,157–159] has been studied to realize high-fidelity optical transmission, but reference patterns [153] need to be repeatedly used to correct scaling factors in dynamic and complex scattering environments. In addition, four 2D patterns need to be applied to optically transmit each pixel of an analog signal. Therefore, optical analog-signal transmission in dynamic and complex scattering environment is still challenging, and it is desirable to investigate new schemes for high-fidelity free-space optical analog-data transmission through dynamic and complex scattering media.

A new scheme is proposed to realize high-fidelity free-space optical analog-signal transmission in dynamic and complex scattering environments using binary encoding with a modified differential method. Each pixel of an analog signal to be transmitted is first divided into two values, and each of them is encoded into a random matrix. Then, a modified error diffusion algorithm is utilized to transform the random matrix into a 2D binary array. Each pixel of the analog signal is eventually encoded into only two 2D binary arrays, and transmission errors and dynamic scaling factors induced by dynamic and complex scattering media can be temporally corrected. Dynamic smoke and non-line-of-sight are created as a dynamic and complex scattering environment to verify the proposed method. It is experimentally demonstrated that analog signals retrieved at the receiving end are always of high fidelity using the proposed method, when average path loss (*APL*) is less than 29.0 dB. The proposed method could open up a novel research perspective for high-fidelity free-space optical analog-signal transmission through dynamic and complex scattering media. The corresponding publication of this Chapter is listed as follows:

Yonggui Cao, Yin Xiao, and Wen Chen, "Optical analog-signal transmission system in dynamic and complex scattering environment using binary encoding with a modified differential method," Optics Express, **31**(10), 16882–16896 (2023).

4.2 Principles

4.2.1 Pixel-to-binary array encoding

In the developed optical analog-signal transmission system, a series of 2D binary arrays are generated to serve as information carriers. A flow chart for the generation of 2D binary arrays is shown in Fig. 4.1(a). The proposed binary array generation approach is described as follows:

(1) A pixel is enlarged with a given magnification factor M (e.g., 60000) to be a new value A. The integer part of A is denoted as p, and the decimal part of A is denoted as q.

(2) A sequence T with random values is obtained. The length of sequence T is $2\times p$. The first half of sequence T is generated with random values ranging from 0 to 1, and another half of sequence T is calculated by using the difference between 1 and each corresponding value of the first half part. The sum of T is equal to p.

(3) A 2D array of random numbers C is generated by arbitrarily placing all the values of sequence T and the decimal value q into a pre-generated all-zero matrix.

(4) A modified error diffusion algorithm is developed to transform the generated 2D array C obtained in Step (3) into a binary array.

In Step (4), each generated 2D array C of random numbers is converted into a 2D binary array with a modified error diffusion algorithm, which is described as follows:

(i) For each pixel in the generated 2D array C, a threshold of 0.5 is used to transform it into a binary representation (i.e., 0 or 1), which is described by

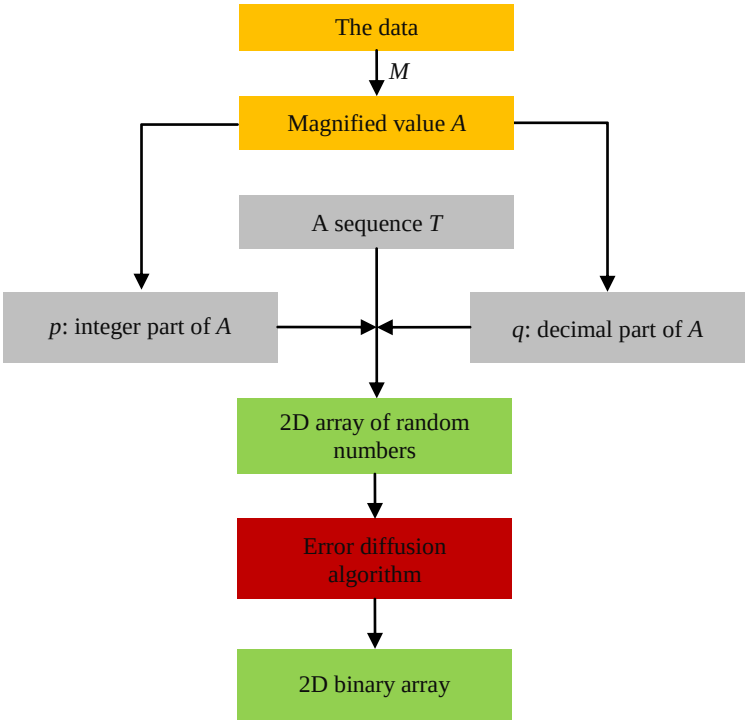

(a)

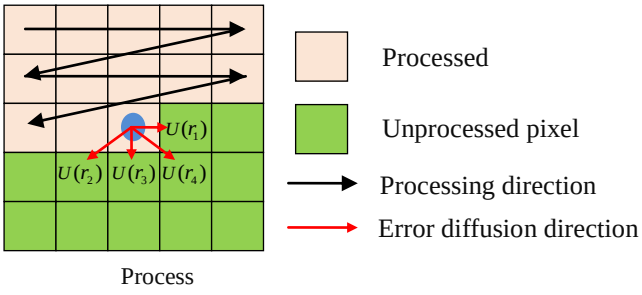

Process

(b)

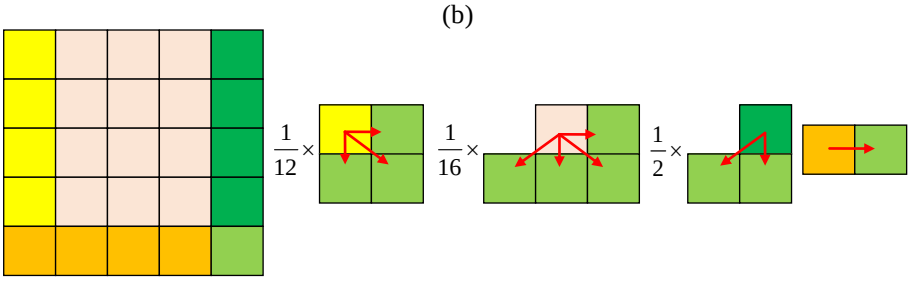

(c)

Figure 4.1 (a) A flow chart of the proposed binary array generation approach, (b) an error diffusion algorithm, and (c) coefficient distributions in a modified error diffusion algorithm.

$$\hat{z}_i = \begin{cases} 0 & \text{if } z_i < 0.5 \\ 1 & \text{if } z_i \geq 0.5 \end{cases}, \tag{4.1}$$

where z_i denotes the ith pixel in the generated 2D array C and $\hat{z}_i$ denotes the generated binary value.

(ii) In the error diffusion algorithm [160–162], the difference between the processed pixel value and its binary representation (i.e., 0 or 1) is distributed and added to its neighboring pixels with a certain weighting ratio in each direction, as schematically illustrated in Fig. 4.1(b). Here, $U(r_1)$, $U(r_2)$, $U(r_3)$ and $U(r_4)$ denote dithering coefficients. The sum of dithering coefficients is equal to 1.

$$U(r_1)+U(r_2)+U(r_3)+U(r_4)=1. \tag{4.2}$$

Here, a modified error diffusion algorithm with designed dithering coefficients is used, and four types of dithering coefficients, i.e., (5/12, 3/12, 4/12), (7/16, 3/16, 5/16, 1/16), (1/2, 1/2) and (1) in Fig. 4.1(c), are correspondingly applied until all pixels in the generated 2D arrays C are converted into binary. Therefore, the sum of each generated binary pattern can be equal to its corresponding magnified value A in practical applications, e.g., via a flexible adjustment of the magnification factor M with a removal of the decimal part q.

4.2.2 Optical data encoding and decoding

In the previous work [153], a reference pattern should be alternately utilized to correct dynamic scaling factors in complex scattering environments, and the transmission of each pixel of an analog signal needs at least four 2D patterns. Here, a new optical encoding scheme with a modified differential method is proposed, and only two 2D binary arrays are required for the transmission of each analog value. A flow chart for the proposed optical data encoding and decoding method is shown in Fig. 4.2. Assumed that an analog signal to be transmitted contains N pixel values (S_i,

i=1,2,…,N), a constant α and a variable β_i (i=1,2,…,N) are used to realize a differential process and a relationship among S_i, α and β_i is given by

$$S_i = \alpha - \beta_i. \tag{4.3}$$

All values, i.e., α and β_i, are multiplied by the magnification factor M, and then are sequentially encoded into 2D binary arrays (respectively denoted as D and P_i) using the proposed algorithm. The generated 2D binary arrays are sequentially embedded into a SLM in the developed optical data transmission system. Then, the SLM is illuminated by a collimated light source, and the modulated wave propagates through dynamic and complex scattering media. A series of light intensities corresponding to the 2D binary arrays are recorded by a single-pixel bucket detector at the receiving end. According to wave propagation theory [46,132], the recorded light intensity I_{out} can be described by

$$I_{\text{out}} \approx u\left|\mathrm{E}_{in}\right|^2, \tag{4.4}$$

where u denotes a scaling factor and E_{in} denotes the wavefront. The recorded light intensity corresponding to each 2D binary array (i.e., D and P_i) can be respectively described by

$$\begin{aligned} B_{i1} &\approx u(t_i)\iint D(x,y)\,\mathrm{dxdy} \\ &= u(t_i) M\alpha, \end{aligned} \tag{4.5}$$

$$\begin{aligned} B_{i2} &\approx u(t_{i+1})\iint P_i(x,y)\,\mathrm{dxdy} \\ &= u(t_{i+1}) M\beta_i, \end{aligned} \tag{4.6}$$

where (x, y) denotes a coordinate, and B denotes light intensity collected by single-pixel detector. At time t_i, the 2D binary array D is embedded into the SLM. At time t_{i+1}, a 2D binary array P_i is embedded into the SLM.

In Eqs. (4.5) and (4.6), since t_i is close to t_{i+1}, it can be assumed that two adjacent scaling factors are the same, i.e.,

$$u(t_i) \approx u(t_{i+1}). \tag{4.7}$$

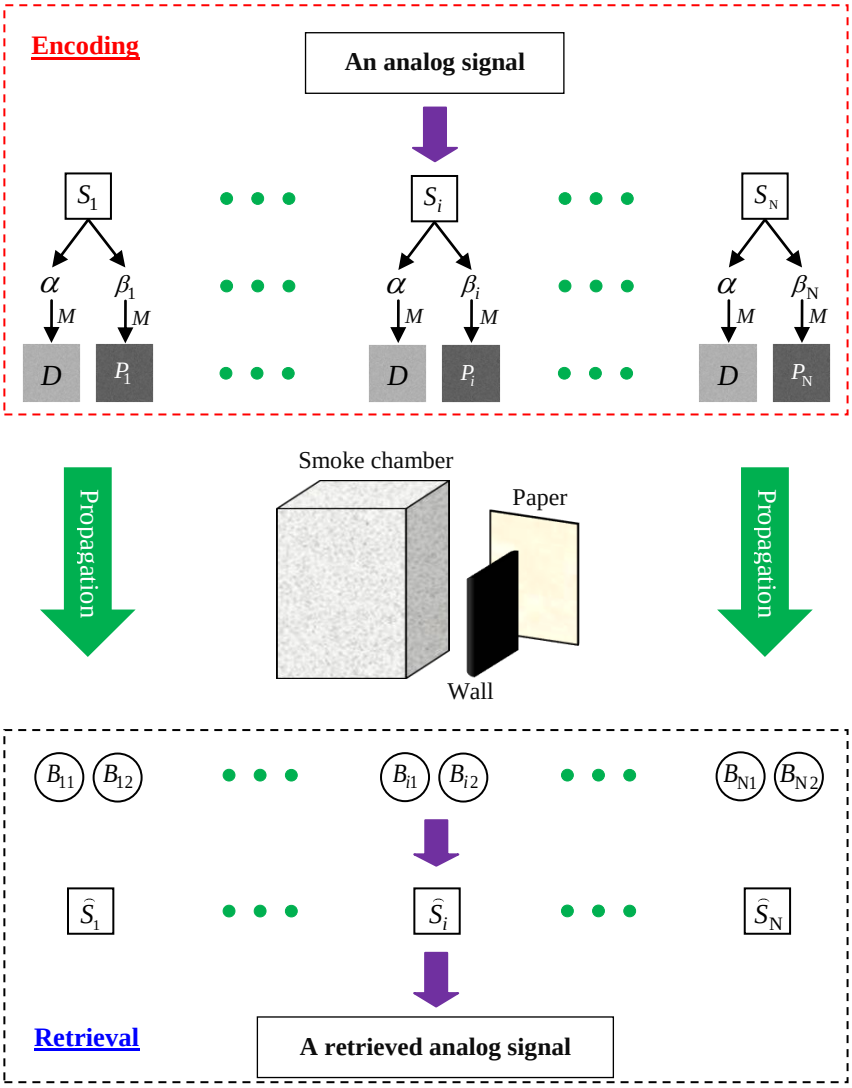

Figure 4.2 A flow chart for the proposed method to realize high-fidelity free-space optical analog-signal transmission in dynamic and complex scattering environment. *D* and P_i (i=1,2,…,N) denote a series of 2D binary arrays obtained by using the proposed algorithm.

Therefore, a signal $\hat{S}_i$ retrieved at the receiving end can be described by

$$\begin{aligned} \hat{S}_i &= \frac{B_{i1}}{u(t_i)M} - \frac{B_{i2}}{u(t_{i+1})M} \\ &\approx \frac{1}{u(t_i)M}(B_{i1} - B_{i2}) \end{aligned} \tag{4.8}$$

Based on Eq. (4.8), the proposed method can realize high-fidelity free-space optical data transmission in dynamic and complex scattering environments using only two 2D binary arrays for the transmission of each pixel of an analog signal.

4.3 Experimental results and discussion

4.3.1 Experimental setup

A series of optical experiments are conducted to verify the proposed method. A schematic experimental setup is shown in Fig. 4.3. A diode-pumped green laser (CrystaLaser, CL532-025-S) is utilized as light source. The laser power is 25.0 mW, and wavelength of the laser is 532.0 nm. The wave is expanded with an objective lens and collimated with a lens. The expanded and collimated wave is reflected by a mirror, and illuminates an amplitude-only SLM (Holoeye, LC-R720) with pixel size of 20.0 μm. The series of generated 2D binary arrays (i.e., D and P_i) is sequentially embedded into the SLM to modulate optical wave. The switching rate of SLM is 1.25Hz. The modulated wave propagates through dynamic and complex scattering media. Complex scattering consists of two parts, i.e., dynamic smoke and non-line-of-sight. The dynamic smoke is generated in a transparent acrylic chamber. The artificially-generated smoke is produced with a smoke generator (HALFSun, power of 3000W and pumping rate of 973.0 cm^3/s) and smoke oil. The smoke oil is a mixture of glycerol and water. Around a corner is composed of a wall (i.e., a protective screen) and an A4 paper (a reflective surface). A single-pixel bucket detector (Newport, 918D-UV-OD3R) is used to collect light intensities at the receiving end. No lens is placed before the single-pixel bucket detector. Axial distance d_1 between the SLM and front side of smoke chamber is 30.0 cm, and axial distance d_3 between back side of smoke chamber and A4 paper is 12.0 cm. The distance d_4 between A4 paper and

single-pixel bucket detector is 5.0 cm. The dimension of smoke chamber is 30 (L)×30 (W)×40 (H) cm^3, and axial distance d_2 is 30.0 cm.

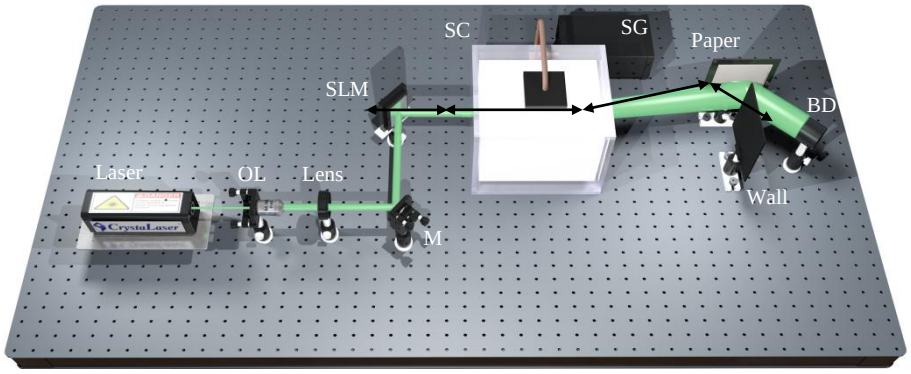

Figure 4.3 A schematic experimental setup for the proposed high-fidelity free-space optical data transmission in dynamic and complex scattering environment (i.e., dynamic smoke and non-line-of-sight): OL, Objective lens; M, Mirror; SLM, Amplitude-only spatial light modulator; SC, Smoke chamber; SG, Smoke generator; BD, Single-pixel bucket detector.

4.3.2 Attenuations

Dynamic and complex scattering environment in Fig. 4.3 consists of dynamic smoke and non-line-of-sight, and a direct metric to describe the attenuation in free space is optical path loss (*PL*). When each 2D binary array is embedded and displayed, the *PL* can be correspondingly calculated by using incident light intensity and collected light intensity. In optical experiments, the *PL* is calculated to describe dynamic changes in transmission environment, which is described by

$$PL = -10 \times \log_{10} \frac{I_{\mathrm{r}}}{I_{\mathrm{t}}}, \tag{4.9}$$

where I_t denotes the collected single-pixel light intensity just before smoke chamber and I_{r} denotes light intensity recorded by single-pixel bucket detector. To eliminate the errors, several recordings just before smoke chamber are used to calculate an average incident light intensity described by

$$I_t = \frac{1}{\Re} \sum_{i=1}^{\Re} I_{ti}, \tag{4.10}$$

where $\Re$ denotes the total number of measurements and I_{ti} denotes collected single-pixel light intensity recorded just before smoke chamber. Here, average incident light intensity I_t is 0.34 mW.

4.3.3 Experimental results

The pumping rate of smoke generator is 973.0 cm^3/s, and pumping durations can be flexibly adjusted in optical experiments to generate different smoke concentrations in the chamber. Real-time properties in the optical transmission path are shown in Fig. 4.4(a), when different amount of smoke is respectively pumped into the chamber. The relationships between sampling time and light intensities collected by single-pixel detector are given. The collected light intensities are small at the beginning, and increase with sampling time. Smoke pumped into the chamber has a high concentration at the beginning, and the propagating wave is strongly scattered. When the pumping duration is longer, more smoke is pumped into the chamber. After the liquefaction and sedimentation, the longer pumping duration leads to the larger amount of liquefied smoke adhered to surface of the chamber. The lowest light intensity, i.e., 6.0×10^{-7} W, is obtained at its stable state, when the pumping duration is 50 s. The *PL* changed with sampling time is shown in Fig. 4.4(b). As sampling time increases, the *PL* decreases due to liquefaction and sedimentation of the smoke in the chamber.

Apart from dynamic smoke, optical data transmission is also affected by the designed non-line-of-sight in Fig. 4.3. Two parameters, i.e., separation distance d and detection angle θ respectively in Figs. 4.5 (a) and (b), are analyzed. In optical experiments, default value of the separation distance d is 4.0 cm, and default value of detection angle θ is 45 °.

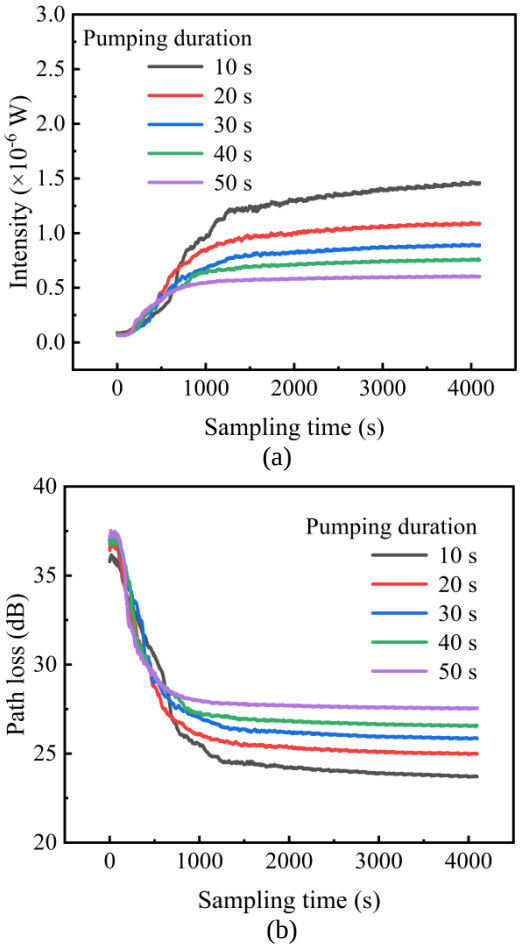

Figure 4.4 (a) The relationships between sampling time and optical intensities collected at the receiving end when pumping duration (i.e., 10 s, 20 s, 30 s, 40 s and 50 s) is different, and (b) the relationships between sampling time and the *PL* when pumping duration (i.e., 10 s, 20 s, 30 s, 40 s and 50 s) is different.

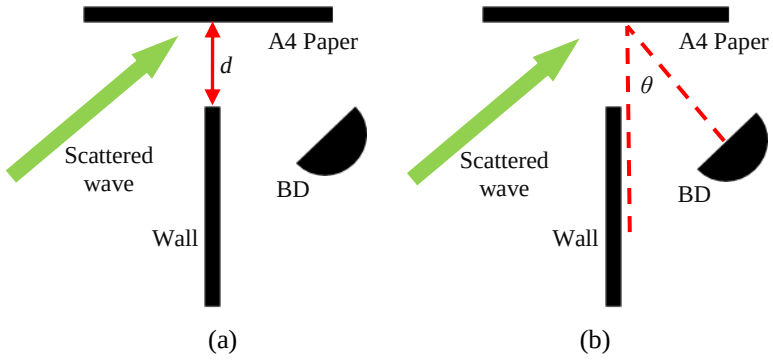

Figure 4.5 (a) A schematic of separation distance *d*, and (b) a schematic of detection angle *θ*.

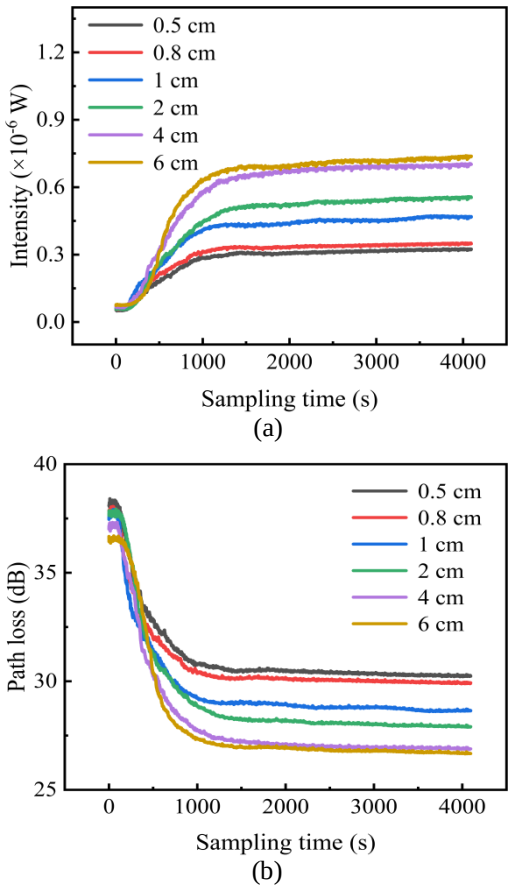

Figure 4.6 (a) The relationships between sampling time and light intensities collected at the receiving end when different separation distances (i.e., 0.5 cm, 0.8 cm, 1.0 cm, 2.0 cm, 4.0 cm and 6.0 cm) are respectively used, and (b) the relationships between sampling time and the *PL* when different separation distances (i.e., 0.5 cm, 0.8 cm, 1.0 cm, 2.0 cm, 4.0 cm and 6.0 cm) are respectively used.

The separation distance d is changed in a range of 0.5 to 6.0 cm, and smoke pumping duration is 30 s. The experimental results are shown in Figs. 4.6(a) and 4.6(b). As can be seen in Fig. 4.6(a), the change trends of recorded light intensities are similar, when different separation distances d are respectively used. As sampling time increases, the recorded light intensities increase due to liquefaction and sedimentation of the smoke in the chamber. When the separation distance around the corner is small (e.g., 0.5 or 0.8 cm), the wall largely blocks the propagating wave, and collected light intensities are significantly reduced. When the separation distance is large (e.g., 4.0 or 6.0 cm), the wall partially blocks the propagating wave. The collected light intensities are close, when the separation distances of 4.0 cm and 6.0 cm are used. The *PL* is also

calculated and shown in Fig. 4.6(b). It is illustrated that the *PLs* are high at the beginning, and decrease with sampling time to remain stable in the end. The signals retrieved at the receiving end are evaluated by using MSE and PSNR.

To accurately evaluate dynamic and complex scattering environments, *APL* is further calculated by

$$APL = \frac{1}{2N}\sum_{i=1}^{2N} PL_i, \tag{4.10}$$

where PL_i denotes the loss obtained when each generated 2D binary array is embedded into the SLM. The typically retrieved analog signals are shown in Figs. 4.7(a)–4.7(d), when different separation distances are respectively used. As can be seen in Figs. 4.7(a)–4.7(d), high PSNR values and low MSE values can be obtained, which means that the analog signals are retrieved with high fidelity. It is experimentally found that when the separation distance *d* is larger than 0.5 cm, the proposed method can realize high-fidelity optical analog-signal transmission in dynamic and complex scattering environments.

The detection angle θ around a corner is also studied, and is changed in a range of 0 ° to 90 °. The experimental results are shown in Figs. 4.8(a) and 4.8(b), when different detection angles θ, i.e., 0 °, 25 °, 45 °, 65 °, and 90 °, are respectively used. Here, smoke pumping duration is 30 s. As can be seen in Fig. 4.8(a), the change trends of recorded light intensities are similar. When the sampling time increases, the recorded light intensities increase due to liquefaction and sedimentation of the smoke in the chamber. When the detection angle θ is 45 °, the largest light intensity is collected at the stable state. The *PLs* are also calculated and given in Fig. 4.8(b). It is illustrated in Fig. 4.8(b) that the *PL* is high at the beginning, and decreases with sampling time to remain stable in the end.

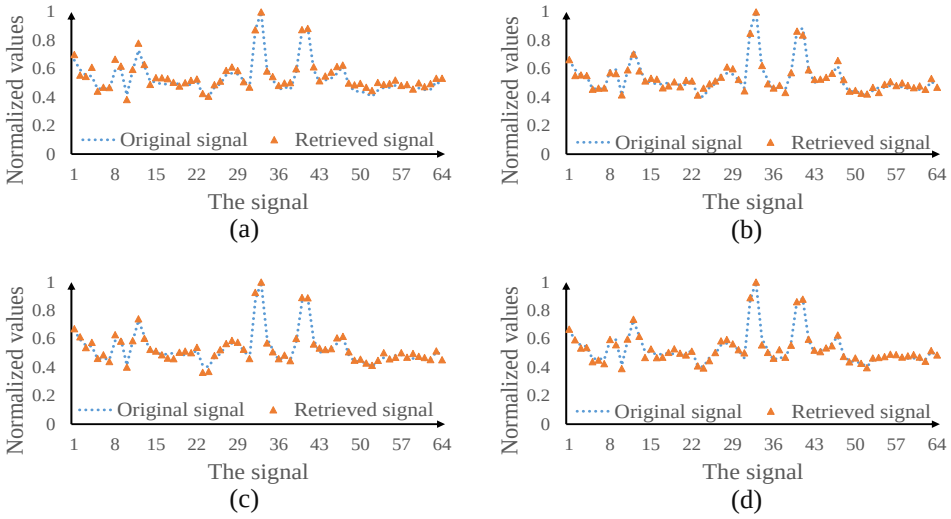

Figure 4.7 (a)-(d) The typical signals experimentally retrieved at the receiving end when different separation distances (i.e., 0.5 cm, 0.8 cm, 2.0 cm, and 4.0 cm) are respectively used. The *APL* is 30.76 dB, 30.65 dB, 30.27 dB, and 29.07 dB in (a)-(d), respectively. PSNR values of the retrieved signals in (a)-(d) are 30.14 dB, 32.96 dB, 33.52 dB and 34.68 dB, respectively. MSE values of the retrieved signals in (a)-(d) are 9.68×10^{-4}, 5.06×10^{-4}, 4.44×10^{-4} and 3.40×10^{-4}, respectively.

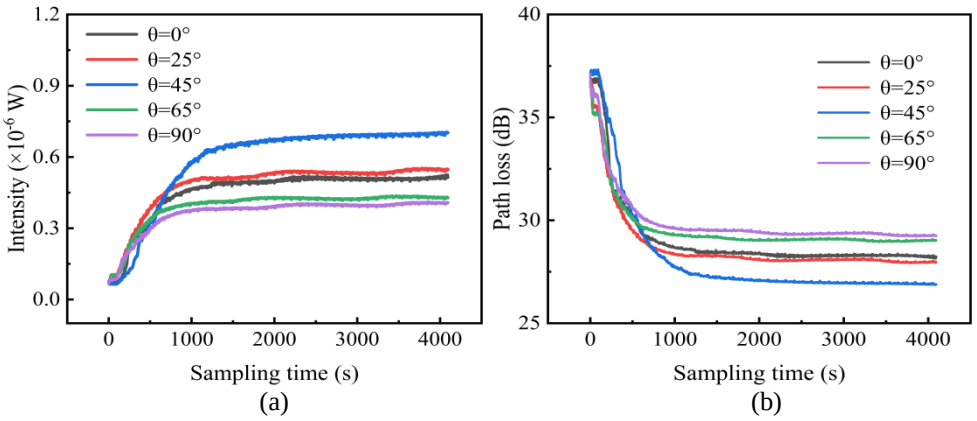

Figure 4.8 (a) The relationships between sampling time and light intensities experimentally collected at the receiving end when different detection angles θ (i.e., 0°, 25°, 45°, 65°, and 90°) are respectively used, and (b) the relationships between sampling time and the *PLs* when different detection angles θ (i.e., 0°, 25°, 45°, 65°, and 90°) are respectively used.

The typically retrieved signals are shown in Figs. 4.9(a)–4.9(d), when detection angle is 0°, 45°, 65° and 90°, respectively. PSNR values of the retrieved signals in Figs. 4.9(a)–4.9(d) are 33.95 dB, 37.55 dB, 33.66 dB and 32.42 dB, respectively. MSE values in Figs. 4.9(a)–4.9(d) are 4.03×10^{-4}, 1.76×10^{-4}, 4.30×10^{-4} and 5.73×10^{-4}, respectively. It is illustrated in Figs. 4.9(a)–4.9(d) that the detection coverage is large

at the receiving end, and high mobility and low pointing errors are realized in the developed optical data transmission system.

It has been experimentally demonstrated in Figs. 4.4 and 4.6–4.9 that the loss is mainly induced by smoke pumping duration, separation distance and detection angle. A relationship between the *APL* and PSNR values of the retrieved signals is further given in Figs. 4.10(a). Four irregular analog signals are tested. It is demonstrated in Fig. 4.10(a) that analog signals retrieved at the receiving end are of high quality, when the *APL* is lower than 29.0 dB. The typical signals retrieved at the receiving end are shown in Figs. 4.10(b)–4.10(e). Here, smoke pumping duration is 30 s, and separation distance d is 4.0 cm. The detection angle θ is 45 °. PSNR values of the retrieved signals in Figs. 4.10(b)–4.10(e) are 35.23 dB, 37.13 dB, 36.01 dB and 35.83 dB, respectively. MSE values of the retrieved signals in Figs. 4.10(b)–4.10(e) are 3.00×10^{-4}, 1.94×10^{-4}, 2.51×10^{-4} and 2.61×10^{-4}, respectively. As can be seen in Figs. 4.10(b)–4.10(e), the retrieved analog signals are of high fidelity in dynamic and complex scattering environments.

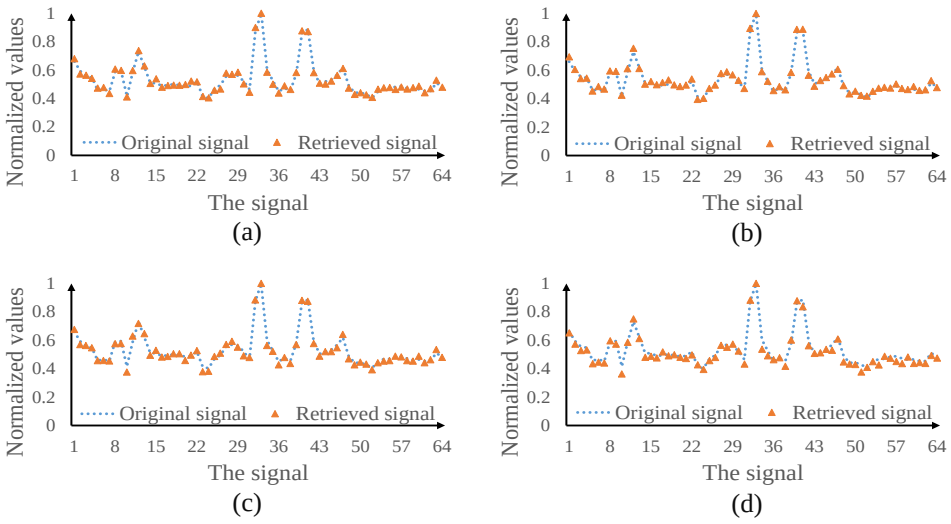

Figure 4.9 The typically retrieved analog signals experimentally obtained when the detection angle is (a) 0 °, (b) 45 °, (c) 65 ° and (d) 90 °. The *APL* is 28.44 dB, 27.19 dB, 29.14 dB, and 29.50 dB in (a)-(d), respectively.

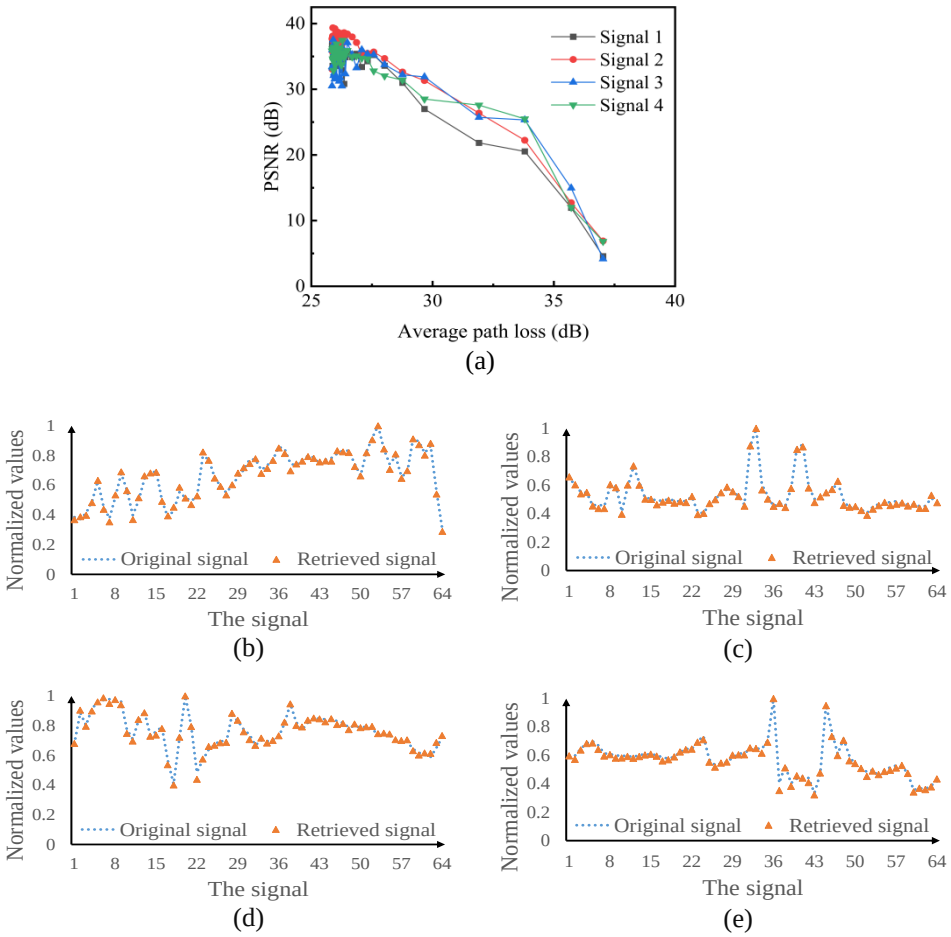

Figure 4.10 (a) The relationships between the *APL* and PSNR values of the retrieved signals, and (b)-(e) typical signals retrieved respectively with different *APL*s (i.e., 27.57 dB, 27.61 dB, 27.55 dB, 27.65 dB).

4.4 Summary

A new scheme has been proposed to realize high-fidelity free-space optical analog-signal transmission in dynamic and complex scattering environments using binary encoding with a modified differential method. An algorithm is developed to generate a series of 2D binary arrays as information carriers to be used in optical transmission channel. The proposed method employs only two 2D binary patterns for the transmission of each pixel of an analog signal in dynamic and complex scattering environments, and only the half number of measurements is used compared to that in conventional methods. Dynamic scaling factors can be effectively corrected as verified in optical experiments to realize high-fidelity analog-signal retrieval at the

receiving end. It is experimentally demonstrated that analog signals retrieved at the receiving end are always of high fidelity using the proposed method, when the *APL* is less than 29.0 dB. The proposed approach could open up a novel research perspective for high-fidelity free-space optical analog-signal transmission through dynamic and complex scattering media.

Chapter 5 Secured optical transmission

5.1 Introduction

Classsical ghost diffraction [6] originates from quantum, which is further explored to be applied in different areas, e.g., data transmission and imaging. In ghost diffraction, a single-pixel detector is utilized to collect light intensities, and correlation algorithms with 2D illumination patterns and the collected light intensities are used to reconstruct image of the object. Ghost diffraction was directly treated as an encryption method in previous studies [39,163]. The illumination patterns and collected single-pixel light intensities are respectively used as security keys and ciphertexts. Recently, free-space optical data transmission with high fidelity was found to be feasible using ghost diffraction [164]. However, high-fidelity secured optical data (ghost) transmission in scattering environment is always challenging, since the propagation of waves through scattering media poses inherent limitations in enabling high-fidelity optical data (ghost) transmissions and information loss is unavoidable. Moreover, few research has been conducted on the data security of ghost diffraction and transmission. Hence, it is desirable and important to explore a secured ghost diffraction and transmission scheme. In terms of optical encoding approaches, security keys are often numerically designed [107,108], and these methods may be vulnerable to the attacking algorithms [165] with sufficiently computational capability. Alternatively, physical-layer security provides unbreakable, provable and quantifiable secrecy, which makes it to be one of the best solutions [109,112,166–171]. There are some physical-layer security methods, e.g., quantum communication [168,169] and chaos communication [170,171]. Quantum encryption needs stringent devices, and the rate of quantum key distribution

could be limited [168]. Messages are encrypted with computer-generated pseudo-code or chaotic signals, which may be intercepted using the attacking methods of direct detection, linear filtering, and synchronization [172]. Therefore, a promising approach to solving the problem is that the computer-generated keys can be combined with physically-generated keys to achieve high security. It is desirable to develop a feasible and easy-to-implement method for enabling ghost diffraction through scattering media in free space with high fidelity and high security.

In this Chapter, ghost diffraction and transmission with high fidelity and high security are reported. A series of 2D arrays of random numbers are used to encode each pixel value of data to be transmitted, e.g., analog signals or images as ghosts, and a random magnification factor is distributed to process each pixel value. Dynamic scaling factors are generated physically in free-space optical transmission. Nonlinear variation of scaling factors is physically produced by using absorptive filters. Experimental results demonstrate that the proposed method realizes ghost diffraction and transmission with high fidelity and high security. The proposed method provides a large key space and guarantees the security of free-space optical data (ghosts) transmissions, since security keys are generated by using computer-generated magnification factors and physically-generated dynamic scaling factors. The corresponding publications of this Chapter are listed as follows:

(1) **Yonggui Cao**, Yin Xiao, Zilan Pan, Lina Zhou, and Wen Chen, "Physically-secured ghost diffraction and transmission," IEEE Photonics Technology Letters, **34**(22), 1238–1241 (2022).

(2) **Yonggui Cao**, Yin Xiao, and Wen Chen, "Securing 2D information carriers over dynamic and turbulent media in a free-space optical channel," Optics Letters, **48**(13), 3491–3494 (2023).

5.2 Secured optical transmission through static scattering media

A 2D array of random numbers is first generated as follows to encode each pixel value *S* of the signal or image (as ghosts): (i) Value *A* is obtained by a multiplication of original pixel value *S* and a magnification factor *M*. The integer part of *A* is represented as *p*, and *q* represents the decimal part of *A*. (ii) A random sequence T is generated, length of which is 2*p*. Half of sequence T is random values between 0 and 1, and the other half is obtained by using the difference between 1 and each value of the first half. (iii) A 2D array of random numbers is generated by arbitrarily assigning the decimal value *q* and the sequence T to (2*p*+1) positions in a predesigned zero matrix. The intermediate variable sequence T is used in the final step of the proposed algorithm to generate the 2D arrays of random numbers (P).

Pixel values (i.e., S_i, i=1,2,3,…,N) of the ghost (e.g., an image) are sequentially encoded into a series of 2D arrays of random numbers (i.e., P_i, i=1,2,3,…,N). To encode each pixel, a random magnification factor (i.e., M_i, i=1,2,3,…,N) is correspondingly used. The magnification factors are used to also make the encoded neighboring pixels have a big difference (i.e., several orders of magnitude). A differential method is used to generate two 2D arrays of random numbers (i.e., D_{i1} and D_{i2}, i=1,2,3,…,N) corresponding to each generated 2D array of random numbers during optical data transmission to further eliminate environmental noise, where D_{i1}=B+P_i, D_{i2}=B-P_i, and B denotes a real and non-negative value. A SLM modulates the optical field information in free space by sequentially embedding the generated 2D arrays of random numbers as information carriers. The collected light intensity I_{out} at the receiving end and incident optical field E_{in} have a proportional relationship

[132], i.e., $I_{\text{out}} \approx u\left|E_{\text{in}}\right|^2$ where u represents a scaling factor. In conventional methods [164], scaling factors are always considered to be a constant. Here, time-dependent scaling factors are present in optical data transmission channels. A random scaling factor, i.e., f_{i1} or f_{i2} (i=1, 2, 3,…,N), is generated and applied to each 2D array of random numbers (i.e., D_{i1} or D_{i2}, i=1,2,3,…,N), when different absorptive filters are used in Figs. 5.1 and 5.2. Therefore, a series of magnification factors and physically-generated dynamic scaling factors can serve as security keys, and single-pixel light intensities collected at the receiving end are used as ciphertexts. When correct keys (i.e., magnification factors and scaling factors) are not used, the transmitted data cannot be correctly retrieved at the receiving end. By conducting a series of optical experiments, the proposed method is capable of implementing high-fidelity and high-security ghost diffraction and transmission. As a clear illustration of the proposed method, a flow chart of the proposed physically-secured ghost diffraction and transmission scheme is shown Fig. 5.1.

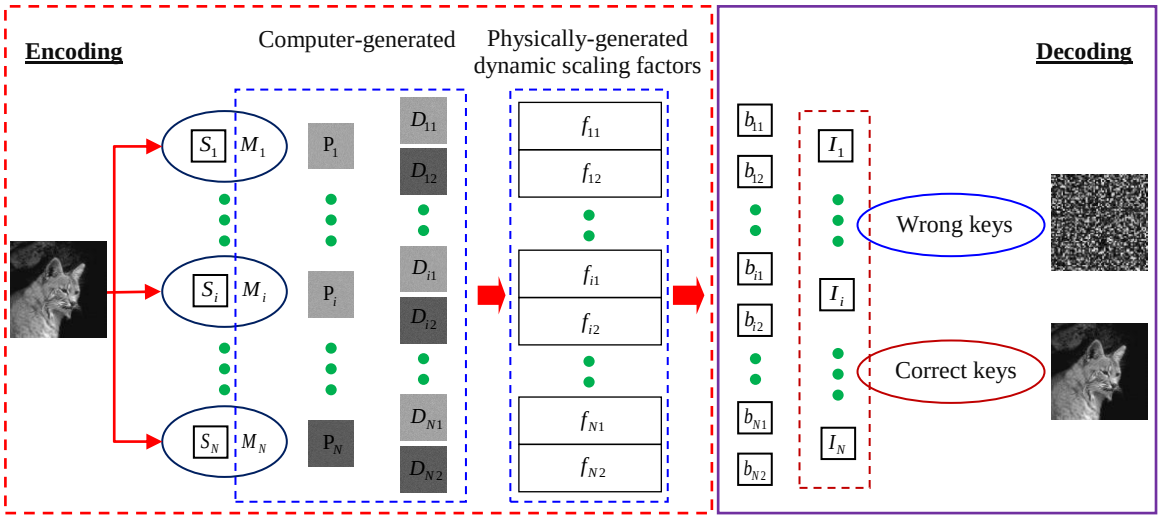

Figure 5.1 A flow chart of the proposed physically-secured ghost diffraction and transmission scheme.

5.3 Experimental results in static scattering media

Figure 5.2 shows an experimental setup for the proposed physically-secured ghost diffraction scheme. Control of the laser diode current is performed with a laser driver (Thorlabs, LDC205C) in a range of 0 to 500 mA. An electronic controller (Thorlabs, TED200C) stabilizes the laser at room temperature. A laser diode with wavelength of 690.0 nm is utilized in optical experiments and inserted into a laser diode mount (Thorlabs, LDM56/M). The laser beam is reflected by a mirror, and illuminates the SLM (Holoeye, LC-R720) with a pixel size of 20.0 μm. Then, the modulated wave propagates through an absorptive filter (Thorlabs, DG10–1500) and scattering media in free space. Here, a typical example of scattering media, i.e., two cascaded diffusers (Thorlabs, DG10-1500), is used to verify the proposed method. A single-pixel bucket detector (Newport, 918D-UV-OD3R) is placed at the receiving end to collect light intensities. Axial distance between the SLM and absorptive filter is 100.0 mm, and axial distance between absorptive filter and the first diffuser is 75.0 mm. Axial distance between the two diffusers is 10.0 mm, and axial distance between the second diffuser and single-pixel bucket detector is 75.0 mm. The SLM modulates the input light wave when the series of generated 2D arrays of random numbers is sequentially embedded into the SLM, and then the modulated light wave propagates through absorptive filter. The optical transmission channel can be used to generate dynamic scaling factors. The ghost signals or images can be effectively retrieved, only when correct security keys, i.e., magnification factors and scaling factors, are applied.

Optical transmission environments without and with scattering media (i.e., two cascaded diffusers, Thorlabs DG10-1500) in free space are used to verify the proposed physically-secured ghost diffraction. The proposed method can also be applied in other types of scattering environment [173,174] to evaluate its effectiveness

and robustness. The label of x-axis (i.e., combination case) in Fig. 5.3 means that different combinations of randomly selected absorptive filters are conducted at the

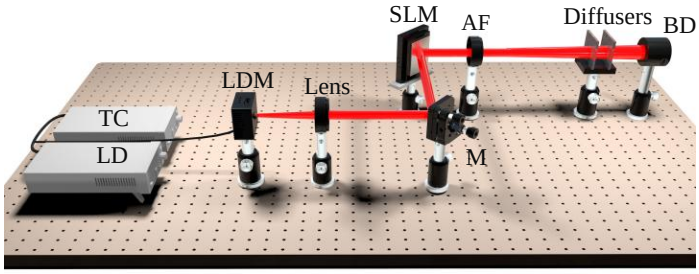

Figure 5.2 A schematic experimental setup for the proposed physically-secured ghost diffraction and transmission scheme. TC: Temperature controller; LD: Laser driver; LDM: Laser diode mount; M: Mirror; SLM: Amplitude-only spatial light modulator; AF: Absorptive filter; BD: Single-pixel (bucket) detector. Two cascaded diffusers are employed as a typical example of scattering media in this study.

same time in the experiment to realize the physical encryption process. Nonlinear variation of scaling factors can be easily obtained with different combination cases, and the large key space of physical security keys in the experiment is realized. To encrypt different pixel values, absorptive filters are changed constantly during the data transmission process. As shown in Figs. 5.3(a) and 5.3(b), nonlinear variation of scaling factors is always realized in free space without and with scattering media, when different absorptive filters are used at the transmitter in the optical transmission channel.

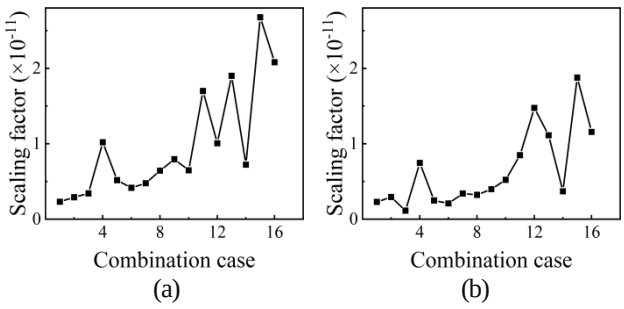

Figure 5.3. (a) Nonlinear variation of scaling factors in free space without scattering media, and (b) nonlinear variation of scaling factors in free space with scattering media.

Then, a series of physically-secured ghost diffraction experiments are conducted. Two irregular analog signals are used as a typical example, and each signal has 64

pixels to be encoded into 128 2D arrays of random numbers which are sequentially displayed by the SLM. Experimental results obtained in these optical transmission environments are shown in Fig. 5.4. As can be seen in Figs. 5.4(a) and 5.4(c), it is

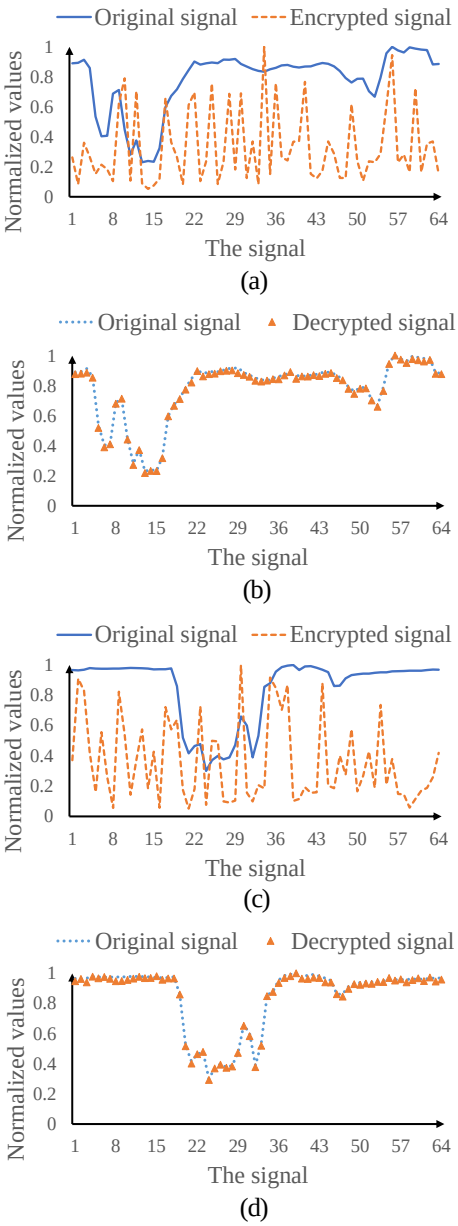

Figure 5.4. (a) and (c) A comparison between the experimentally encoded signal and original ghost, and (b) and (d) a comparison between the decoded signal and original ghost: (a) and (b) Experimental results obtained in free space without scattering media; (c) and (d) experimental results obtained in free space with scattering media. The MSE values corresponding to (a)-(d) are 0.28, 1.86×10^{-4}, 0.33 and 1.78×10^{-4}, respectively. The PSNR values corresponding to (a)-(d) are 5.53 dB, 37.31 dB, 4.79 dB and 37.49 dB, respectively.

impossible to reconstruct original ghost signals from the signals obtained at the receiving end, since original ghost signals are encoded into random values. Decoded signals overlap with original signals, when correct security keys are applied as shown in Figs. 5.4(b) and 5.4(d). Quantitative evaluation of ghost retrieval is realized by calculating PSNR and MSE. The MSE and PSNR values are given in Fig. 5.4. It is experimentally demonstrated that high-fidelity and high-security ghost diffraction and transmission can be effectively realized in the proposed method.

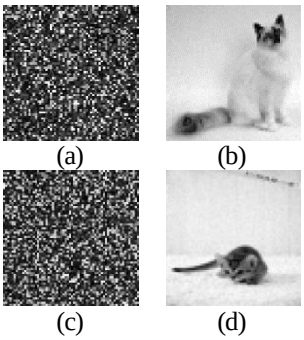

Figure 5.5. The experimentally encoded ghost images in (a) free space without scattering media and (c) free space with scattering media, and the decoded ghost images obtained in free space (b) without scattering media and (d) with scattering media when correct security keys are applied. The MSE values for (a)-(d) are 0.32, 2.40×10^{-4}, 0.37 and 1.71×10^{-4}, respectively. The PSNR values for (a)-(d) are 4.92 dB, 36.20 dB, 4.34 dB and 37.67 dB, respectively.

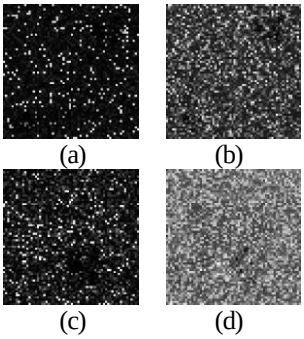

Figure 5.6. (a) and (c) The decoded ghost images obtained by using correct magnification factors and wrong physically-generated scaling factors; and (b) and (d) the decoded ghost images obtained by using wrong magnification factors and correct physically-generated scaling factors: (a) and (b) Free space without scattering media; (c) and (d) free space with scattering media. The MSE values corresponding to (a)-(d) are 0.59, 0.30, 0.58 and 0.10, respectively. The PSNR values corresponding to (a)-(d) are 2.31 dB, 5.27 dB, 2.33 dB and 9.95 dB, respectively.

Optical experiments to test the transmission of two grayscale images of 64×64 pixels are also conducted to verify the proposed method. As can be seen in Figs. 5.5 (a) and 5.5(c), original ghost images are effectively encoded into noise-like patterns at the receiving end. When correct security keys are applied, ghost images can be retrieved with high fidelity as shown in Figs. 5.5(b) and 5.5(d). It is demonstrated by the given high PSNR values and low MSE values that the proposed high-fidelity and high-security ghost diffraction scheme is feasible and effective.

Performance of security keys is further analyzed in the proposed physically-secured ghost diffraction scheme. The decoded ghost images using different keys to evaluate the security are shown in Figs. 5.6(a) and 5.6(d). As can be seen in Figs. 5.6 (a) and 5.6(c), when correct magnification factors and wrong physically-generated scaling factors are used, no information about the plaintexts can be obtained from the decoded ghost images. As can be seen in Figs. 5.6(b) and 5.6(d), when wrong magnification factors and correct physically-generated scaling factors are used, it is also impossible to obtain any information about the plaintexts from the decoded ghost images. It is experimentally verified that the series of computer-generated magnification factors and physically-generated dynamic scaling factors can provide a large key space compared with other existing methods, and the proposed physically-secured ghost diffraction scheme possesses high security. In addition, since the security key space is very large, the proposed method shows high resistance to brute force attacks.

5.4 Secured optical transmission through dynamic scattering media

Based on the aforementioned introduction, ghost diffraction could provide a promising alternative to realize a secured free-space optical transmission. However, secured ghost transmission is implemented in free space through static media, and is not applicable in dynamic and turbulent media [107,174–178]. Real-time transmission errors are generated, when the environment keeps changing due to dynamic and turbulent media [54,59]. To realize a secured optical transmission system in dynamic scattering environment, the transmission errors induced by the scattering media need to be corrected temporally and the encrypted transmission data need to be decrypted at the same time. Hence, it is desirable to design an optical approach to realizing secured free-space optical data transmission through dynamic and turbulent media.

Hence, a new scheme is proposed by encoding 2D information carriers to realize high-fidelity secured free-space optical information transmission through dynamic and turbulent media. The transmitted data is transformed into a series of 2D patterns as information carriers. The noise is suppressed using a novel differential method, and a series of random keys are also generated. A different number of absorptive filters are arbitrarily combined to be placed in the optical channel to generate ciphertext with high randomness. The plaintext can be retrieved only when correct keys are used. Feasibility and effectiveness of the proposed method are verified by optical experiments. The practical implementation of the proposed scheme is simple and convenient since additional works are not necessary for the system, e.g., calibration or post-processing for eliminating noise. The proposed method realizes high-fidelity, high-reliability and high-security optical information transmission over dynamic and turbulent media in a free-space optical channel.

As shown in Fig. 5.7, Alice wants to optically transmit information (e.g., an image or an analog signal) to Bob in free space. Each pixel S_i (i=1,2,…,N) of the analog signal is first described by separate values α_i and β_i, i.e., $S_i = \alpha_i - \beta_i$. Then, each value α_i or β_i is transformed into a 2D pattern (i.e., D_i or P_i) using the aforementioned algorithm. This differential method is developed to fully suppress noise, and a series of random security keys ($\alpha_i, i = 1,2,\ldots,N$) are simultaneously generated. The generated 2D patterns, i.e., D_i and P_i, are sequentially and alternately embedded into a SLM to modulate the optical wave. The modulated wave propagates through dynamic and turbulent media in free space, and is collected by a single-pixel detector at the receiving end. A different number of absorptive filters are arbitrarily combined to be placed in the optical channel to modulate light intensities. The collected light intensity I_{out} could have a relationship [132] with incident wave, i.e., $I_{\text{out}} \approx u\left|E_{\text{in}}\right|^2$ where u represents a scaling factor. When scaling factors linearly vary, the designed secured optical transmission system could be attacked. Here, a strategy is further developed to generate ciphertext with high randomness. A different number of absorptive filters (e.g., 1,2,…) are placed in the free-space optical channel at the transmitter, and then the scaling factors can possess dynamic and nonlinear properties. Moreover, scaling factors corresponding to two adjacent 2D patterns (i.e., D_i and P_i) can be assumed to be the same in dynamic and turbulent environments. At the receiving end, collected light intensities b_{i1} and b_{i2} to serve as the ciphertext are respectively described by

$$b_{i1} \approx u_{i1} \iint \mathrm{D}_i\left(x, y\right) dxdy = \alpha_i M_i k_{i1}, \tag{5.1}$$

$$b_{i2} \approx u_{i2} \iint \mathbf{P}_i\left(x, y\right) dxdy = \beta_i M_i k_{i2}, \tag{5.2}$$

where u_{i1} and i_{i2} respectively denote a scaling factor corresponding to 2D patterns D_i and P_i, and $u_{i1} \approx u_{i2}$.

After Bob receives the ciphertext b_{i1} and b_{i2}, he needs to use a series of random keys $(\alpha_i, i = 1,2,\ldots,N)$ to retrieve the plaintext. The decryption can be described by

$$\hat{S}_i = \alpha_i \left(1 - \frac{b_{i2}}{b_{i1}}\right). \tag{5.3}$$

Therefore, Bob can obtain the ciphertext with high randomness owing to the designed optical system, and random security keys can be provided by Alice. Only when correct security keys α_i are used, the transmitted signal, i.e., plaintext, can be retrieved at the receiving end.

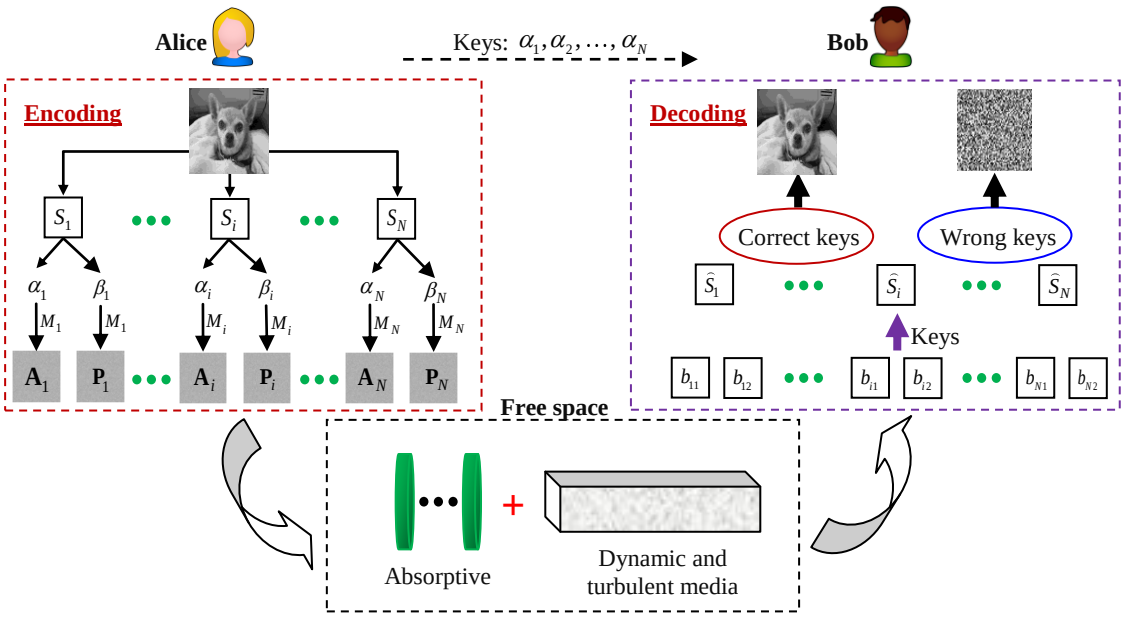

Figure 5.7 A flow chart of the proposed physically-secured optical transmission through dynamic turbulence media.

5.5 Experimental results in dynamic scattering media

A schematic experimental setup is shown in Fig. 5.8 to verify the proposed method. A green laser (CrystaLaser, CL532-025-S) is used as light source. Wavelength and power of the laser are 532.0 nm and 25.0 mW, respectively. The laser is expanded by an objective lens and collimated with a lens followed by the reflection with a mirror.

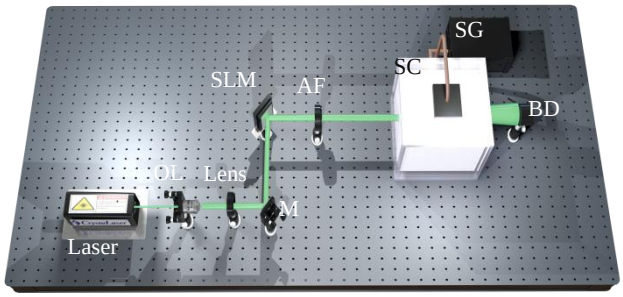

Figure 5.8 A schematic experimental setup for the proposed optically securing information transmission over dynamic turbulence media. OL: Objective lens; M: Mirror; SLM: Amplitude-only spatial light modulator; AF: Absorptive filter; SC: Smoke chamber; SG: Smoke generator; BD: Single-pixel (bucket) detector.

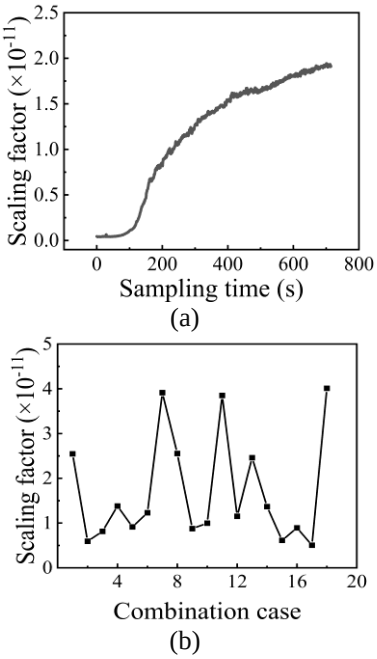

Figure 5.9 (a) A variation of scaling factors corresponding to dynamic and turbulent media in free space, and (b) a nonlinear variation of scaling factors in dynamic and turbulent media. A combination case denotes a different number of absroptive filters to be placed in the free-space optical transmission channel.

The reflected wave is modulated by an amplitude-only SLM (Holoeye, LC-R720) and propagates through dynamic and turbulent media. The optical wave is modulated, when the series of 2D patterns is sequentially and alternately embedded into SLM. The free-space optical channel also consists of a different number of absorptive filters, a transparent acrylic smoke chamber [size of 30 (L) × 30 (W) × 40 (H) cm^3] and a single-pixel detector (Newport, 918D-UV-OD3R). The smoke is produced by a generator (HALFSun) with power of 3000W and pumping rate of 973.0cm^3/s. Smoke

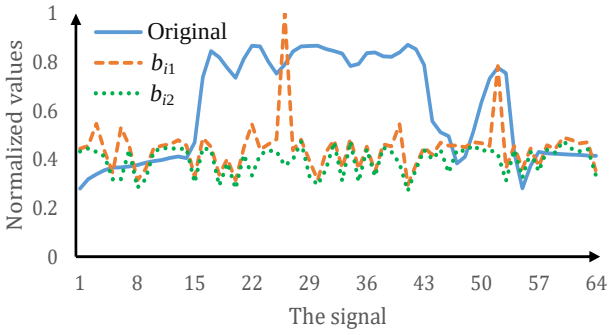

(a)

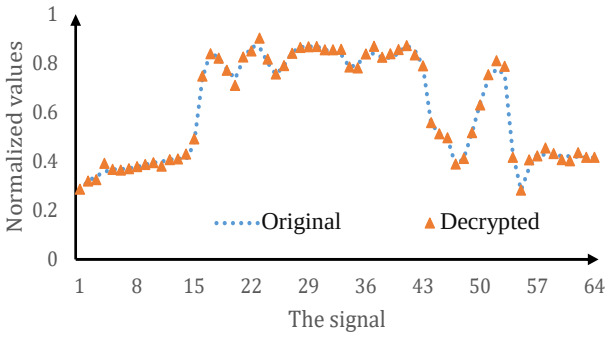

(b)

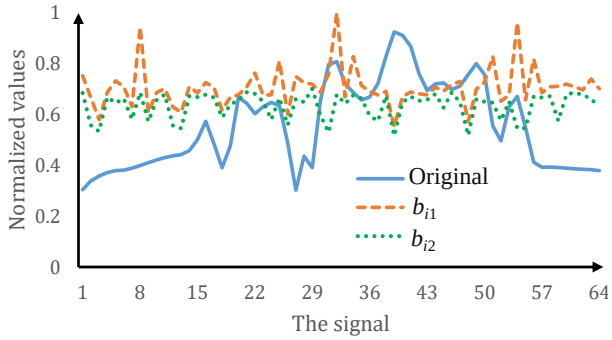

(c)

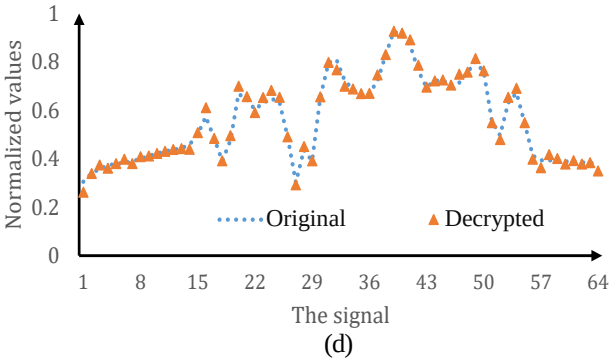

(d)

Figure 5.10 (a) and (c) A comparison between original analog signal and the ciphertexts obtained at the receiving end, and (b) and (d) the decrypted signals obtained when correct security keys are used. MSE and PSNR values corresponding to ciphertexts b_{i1} and b_{i2} in (a) are 7.78×10^{-2}, 11.09 dB, 9.64×10^{-2} and 10.16 dB, respectively. MSE and PSNR values corresponding to ciphertexts b_{i1} and b_{i2} in (c) are 5.60×10^{-2}, 12.52 dB, 3.83×10^{-2} and 14.17 dB, respectively. MSE values corresponding to (b) and (d) are 2.14×10^{-4} and 2.83×10^{-4}, respectively. PSNR values corresponding to (b) and (d) are 36.71 dB and 35.48 dB, respectively.

is pumped into the chamber with pumping time of 15 s. Axial distance between the SLM and absorptive filter is 10.0 cm, and axial distance between absorptive filter and front side of smoke chamber is 20.0 cm. The axial distance between back side of smoke chamber and single-pixel detector is 5.0 cm.

The dynamic property of turbulent media is shown in Fig. 5.9(a). The scaling factors increase with sampling time due to smoke liquefaction and sedimentation. It is experimentally demonstrated that property of dynamic and turbulent media is approximately linear, which could not effectively withstand the attacks. When a different number of absorptive filters are arbitrarily combined (e.g., 1,2,3,…) to be placed in the free-space optical channel, a nonlinear and dynamic change of scaling factors can be obtained as shown in Fig. 5.9(b). Therefore, ciphertexts collected at the receiving end have high randomness in the developed free-space optical data transmission system.

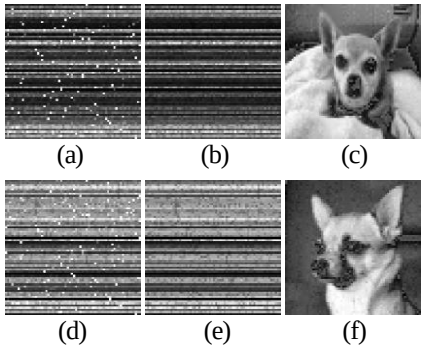

Figure 5.11 (a) and (b) Ciphertexts (i.e., b_{i1} and b_{i2}) corresponding to a grayscale image experimentally encoded in the free-space optical transmission channel through dynamic and turbulent media, (d) and (e) ciphertexts (i.e., b_{i1} and b_{i2}) corresponding to another grayscale image experimentally encoded in the free-space optical transmission channel through dynamic and turbulent media, and (c) and (f) the decrypted images obtained at the receiving end when a series of correct security keys are applied. MSE values corresponding to (a)–(f) are 0.15, 0.16, 4.05×10^{-4}, 0.10, 0.09 and 4.36×10^{-4}, respectively. PSNR values corresponding to (a)–(f) are 8.20 dB, 7.82 dB, 33.92 dB, 9.99 dB, 10.36 dB and 33.60 dB, respectively.

(a) (b)

Figure 5.12 (a) and (b) The decrypted images obtained when wrong security keys are used respectively corresponding to those in Figs. 5.11(c) and 5.11(f). MSE values corresponding to (a) and (b) are 1.33×10^{-2}, and 1.22×10^{-2}, respectively. PSNR values corresponding to (a) and (b) are 8.75 dB and 9.13 dB, respectively.

Two irregular analog signals are experimentally tested as a typical example to show the proposed secured free-space optical transmission in dynamic and turbulent media. As shown in Figs. 5.10(a) and 5.10(c), original analog signals, i.e., plaintexts, are fully encrypted into random intensities at the receiving end. The analog signals can be precisely decrypted and obtained as shown in Figs. 5.10(b) and 5.10(d), when correct security keys are applied. MSE and PSNR are calculated to evaluate quality of the encrypted and decrypted signals, as given in Fig. 5.10.

2D grayscale images are also tested, and are experimentally encrypted into random noise as shown in Figs. 5.11(a), 5.11(b), 5.11(d) and 5.11(e). When security keys are correctly applied, the retrieved images are shown in Figs. 5.11(c) and 5.11(f). It is demonstrated that the proposed method is feasible and effective to realize high-fidelity secured free-space optical data transmission through dynamic and turbulent media. Security of the proposed free-space optical transmission through dynamic and turbulent media is further analyzed. When security keys are wrong during the decryption, the plaintexts cannot be retrieved as shown in Figs. 5.12(a) and 5.12(b). Only noise-like images can be obtained. It is experimentally illustrated that the proposed method can realize high-security and high-fidelity free-space optical data transmission in dynamic and turbulent scattering environment. Moreover, since all kinds of data (e.g., colorful images and video streams) can be represented with combinations of analog signals or binary signals, it is feasible that all kinds of data

can be transmitted with the proposed method. The proposed encryption scheme can be combined with other encryption transmission approaches (e.g. compressive sensing chaotic encryption) to improve the capacity or security of the system.

5.6 Summary

In summary, a new approach has been proposed to realize high-fidelity and high-security ghost diffraction and transmission through static scattering media. A flexible combination of computer-generated magnification factors and physically-generated scaling factors are utilized as security keys to achieve high-security free-space optical transmission. Absorptive filters are used to generate nonlinear scaling factors. Feasibility and effectiveness of the proposed method have been demonstrated experimentally. A novel research perspective for secured optical analog-signal transmission through scattering media in free space could be opened up by the proposed physically-secured ghost diffraction.

In addition, a new scheme has been proposed to realize high-fidelity secured free-space optical data transmission through dynamic and turbulent media by encoding information carriers. An encoding algorithm is designed to transform the data into a series of 2D patterns as information carriers. A novel differential method is developed to suppress noise, and a series of random security keys are also generated. The ciphertexts with high randomness are collected at the receiving end, when a different number of absorptive filters are arbitrarily applied in the free-space optical channel. Feasibility and effectiveness of the proposed method are fully verified by optical experiments. The proposed approach provides a promising way to realize high-fidelity secured optical data transmission over dynamic and turbulent media in a free-space optical channel.

Chapter 6 Conclusion and future work

6.1 Conclusion

This thesis devotes to overcoming the challenges in optical wireless transmission in scattering environments.

(1) A free-space optical transmission scheme is developed, where 2D patterns of random numbers are utilized as information carriers. The generated 2D patterns of random numbers are sequentially embedded into the SLM to modulate the light field. A differential method is introduced to suppress noise. The modulated wave transmits through a static scattering media (i.e., two cascaded diffusers), and high-fidelity analog signals can be retrieved at the receiving end.

(2) In dynamic scattering environment, transmission errors are induced in the transmission channel. To correct transmission errors aroused by the dynamic scattering media, a fixed pattern is utilized repeatedly during the transmission process to realize a real-time correction process. The data collected at the receiving end are corrected, and then are applied to retrieve the signal. The errors can be temporally corrected and eliminated, so the proposed method can realize high-fidelity optical transmission through dynamic smoke. It is also demonstrated that when the average optical thickness in the free-space optical data transmission channel is lower than 2.5, irregular analog signals can be retrieved with high fidelity at the receiving end.

(3) An improved transmission scheme is further developed, where the fixed pattern is optimized to realize high-fidelity optical transmission in complex and dynamic scattering environment. The fixed pattern is used with a differential method. The differential method is directly introduced in the pattern generation algorithm, where each pixel of original signals is separated. Experimental studies demonstrate

that analog signals retrieved at the receiving end are always of high fidelity when the *APL* is less than 29.0 dB.

(4) To realize optically secured transmission through scattering media, computer-generated security keys are utilized with physically-generated keys (i.e., scaling factors). The proposed method has high security, since key space of computer-generated keys and physically-generated keys is infinite. In addition, how to guarantee the security of optical wireless transmission through dynamic scattering media is also studied. A novel differential method is applied in the optical encoding process to eliminate noise, and a series of security keys are generated. A number of absorptive filters can be arbitrarily assigned in the transmission channel to generate ciphertexts with high randomness. Therefore, transmission model utilized to realize the encryption is difficult to be attacked.

6.2 Contributions of the thesis

The significant contributions of this thesis are summarized as follows:

(1). An optical transmission scheme is proposed to directly generate a series of 2D arrays of random numbers to encode the signals to realize high-fidelity free-space optical information transmission through scattering media. Optical experimental results demonstrate that high-fidelity free-space optical information transmission through scattering media is realized by using the proposed method.

(2). A new approach is proposed to realize high-fidelity free-space optical data transmission through dynamic smoke using a series of 2D arrays of random numbers via pixel-to-plane encoding. A series of 2D arrays with random numbers are generated to be used as information carriers in the free-space optical data transmission channel. Transmission errors induced by dynamic smoke are temporally corrected using a fixed pattern. It is experimentally demonstrated that irregular analog signals

can be retrieved with high fidelity at the receiving end, when the AOT in the free-space optical data transmission channel is lower than 2.5.

(3). A new scheme has been proposed to realize high-fidelity free-space optical analog-signal transmission in dynamic and complex scattering environments using binary encoding with a modified differential method. An algorithm is developed to generate a series of 2D binary arrays as information carriers to be used in optical transmission channel. The proposed method employs only two 2D binary patterns for the transmission of each pixel of an analog signal in dynamic and complex scattering environments, and only the half number of measurements is used compared to that in conventional methods. Dynamic scaling factors can be effectively corrected as verified in optical experiments to realize high-fidelity analog-signal retrieval at the receiving end. It is experimentally demonstrated that analog signals retrieved at the receiving end are always of high fidelity using the proposed method, when the *APL* is less than 29.0 dB.

(4). A new approach is proposed to realize high-fidelity and high-security optical wireless transmission. A flexible combination of computer-generated magnification factors and physically-generated scaling factors is utilized as security keys to achieve high-security free-space optical transmission in static scattering media. Absorptive filters are used to generate nonlinear scaling factors. Moreover, an optimized method is introduced to realize optically secured transmission through dynamic scattering media. A novel differential method is developed to suppress noise, and a series of random security keys are also generated. The ciphertexts with high randomness are collected at the receiving end, when a different number of absorptive filters are arbitrarily applied in the free-space optical channel. Feasibility and effectiveness of the proposed methods have been demonstrated experimentally. The proposed

approaches provide a promising way to realize high-fidelity secured optical data transmission via optical encoding method.

6.3 Future work

Optical transmission schemes utilizing the concept of single-pixel ghost diffraction and transmission are introduced in this thesis. Different optical encoding algorithms are proposed to generate information carriers to realize optical transmission in different environments. Two scientific problems are addressed in this thesis, i.e., high-quality transmission and high-security transmission. Some improvements can be further made in the future work, which are described as follows:

(1). Besides the utilization of high switching rate devices, binary signals can be compressed with innovative encoding algorithms or other multiplexing methods to improve the capacity of signal transmission. For instance, orbital angular momentum (OAM) multiplexing method can be utilized to encode binary sequences into different combinations of OAM bases, and the corresponding patterns are employed as information carriers to realize binary signal transmission.

(2). In addition to the data transmission process involving ghost diffraction, the time-domain ghost imaging method [36] can also be employed for data transmission. Modulating the light source with an arbitrary waveform generator results in the emission of a 2D modulated light signal with varying intensities over time. The transmitted optical field information is collected with a camera at the receiving end. The 2D sequences obtained can be utilized to retrieve temporal signals over a specific duration. Capacity of the transmission channel can be significantly improved.

Bibliography

[1]. M. A. Khalighi and M. Uysal, “Survey on free space optical communication: a communication theory perspective,” IEEE Commun. Surveys Tuts. **16**(4), 2231–2258 (2014).

[2]. T. B. Pittman, Y. H. Shih, D. V. Strekalov, and A. V. Sergienko, “Optical imaging by means of two-photon quantum entanglement,” Phys. Rev. A **52**(5), R3429–R3432 (1995).

[3]. D. V. Strekalov, A. V. Sergienko, D. N. Klyshko, and Y. H. Shih, “Observation of two-photon "ghost" interference and diffraction,” Phys. Rev. Lett. **74**(18), 3600–3603 (1995).

[4]. A. F. Abouraddy, B. E. Saleh, A. V. Sergienko, and M. C. Teich, “Role of entanglement in two-photon imaging,” Phys. Rev. Lett. **87**(12), 123602 (2001).

[5]. A. F. Abouraddy, P. R. Stone, A. V. Sergienko, B. E. Saleh, and M. C. Teich, “Entangled-photon imaging of a pure phase object,” Phys Rev Lett **93**(21), 213903 (2004).

[6]. R. S. Bennink, S. J. Bentley, and R. W. Boyd, “"Two-Photon" coincidence imaging with a classical source,” Phys. Rev. Lett. **89**(11), 113601 (2002).

[7]. J. Cheng, and S. Han, “Incoherent coincidence imaging and its applicability in X-ray diffraction,” Phys. Rev. Lett. **92**(9), 093903 (2004).

[8]. A. Gatti, E. Brambilla, M. Bache, and L. A. Lugiato, “Ghost imaging with thermal light: comparing entanglement and classical correlation,” Phys. Rev. Lett. **93**(9), 093602 (2004).

[9]. J. H. Shapiro, “Computational ghost imaging,” Phys. Rev. A **78**(6) (2008).

[10]. Y. Bromberg, O. Katz, and Y. Silberberg, “Ghost imaging with a single detector,” Phys. Rev. A **79**(5) (2009).

[11]. Y. Ooka, and S. Fukatsu, "Differential ghost imaging in time domain," Appl. Phys. Lett. **111**(6), 061106 (2017).

[12]. B. Sun, S. S. Welsh, M. P. Edgar, J. H. Shapiro, and M. J. Padgett, "Normalized ghost imaging," Opt. Express **20**(15), 16892–16901 (2012).

[13]. K. H. Luo, B. Q. Huang, W. M. Zheng, and L. A. Wu, "Nonlocal Imaging by Conditional Averaging of Random Reference Measurements," Chinese Phys. Lett. **29**(7) (2012).

[14]. O. Katz, Y. Bromberg, Y. Silberberg, "Compressive ghost imaging," Appl. Phys. Lett. **95**(13), 131110 (2009).

[15]. M. F. Duarte, M. A. Davenport, D. Takhar, J. N. Laska, T. Sun, K. F. Kelly, and R. G. Baraniuk, "Single-pixel imaging via compressive sampling," IEEE Signal Process Mag. **25**(2), 83–91 (2008).

[16]. L. Jiying, Z. Jubo, L. Chuan, and H. Shisheng, "High-quality quantum-imaging algorithm and experiment based on compressive sensing," Opt. Lett. **35**(8), 1206–1208 (2010).

[17]. V. Katkovnik, J. Astola, "Compressive sensing computational ghost imaging," JOSA A, **29**(8), 1556–1567 (2012).

[18]. H. Wu, X. Zhang, J. Gan, C. Luo, "High-quality computational ghost imaging using an optimum distance search method," IEEE Photon. J. **8**(6), 1–9 (2016).

[19]. X. Hu, J. Suo, T. Yue, L. Bian, Q. Dai, "Patch-primitive driven compressive ghost imaging," Opt. Express 23(9), 11092–11104 (2015).

[20]. B. Sun, M. P. Edgar, R. Bowman, L. E. Vittert, S. Welsh, A. Bowman, M. J. Padgett, "3D computational imaging with single-pixel detectors," Science, **340**(6134), 844–847 (2013).

[21]. M. Xi , H. Chen, Y. Yuan, G. Wang, Y. He, Y. Liang, Z. Xu, "Bi-frequency 3D ghost imaging with Haar wavelet transform," Opt. Express 27(22), 32349–32359 (2019).

[22]. M. Bache, D. Magatti, F. Ferri, A. Gatti, E. Brambilla, L. Lugiato, "Coherent imaging of a pure phase object with classical incoherent light," Phys. Rev. A **73**(5), 053802 (2006).

[23]. Y. T. Zhang, C. J. He, H. G. Li, K. G. Wang, "Novel ghost imaging method for a pure phase object," Chinese Phys. Lett. **25**(7), 2481 (2008).

[24]. C. M. Watts, D. Shrekenhamer, J. Montoya, G. Lipworth, J. Hunt, T. Sleasman, W. J. Padilla, "Terahertz compressive imaging with metamaterial spatial light modulators," Nat. Photon. **8**(8), 605–609 (2014).

[25]. R. I. Stantchev, B. Sun, S. M. Hornett, P. A. Hobson, G. M. Gibson, M. J. Padgett, E. Hendry, "Noninvasive, near-field terahertz imaging of hidden objects using a single-pixel detector," Sci. Adv. **2**(6), e1600190 (2016).

[26]. J. Ma, "Single-pixel remote sensing," IEEE Geosci. Remote. Sens. Lett. 6(2), 199–203 (2009).

[27]. A. X. Zhang, Y. H. He, L. A. Wu, L. M. Chen, B. B. Wang, "Tabletop x-ray ghost imaging with ultra-low radiation," Optica, **5**(4), 374–377 (2018).

[28]. Y. Klein, A. Schori, I. P. Dolbnya, K. Sawhney, S. Shwartz, "X-ray computational ghost imaging with single-pixel detector," Opt. express **27**(3), 3284–3293 (2019).

[29]. L. Bian, J. Suo, J. Chung, X. Ou, C. Yang, F. Chen, Q. Dai, "Fourier ptychographic reconstruction using Poisson maximum likelihood and truncated Wirtinger gradient," Sci. Rep. **6**(1), 1–10 (2016).

[30]. K. Guo, S. Jiang, G. Zheng, "Multilayer fluorescence imaging on a single-pixel detector," Biomed. Opt. Express **7**(7), 2425–2431 (2016).

[31]. Y. Bai, S. Han, "Ghost imaging with thermal light by third-order correlation," Phys. Rev. A **76**(4), 043828 (2007).

[32]. X. H. Chen, I. N. Agafonov, K. H. Luo, Q. Liu, R. Xian, M. V. Chekhova, and L. A. Wu, "High-visibility, high-order lensless ghost imaging with thermal light," Opt. Lett. **35**(8), 1166–1168 (2010).

[33]. R. Borghi, F. Gori, M. Santarsiero, "Phase and amplitude retrieval in ghost diffraction from

field-correlation measurements," Phys. Rev. Lett. **96**(18), 183901 (2006).

[34]. G. Ying, Q. Wei, X. Shen, S. Han, "A two-step phase-retrieval method in Fourier-transform ghost imaging," Opt. Commun. **281**(20), 5130–5132 (2008).

[35]. T. Shirai, T. Setälä, and A. T. Friberg, "Temporal ghost imaging with classical non-stationary pulsed light," J. Opt. Soc. Am. B **27**(12), 2549–2555 (2010).

[36]. F. Devaux, P. A. Moreau, S. Denis, E. Lantz, "Computational temporal ghost imaging," Optica, **3**(7), 698–701 (2016).

[37]. T. Setälä, T. Shirai, A. T. Friberg, "Fractional Fourier transform in temporal ghost imaging with classical light," Phys. Rev. A **82**(4), 043813 (2010).

[38]. S. Jiang, Y. Wang, T. Long, X. Meng, X. Yang, R. Shu, B. Sun, "Information security scheme based on computational temporal ghost imaging," Sci. Rep. **7**(1), 1–8 (2017).

[39]. Z. Pan, L. Zhang, "Optical cryptography-based temporal ghost imaging with chaotic laser," IEEE Photon. Technol. Lett. 29(16), 1289–1292 (2017).

[40]. Y. Kang, L. Zhang, H. Ye, M. Zhao, S. Kanwal, C. Bai, D. Zhang, "One-to-many optical information encryption transmission method based on temporal ghost imaging and code division multiple access," Photon. Research **7**(12), 1370–1380 (2019).

[41]. Y. Kang, R. Xiong, L. H. Zhang, X. H. Ma, D.W. Zhang. "Effect of different temporal light fields on compressive temporal ghost imaging reconstruction," Laser Phys. Lett. **16**(11), 115204 (2019).

[42]. Z. Bo, W. Gong, S. Han, "Focal-plane three-dimensional imaging method based on temporal ghost imaging: a proof of concept simulation," J. Opt. Soc. Am. A **37**(3), 417–421 (2020).

[43]. H. Huang, C. Hu, S. Yang, M. Chen, H. Chen, "Temporal Ghost Imaging by Means of Fourier Spectrum Acquisition," IEEE Photon. J. **12**(5), 1–12 (2020).

[44]. Y. Wang, H. Chen, W. Jiang, X. Li, X. Chen, X. Meng, B. Sun, "Optical encryption for

visible light communication based on temporal ghost imaging with a micro-LED," Opt. Lasers Eng. **134**, 106290 (2020).

[45]. P. Ryczkowski, M. Barbier, A. T. Friberg, J. M. Dudley, G. Genty, "Ghost imaging in the time domain," Nat. Photon. **10**(3), 167–170 (2016).

[46]. B. Judkewitz, R. Horstmeyer, I. M. Vellekoop, I. N. Papadopoulos, C. Yang, "Translation correlations in anisotropically scattering media," Nat. Phys. **11**(8), 684–689 (2015).

[47]. 5. G. Satat, M. Tancik, and R. Raskar, "Towards photography through realistic fog," in *2018 IEEE International Conference on Computational Photography* (*ICCP*), (IEEE, 2018), pp. 1–10.

[48]. J. Duan, J. T. Zhan, S. Zhang, C. X. Zhao, J. Peng, Y. Lei, and Q. Fu, "Experiment of polarization transmission characteristics and polarization imaging in simulation smoke/fog environment," in *Annual Conference of the Chinese-Society-for-Optical-Engineering on Applied Optics and Photonics, China* (*AOPC*), (Beijing, PEOPLES R CHINA, 2015) , pp. 96740D.

[49]. K. Su, L. Moeller, R. B. Barat, and J. F. Federici, "Experimental comparison of performance degradation from terahertz and infrared wireless links in fog," J. Opt. Soc. Am. A **29**(2), 179–184 (2012).

[50]. M. Ijaz, Z. Ghassemlooy, H. Le-minh, S. Zvanovec, J. Perez, J. Pesek, and O. Fiser, "Experimental validation of fog models for FSO under laboratory controlled conditions," in *2013 IEEE 24th Annual International Symposium on Personal, Indoor, and Mobile Radio Communications (PIMRC)*, (IEEE2013), pp. 19–23.

[51]. Z. X. He, P. Zhang, D. Wu, X. J. Wu, S. He, J. Wei, X. Y. Gong, T. Wang, D. S. Wang, K. X. Han, S. F. Tong, and H. L. Jiang, "1.7 μ m band modulated optical signal transmission through water fog using pump modulated Tm-doped fiber laser," in *Asia Communications*

and Photonics Conference (*ACP*), (Chengdu, PEOPLES R CHINA, 2019), pp. M4A–46.

[52]. S. Q. Hu, H. J. Liu, L. F. Zhao, and X. L. Bian, "The Link Attenuation Model Based on Monte Carlo Simulation for Laser Transmission in Fog Channel," IEEE Photon. J. **12**(4), 1–10 (2020).

[53]. Y. Guo, M. Kong, M. Sait, S. Marie, O. Alkhazragi, T. K. Ng, and B. S. Ooi, "Compact scintillating-fiber/450-nm-laser transceiver for full-duplex underwater wireless optical communication system under turbulence," Opt. Express **30**(1), 53–69 (2022).

[54]. C. Shen, Y. Guo, H. M. Oubei, T. K. Ng, G. Liu, K. H. Park, K. T. Ho, M. S. Alouini, and B. S. Ooi, "20-meter underwater wireless optical communication link with 1.5 Gbps data rate," Opt. Express **24**(22), 25502–25509 (2016).

[55]. Z. Ghassemlooy, H. Le Minh, S. Rajbhandari, J. Perez, and M. Ijaz, "Performance analysis of ethernet/fast-ethernet free space optical communications in a controlled weak turbulence condition," J. Lightwave Technol. **30**(13), 2188–2194 (2012).

[56]. J. Perez, Z. Ghassemlooy, S. Rajbhandari, M. Ijaz, and H. L. Minh, "Ethernet FSO communications link performance study under a controlled fog environment," IEEE Commun. Lett. **16**(3), 408–410 (2012).

[57]. M. Ijaz, Z. Ghassemlooy, J. Pesek, O. Fiser, H. L. Minh, and E. Bentley, "Modeling of fog and smoke attenuation in free space optical communications link under controlled laboratory conditions," J. Lightwave Technol. **31**(11), 1720–1726 (2013).

[58]. B. R. Babaria, T. L. Alvarez, M. T. Bergen, and R. J. Servatius, "Transmission of light in a synthetic fog medium," in *IEEE 30th Annual Northeast Bioengineering Conference*, (Western New England Coll, Springfield, MA, 2004), pp. 23–24.

[59]. P. Lin, T. Wang, W. Ma, Q. Yang, and Z. Liu, "Transmission characteristics of 1.55 and 2.04 μm laser carriers in a simulated smoke channel based on an actively mode-locked

fiber laser," Opt. Express 28(26), 39216–39226 (2020).

[60]. C. Zhang, J. Zhang, X. Wu, and M. Huang, "Numerical analysis of light reflection and transmission in poly-disperse sea fog," Opt. Express **28**(17), 25410–25430 (2020).

[61]. M. Ijaz, Z. Ghassemlooy, H. L. Minh, S. Rajbhandari, and J. Perez, "Analysis of fog and smoke attenuation in a free space optical communication link under controlled laboratory conditions," in *2012 International Workshop on Optical Wireless Communications,* (IEEE, 2012), pp. 1–3.

[62]. P. Duthon, M. Colomb, and F. Bernardin, "Light Transmission in Fog: The Influence of Wavelength on the Extinction Coefficient," Appl. Sci. **9**(14), 2843 (2019).

[63]. X. X. Chen, and Z. S. Wu, "Transmission Characteristics of Polarized Light in Low Visibility Fog," in *12th International Symposium on Antennas, Propagation and Electromagnetic Theory (ISAPE),* (Hangzhou, PEOPLES R CHINA, 2018), pp. 1–5.

[64]. L. Ma, C. Wang, and L. Liu, "Polarized radiative transfer in dense dispersed media containing optically soft sticky particles," Opt. Express **28**(19), 28252–28268 (2020).

[65]. X. Zeng, X. Chen, Y. Li, and Q. Xiangnan, "Polarization enhancement of linearly polarized light through foggy environments at UV–NIR wavelengths," Appl. Opt. **60**(26), 8103–8108 (2021).

[66]. S. Zhang, J. T. Zhan, Q. Fu, J. Duan, Y. C. Li, and H. L. Jiang, "Propagation of linear and circular polarization in a settling smoke environment: theory and experiment," Appl. Opt. **58**(17), 4687–4694 (2019).

[67]. X. W. Zeng, J. K. Chu, W. D. Cao, W. D. Kang, and R. Zhang, "Visible-IR transmission enhancement through fog using circularly polarized light," Appl. Opt. **57**(23), 6817–6822 (2018).

[68]. S. Zhang, J. Zhan, Q. Fu, J. Duan, Y. Li, and H. Jiang, "Effects of environment variation of glycerol smoke particles on the persistence of linear and circular polarization," Opt.

Express **28**(14), 20236–20248 (2020).

[69]. B. Z. Bentz, B. J. Redman, J. D. van der Laan, K. Westlake, A. Glen, A. L. Sanchez, and J. B Wright, "Light transport with weak angular dependence in fog," Opt. Express **29**(9), 13231–13245 (2021).

[70]. B. Wu, B. Marchant, and M. Kavehrad, "Channel modeling of light signals propagating through a battlefield environment: analysis of channel spatial, angular, and temporal dispersion," Appl. Opt. **46**(25), 6442–6448 (2007).

[71]. R. Q. Fugate, D. L. Fried, G. A. Ameer, B. Boeke, S. Browne, P. H. Roberts, R. Ruane, G. A. Tyler, and L. Wopat, "Measurement of atmospheric wavefront distortion using scattered light from a laser guide-star," Nature **353**(6340), 144–146 (1991).

[72]. I. M. Vellekoop, and A. Mosk, "Focusing coherent light through opaque strongly scattering media," Opt. Lett. **32**(16), 2309–2311 (2007).

[73]. H. B. de Aguiar, S. Gigan, and S. Brasselet, "Enhanced nonlinear imaging through scattering media using transmission-matrix-based wave-front shaping," Phys. Rev. A **94**(4), 043830 (2016).

[74]. S. M. Popoff, G. Lerosey, R. Carminati, M. Fink, A. C. Boccara, and S. Gigan, "Measuring the transmission matrix in optics: an approach to the study and control of light propagation in disordered media," Phys. Rev. Lett. **104**(10), 100601 (2010).

[75]. Q. Feng, B. Zhang, Z. Liu, C. Lin, and Y. Ding, "Research on intelligent algorithms for amplitude optimization of wavefront shaping," Appl. Opt. **56**(12), 3240–3244 (2017).

[76]. Z. Fayyaz, N. Mohammadian, F. Salimi, A. Fatima, M. R. R. Tabar, and M. R. Avanaki, "Simulated annealing optimization in wavefront shaping controlled

transmission," Appl. Opt. **57**(21), 6233–6242 (2018).

[77]. H. Li, C. M. Woo, T. Zhong, Z. Yu, Y. Luo, Y. Zheng, X. Yang, H. Hui, and P. Lai, "Adaptive optical focusing through perturbed scattering media with a dynamic mutation algorithm," Photonics Res. **9**(2), 202–212 (2021).

[78]. H. Ruan, J. Xu, and C. Yang, "Optical information transmission through complex scattering media with optical-channel-based intensity streaming," Nat. Commun. **12**(1), 1–10 (2021).

[79]. X. Wang, L. V. Wang, C.-W. Sun, and C.-C. Yang, "Polarized light propagation through scattering media: time-resolved Monte Carlo simulations and experiments," J. Biomed. Opt. **8**(4), 608–617 (2003).

[80]. X. Li, Y. Han, H. Wang, T. Liu, S.C. Chen, and H. Hu, "Polarimetric imaging through scattering media: A review," Front. Phys. **10**, 815296 (2022).

[81]. J. B. Snow, J. P. Flatley, D. E. Freeman, M. A. Landry, C. E. Lindstrom, J. R. Longacre, and J. A. Schwartz, "Underwater propagation of high-data-rate laser communications pulses," in *Ocean Optics XI*, (SPIE1992), pp. 419–427.

[82]. Y. Li, Y. Xue, and L. Tian, "Deep speckle correlation: a deep learning approach toward scalable imaging through scattering media," Optica **5**(10), 1181–1190 (2018).

[83]. F. Li, M. Zhao, Z. Tian, F. Willomitzer, and O. Cossairt, "Compressive ghost imaging through scattering media with deep learning," Opt. Express **28**(12), 17395–17408 (2020).

[84]. R. Horisaki, R. Takagi, and J. Tanida, "Learning-based imaging through scattering media," Opt. Express **24**(13), 13738–13743 (2016).

[85]. Y. Luo, S. Yan, H. Li, P. Lai, and Y. Zheng, "Towards smart optical focusing: deep learning-empowered dynamic wavefront shaping through nonstationary

scattering media," Photonics Res. **9**(8), B262–B278 (2021).

[86]. G. Satat, M. Tancik, O. Gupta, B. Heshmat, and R. Raskar, "Object classification through scattering media with deep learning on time resolved measurement," Opt. Express **25**(15), 17466–17479 (2017).

[87]. S. Noda, M. Fujita, and T. Asano, "Spontaneous-emission control by photonic crystals and nanocavities," Nat. Photonics **1**(8), 449–458 (2007).

[88]. W. Zhu, I. D. Rukhlenko, and M. Premaratne, "Graphene metamaterial for optical reflection modulation," Appl. Phys. Lett. **102**(24), 241914 (2013).

[89]. W. Yang, and Y.S. Lin, "Tunable metamaterial filter for optical communication in the terahertz frequency range," Opt. Express **28**(12), 17620–17629 (2020).

[90]. Z. Zhang, J. Yang, X. He, Y. Han, J. Zhang, J. Huang, D. Chen, and S. Xu, "All-optical multi-channel switching at telecommunication wavelengths based on tunable plasmon-induced transparency," Opt. Commun. **425,** 196–203 (2018).

[91]. N. B. Hassan, Z. Ghassemlooy, S. Zvanovec, M. Biagi, A. M. Vegni, M. Zhang, and P. Luo, "Non-line-of-sight mimo space-time division multiplexing visible light optical camera communications," J. Light. Technol. **37**(10), 2409–2417 (2019).

[92]. S. Arnon, and D. Kedar, "Non-line-of-sight underwater optical wireless communication network," J. Opt. Soc. Am. A **26**(3), 530–539 (2009).

[93]. Z. Cao, X. Zhang, G. Osnabrugge, J. Li, I. M. Vellekoop, and A. M. Koonen, "Reconfigurable beam system for non-line-of-sight free-space optical communication," Light Sci. Appl. **8**(1), 1–9 (2019).

[94]. W. C. Wang, C. W. Chow, L. Y. Wei, Y. Liu, and C. H. Yeh, "Long distance non-line-of-sight (NLOS) visible light signal detection based on rolling-shutter-patterning of mobile-phone camera," Opt. Express **25**(9), 10103–10108 (2017).

[95]. G. Chen, Z. Xu, and B. M. Sadler, "Experimental demonstration of ultraviolet pulse broadening in short-range non-line-of-sight communication channels," Opt. Express **18**(10), 10500–10509 (2010).

[96]. R. Cao, F. de Goumoens, B. Blochet, J. Xu, and C. Yang, "High-resolution non-line-of-sight imaging employing active focusing," Nat. Photonics **16**(6), 462–468 (2022).

[97]. J. Boger-Lombard, and O. Katz, "Passive optical time-of-flight for non line-of-sight localization," Nat. Commun. **10**(1), 3343 (2019).

[98]. A. Moschevikin, A. Galov, S. Reginya, A. Volkov, and A. Sikora, "The impact of nlos components in time-of-flight networks for indoor positioning systems," in *2013 IEEE 7th International Conference on Intelligent Data Acquisition and Advanced Computing Systems (IDAACS)*, (IEEE2013), pp. 455–460.

[99]. M. O'Toole, D. B. Lindell, and G. Wetzstein, "Confocal non-line-of-sight imaging based on the light-cone transform," Nature **555**(7696), 338–341 (2018).

[100]. F. Heide, M. O'Toole, K. Zang, D. B. Lindell, S. Diamond, and G. Wetzstein, "Non-line-of-sight imaging with partial occluders and surface normals," ACM Transactions on Graphics (ToG) **38**(3), 1–10 (2019).

[101]. M. Laurenzis, F. Christnacher, J. Klein, M. B. Hullin, and A. Velten, "Study of single photon counting for non-line-of-sight vision," in *Advanced Photon Counting Techniques IX*, (SPIE2015), pp. 31–38.

[102]. C. Gong, and Z. Xu, "Non-line of sight optical wireless relaying with the photon counting receiver: A count-and-forward protocol," IEEE Transactions on Wireless Communications **14**(1), 376–388 (2014).

[103]. M. Laurenzis, J. Klein, E. Bacher, and N. Metzger, "Multiple-return single-

photon counting of light in flight and sensing of non-line-of-sight objects at shortwave infrared wavelengths," Opt. Lett. **40**(20), 4815–4818 (2015).

[104]. C. Callenberg, Z. Shi, F. Heide, and M. B. Hullin, "Low-Cost SPAD Sensing for Non-Line-Of-Sight Tracking, Material Classification and Depth Imaging," Acm Transactions on Graphics **40**(4) (2021).

[105]. T. Kim Geok, K. Zar Aung, M. Sandar Aung, M. Thu Soe, A. Abdaziz, C. Pao Liew, F. Hossain, C. P. Tso, and W. H. Yong, "Review of indoor positioning: Radio wave technology," Appl. Sci. **11**(1), 279 (2020).

[106]. I. An, D. Lee, J.w. Choi, D. Manocha, and S.-e. Yoon, "Diffraction-aware sound localization for a non-line-of-sight source," in *2019 International Conference on Robotics and Automation (ICRA)*, (IEEE2019), pp. 4061–4067.

[107]. P. Réfrégier and B. Javidi, "Optical image encryption based on input plane and Fourier plane random encoding," Opt. Lett. **20**(7), 767–769 (1995).

[108]. W. Chen, X. D. Chen, and C. J. R. Sheppard, "Optical image encryption based on diffractive imaging," Opt. Lett. **35**(22), 3817–3819 (2010).

[109]. N. Yang, L. Wang, G. Geraci, M. Elkashlan, J. Yuan, and M. D. Renzo, "Safeguarding 5G wireless communication networks using physical layer security," IEEE Commun. Mag. **53**(4), 20–27 (2015).

[110]. L. Sun and Q. Du, "A Review of Physical Layer Security Techniques for Internet of Things: Challenges and Solutions," Entropy **20**(10), 730–745 (2018).

[111]. N. Jiang, A. Zhao, C. Xue, J. Tang, and K. Qiu, "Physical secure optical communication based on private chaotic spectral phase encryption/decryption," Opt. Lett. **44**(7), 1536–1539 (2019).

[112]. J. Zhao, B. Liu, Y. Mao, J. Ren, X. Xu, X. Wu, L. Jiang, S. Han, and J. Zhang, "High-security physical layer in CAP-PON system based on floating probability disturbance,"

IEEE Photon. Technol. Lett. **32**(7), 367–370 (2020).

[113]. F. I. K. Mousa, N. Al Maadeed, K. Busawon, A. Bouridane, and R. Binns, "Secure MIMO visible light communication system based on user's location and encryption," Journal of Lightwave Technology **35**(24), 5324–5334 (2017).

[114]. G. Blinowski, "Security of visible light communication systems—A survey," Phys. Commun. **34**, 246–260 (2019).

[115]. W. Li, H. Hu, and N. K. Dutta, "High speed all-optical encryption and decryption using quantum dot semiconductor optical amplifiers," Journal of Modern Optics **60**(20), 1741–1749 (2013).

[116]. J. Benaloh, M. Chase, E. Horvitz, and K. Lauter, "Patient controlled encryption: ensuring privacy of electronic medical records," in *Proceedings of the 2009 ACM workshop on Cloud computing security*, (2009), pp. 103–114.

[117]. Y. Fu, M. Cheng, X. Jiang, Q. Yu, L. Huang, L. Deng, and D. Liu, "High-speed optical secure communication with an external noise source and an internal time-delayed feedback loop," Photonics Res. **7**(11), 1306–1313 (2019).

[118]. Z. Shen, Y. Wang, and J. Wu, "Physical Layer Security Performance of Multi-User Mixed Radio-Frequency/Free-Space-Optics System Based on Optimal User Interference," Sensors **23**(14), 6523 (2023).

[119]. G. S. Kanter, D. Reilly, and N. Smith, "Practical physical-layer encryption: The marriage of optical noise with traditional cryptography," IEEE Commun. Mag. **47**(11), 74–81 (2009).

[120]. A. Trichili, M. A. Cox, B. S. Ooi, and M. S. Alouini, "Roadmap to free space optics," J. Opt. Soc. Am. B **37**(11), A184–A201 (2020).

[121]. D. Akbulut, T. J. Huisman, E. G. van Putten, W. L. Vos, and A. P. Mosk, "Focusing light through random photonic media by binary amplitude modulation," Opt. Express **19**(5),

4017–4029 (2011).

[122]. L. Yang, X. Gao, and M.-S. Alouini, "Performance analysis of free-space optical communication systems with multiuser diversity over atmospheric turbulence channels," IEEE Photon. J. **6**(2), 1–17 (2014).

[123]. R. Tobin, A. Halimi, A. McCarthy, M. Laurenzis, F. Christnacher, and G. S. Buller, "Three-dimensional single-photon imaging through obscurants," Opt. Express **27**(4), 4590–4611 (2019).

[124]. X. Hu, H. Zhang, Q. Zhao, P. Yu, Y. Li, and L. Gong, "Single-pixel phase imaging by Fourier spectrum sampling," Appl. Phys. Lett. **114**(5), 051102 (2019).

[125]. M. A. Midoun, X. Y. Wang, and M. Z. Talhaoui, "A sensitive dynamic mutual encryption system based on a new 1D chaotic map," Opt. Lasers Eng. **139**, 106485 (2021).

[126]. Y. G. Su, W. J. Xu, T. L. Li, J. Zhao, and S. Q. Liu, "Optical color image encryption based on fingerprint key and phase-shifting digital holography," Opt. Lasers Eng. **140**, 106550 (2021).

[127]. H. Chen, Z. J. Liu, C. Tanougast, F. F. Liu, and W. Blondel, "Optical cryptosystem scheme for hyperspectral image based on random spiral transform in gyrator domains," Opt. Lasers Eng. **137**, 106375 (2021).

[128]. D. Pelliccia, A. Rack, M. Scheel, V. Cantelli, and D. M. Paganin, "Experimental x-ray ghost imaging," Phys. Rev. Lett. **117**(11), 113902 (2016).

[129]. W. Jiang, X. Li, X. Peng, and B. Sun, "Imaging high-speed moving targets with a single-pixel detector," Opt. Express **28**(6), 7889–7897 (2020).

[130]. Y. Cai and S. Y. Zhu, "Ghost interference with partially coherent radiation," Opt. Lett. **29**(23), 2716–2718 (2004).

[131]. M. Le, G. Wang, H. Zheng, J. Liu, Y. Zhou, and Z. Xu, "Underwater computational ghost imaging," Opt. Express **25**(19), 22859–22868 (2017).

[132]. E. Tajahuerce, V. Durán, P. Clemente, E. Irles, F. Soldevila, P. Andrés, and J. Lancis, "Image transmission through dynamic scattering media by single-pixel photodetection," Opt. Express **22**(14), 16945–16955 (2014).

[133]. M. Dehshiri, S. G Sabouri, and A. Khorsandi, "Structural similarity assessment of an optical coherence tomographic image enhanced using the wavelet transform technique," J. Opt. Soc. Am. A **38**(1), 1–9 (2021).

[134]. Y. N. Zhao, H. Y. Hou, J. C. Han, H. C. Liu, S. H. Zhang, D. Z. Cao, and B. L. Liang, "Full-color photon-counting single-pixel imaging," Opt. Lett. **46**(19), 4900–4903 (2021).

[135]. S. Ahmadzadeh, G. Parr, and W. Q. Zhao, "A Review on Communication Aspects of Demand Response Management for Future 5G IoT- Based Smart Grids," IEEE Access **9**, 77555–77571 (2021).

[136]. S. S. Oyewobi, K. Djouani, and A. M. Kurien, "A review of industrial wireless communications, challenges, and solutions: a cognitive radio approach," Trans. Emerg. Telecommun. Technol. **31**(9), e4055 (2020).

[137]. V. W. Chan, "Free-space optical communications," J. Lightwave Technol. **24**(12), 4750–4762 (2006).

[138]. L. Gong, Q. Zhao, H. Zhang, X.-Y. Hu, K. Huang, J.-M. Yang, and Y.-M. Li, "Optical orbital-angular-momentum-multiplexed data transmission under high scattering," Light Sci. Appl. **8**(1), 1–11 (2019).

[139]. S. Zheng, H. Wang, S. Dong, F. Wang, and G. Situ, "Incoherent imaging through highly nonstatic and optically thick turbid media based on neural network," Photonics Res. **9**(5), B220–B228 (2021).

[140]. P. Qiu, G. Cui, Z. Qian, S. Zhu, X. Shan, Z. Zhao, X. Zhou, X. Cui, and P. Tian, "4.0 Gbps visible light communication in a foggy environment based on a blue laser diode," Opt. Express **29**(9), 14163–14173 (2021).

[141]. M. S. Awan, P. Brandl, E. Leitgeb, F. Nadeem, L. Csugai-Horvath, and R. Nebuloni, "Transmission of High Data Rate Optical Signals in Fog and Snow Conditions," in *1st International Conference on Wireless Communication, Vehicular Technology, Information Theory and Aerospace and Electronic Systems Technology*, (Aalborg, DENMARK, 2009), pp. 702–706.

[142]. J. Perez, S. Zvanovec, Z. Ghassemlooy, and W. O. Popoola, "Experimental characterization and mitigation of turbulence induced signal fades within an ad hoc FSO network," Opt. Express **22**(3), 3208–3218 (2014).

[143]. J. Libich, J. Perez, S. Zvanovec, Z. Ghassemlooy, R. Nebuloni, and C. Capsoni, "Combined effect of turbulence and aerosol on free-space optical links," Appl. Opt. **56**(2), 336–341 (2017).

[144]. A. Almogahed, A. Amphawan, F. Mohammed, A. Alawadhi, and C. Yuen, "Performance improvement of mode division multiplexing free space optical communication system through various atmospheric conditions with a decision feedback equalizer," Cogent Eng. **9**(1), 2034268 (2022).

[145]. A. Almogahed, A. Amphawan, and Y. Fazea, "Mitigation of atmospheric turbulences using mode division multiplexing based on decision feedback equalizer for free space optics," J. Opt. Commun. **41**(2), 185–193 (2020).

[146]. D. Shah, and D. Kothari, "Mitigation of fog and rain effects in free-space optical transmission using combined diversity," in *2nd International Conference on Computer and Communication Technologies*, (CMR Tech Campus, Hyderabad, INDIA, 2015), pp. 725–733.

[147]. E. Kristensson, J. Bood, M. Aldén, E. Nordström, J. Zhu, S. Huldt, P. E. Bengtsson, H. Nilsson, E. Berrocal, and A. Ehn, "Stray light suppression in spectroscopy using periodic shadowing," Opt. Express **22**(7), 7711–7721 (2014).

[148]. E. Kristensson, A. Ehn, and E. Berrocal, "High dynamic spectroscopy using a digital micromirror device and periodic shadowing," Opt. Express **25**(1), 212–222 (2017).

[149]. H. K. Hughes, "Beer's law and the optimum transmittance in absorption measurements," Appl. Opt. **2**(9), 937–945 (1963).

[150]. S. Ahmadzadeh, G. Parr, and W. Q. Zhao, "A review on communication aspects of demand response management for future 5G IoT-based smart grids," IEEE Access **9**, 77555–77571 (2021).

[151]. J. Wang, J. Y. Yang, I. M. Fazal, N. Ahmed, Y. Yan, H. Huang, Y. Ren, Y. Yue, S. Dolinar, and M. Tur, "Terabit free-space data transmission employing orbital angular momentum multiplexing," Nat. Photonics **6**(7), 488–496 (2012).

[152]. M. Figueiredo, L. N. Alves, and C. Ribeiro, "Lighting the wireless world: The promise and challenges of visible light communication," IEEE Consum. Electron. Mag. **6**(4), 28–37 (2017).

[153]. Y. Cao, Y. Xiao, Z. Pan, L. Zhou, and W. Chen, "High-fidelity temporally-corrected transmission through dynamic smoke via pixel-to-plane data encoding," Opt. Express **30**(20), 36464–36477 (2022).

[154]. Z. Pan, Y. Xiao, L. Zhou, Y. Cao, M. Yang, and W. Chen, "Non-line-of-sight optical information transmission through turbid water," Opt. Express **29**(24), 39498–39510 (2021).

[155]. A. Assefa, P. J. Chen, X. L. Ho, and J. D. White, "On the potential of solid state LED strips utilizing an organic color converter for non-line of sight visible light communication," Opt. Express **25**(20), 24242–24250 (2017).

[156]. X. Sun, W. Cai, O. Alkhazragi, E. N. Ooi, H. He, A. Chaaban, C. Shen, H. M. Oubei, M. Z. M. Khan, and T. K. Ng, "375-nm ultraviolet-laser based non-line-of-sight underwater optical communication," Opt. Express **26**(10), 12870–12877 (2018).

[157]. Y. Xiao, L. Zhou, and W. Chen, "Wavefront control through multi-layer scattering media

using single-pixel detector for high-PSNR optical transmission," Opt. Lasers Eng. **139**, 106453 (2021).

[158]. Y. Cao, Y. Xiao, Z. Pan, L. Zhou, and W. Chen, "Direct generation of 2D arrays of random numbers for high-fidelity optical ghost diffraction and information transmission through scattering media," Opt. Lasers Eng. **158**, 107141 (2022).

[159]. Z. Pan, Y. Xiao, Y. Cao, L. Zhou, and W. Chen, "Optical analog-signal transmission and retrieval through turbid water," Appl. Opt. **60**(34), 10704–10713 (2021).

[160]. V. Ostromoukhov, "A simple and efficient error-diffusion algorithm," In Proceedings of the 28th annual conference on Computer graphics and interactive techniques, pp. 567–572 (2001).

[161]. Z. Wang, G. R. Arce, and G. Di Crescenzo, "Halftone visual cryptography via error diffusion," IEEE Trans. Inf. Forensics Secur. 4(3), 383–396 (2009).

[162]. R. W. Floyd, "An adaptive algorithm for spatial gray-scale," Proc. Soc. Inf. Disp. Vol. 17, 75–77 (1976).

[163]. W. Chen, "Correlated-photon secured imaging by iterative phase retrieval using axially-varying distances," IEEE Photon. Technol. Lett. **28**(18), 1932-1935 (2016).

[164]. Y. Xiao, L. Zhou, and W. Chen, "High-fidelity ghost diffraction and transmission in free space through scattering media," Appl. Phys. Lett. **118**(10), 104001 (2021).

[165]. A. Carnicer, M. Montes-Usategui, S. Arcos, and I. Juvells, "Vulnerability to chosen-cyphertext attacks of optical encryption schemes based on double random phase keys," Opt. Lett. **30**(13), 1644–1646 (2005).

[166]. Y. Xiao, L. Zhou, Z. Pan, Y. Cao, and W. Chen, "Physically-enhanced ghost encoding," Opt. Lett. **47**(2), 433-436 (2022).

[167]. Y. Xiao, L. Zhou, Z. Pan, Y. Cao, and W. Chen, "Physically-secured high-fidelity

free-space optical data transmission through scattering media using dynamic scaling factors," Opt. Express **30**(5), 8186-8198 (2022).

[168]. E. Diamanti, H. W. Lo, B. Qi, and Z. L. Yuan, "Practical challenges in quantum key distribution," npj Quantum Inf. **2**(1), 1–12 (2016).

[169]. F. Xu, M. Curty, B. Qi, and H. K. Lo, "Measurement-device-independent quantum cryptography," IEEE J. Sel. Top. Quantum Electron. **21**(3), 148–158 (2015).

[170]. N. Li, H. Susanto, B. Cemlyn, I. D. Henning, and M. J. Adams, "Secure communication systems based on chaos in optically pumped spin-VCSELs," Opt. Lett. **42**(17), 3494–3497 (2017).

[171]. A. Bogris, A. Argyris, and D. Syvridis, "Encryption efficiency analysis of chaotic communication systems based on photonic integrated chaotic circuits," IEEE J. Quantum Electron. **46**(10), 1421–1429 (2010).

[172]. N. Jiang, A. K. Zhao, S. Q. Liu, C. P. Xue, and K. Qiu, "Chaos synchronization and communication in closed-loop semiconductor lasers subject to common chaotic phase-modulated feedback," Opt. Express **26**(25), 32404–32416 (2018).

[173]. Y. Xiao, L. Zhou, and W. Chen, "Direct single-step measurement of Hadamard spectrum using single-pixel optical detection," IEEE Photon. Technol. Lett. **31**(11), 845–848 (2019).

[174]. W. Chen, "Spatial nonlinear optics for securing information," Light Sci. Appl. **11**(1), 1–2 (2022).

[175]. P. Clemente, V. Durán, V. Torres-Company, E. Tajahuerce, and J. Lancis, "Optical encryption based on computational ghost imaging," Opt. Lett. **35**(14), 2391–2393 (2010).

[176]. M. Tanha, R. Kheradmand, and S. Ahmadi-Kandjani, "Gray-scale and color optical encryption based on computational ghost imaging," Appl. Phys. Lett. **101**(10), 101108 (2012).

[177]. P. Zheng, Q. Dai, Z. Li, Z. Ye, J. Xiong, H. C. Liu, G. Zheng, and S. Zhang, "Metasurface-

based key for computational imaging encryption," Sci. Adv. **7**(21), eabg0363 (2021).

[178]. W. Chen, B. Javidi, and X. Chen, "Advances in optical security systems," Adv. Opt. Photon. **6**(2), 120–155 (2014).